Trapping Efficiency of Non-Buoyant Microplastics by River Groynes

Kelly Lau

Thesis submitted to the University of Ottawa
in partial Fulfillment of the requirements for the
Master of Applied Science in Environmental Engineering

Ottawa-Carleton Institute for Environmental Engineering
Faculty of Engineering
University of Ottawa

Abstract

Microplastics (MPs) have become an urgent environmental issue, driven by rapid industrial plastic use and inadequate waste management. As rivers act both as major transport pathways and temporary sinks, reducing MPs loads within them can effectively limit their transfer into the food chain. This study investigates the effectiveness of groynes, structures originally designed for flow and erosion control, in trapping non-buoyant MPs. Ten configurations formed from pairwise combinations of four common groyne geometries were tested using MPs (of equivalent diameter d_{eq} = 2.29 mm) of two densities (ρ_s = 1.08 and 1.11 g/cm³). Experiments were conducted in a recirculating flume using subcritical turbulent flow. A particle tracking model was employed to track and record particle trajectories around groyne fields, from which trapping efficiencies and retention zones were derived. It was observed that MPs entered the groyne field from the downstream end, forming a clockwise gyre. All scenarios retained > 6% of particles during the test period. When both groynes used in the experiments shared the same shape, upstream-facing inclined groynes exhibited the greatest trapping potential, achieving a peak retention rate of 20.7 ± 3.7% over extended durations. Despite their lower entrainment, straight and T-shaped groynes retained particles more effectively, with < 3% trapped particles leaving the field during the tested period. In cases where the upstream groyne was straight and the downstream geometry was varied, particle escape was negligible, with downstream repelling groynes consistently trapping more MPs than other configurations. Although particle density had little effect on particle entrainment, lighter particles showed lower escape and smaller retention zone, indicating MPs sensitivity to vertical flow dynamics within the groyne field.

Acknowledgements

I would first like to express my sincere gratitude to all supervisors for their guidance and patience throughout this thesis. Despite demanding schedules, they accommodated my tight timeline, attended weekly meetings, and provided timely and constructive feedback on draft manuscripts, which greatly supported the progress of this work.

Special thanks go to Prof. Abdolmajid Mohammadian for the trust placed in me from the beginning of the project. Detailed explanations of engineering concepts, coupled with the constant effort to teach beyond what was required, made a lasting impact. The steady support, always just a phone call away, was invaluable during the course of this thesis.

I am also grateful to Prof. Abolghasem Pilechi for sharing expertise in microplastics and offering practical advice on experimental design. The many relevant papers provided were consistently useful, offering fresh perspectives and helpful direction at important stages of the research.

My appreciation extends to Prof. Ioan Nistor for making time despite a very busy schedule, particularly during a demanding period of the year. The insights shared on the research topic and central questions helped refine the study and strengthen its overall focus.

Lastly, I would like to thank my parents, roommates and friends for the encouragement and mental support they provided. Their belief and reassurance gave me the motivation to persevere and complete this work.

Table of Contents

List of Figures

List of Tables

List of Symbols

Symbol	Meaning	SI Unit
A_{mc}	Maximum cross-sectional area	mm^2 or μm^2
A_p	Project area	mm^2 or μm^2
A_s	Surface area of particle	mm^2 or μm^2
A_{sph}	Surface area of the volume equivalent sphere	mm^2 or μm^2
a	Length of longest side	mm or μm
ASF	Aschenbrenner shape factor	–
b	Length of intermediate side	mm or μm
C_d	Drag coefficient	–
CSF	Corey Shape Factor	–
c	Length of shortest side	mm or μm
d_n	Nominal diameter	mm or μm
D_x	Longitudinal dispersion coefficients	m^2/s
d_*	Dimensionless diameter	–
d_{50}	Median size of sediment grains	mm or μm
d	Particle diameter	mm or μm
d_{eq}	Projected area equivalent diameter	mm or μm
E	Elongation	–
F_B	Buoyancy force	N
F_D	Drag force	N
F_G	Gravitational force	N
F_L	Lift force	N
f	Flatness	–
g'	Reduced gravity acceleration	m/s^2
k_s	Bed roughness	m
k_t	Turbulent kinetic energy	m^2/s^2
L_p	Projected length	mm or μm
l_t	Integral length scale	m
P	Rouse number	–
Re_p	Particle Reynolds number	–

Symbol	Meaning	SI Unit
u_*	Shear velocity	m/s
u_{*c}	Critical shear velocity	m/s
V	Volume of particle	mm^3 or μm^3
v_x	Streamwise velocity	m/s
w_s	Settling velocity	cm/s or mm/s
w_*	Dimensionless settling velocity	–
ε	Turbulent kinetic energy dissipation rate	m^2/s^3
γ	Diffusion exponent	–
λ_L	Filter coefficient for particles of size L	cm^{-1}
Φ	Sphericity	–
ρ	Density of fluid	g/cm^3
ρ_s	Density of MPs particles	g/cm^3
τ_c	Critical shear stress	N/m^2

List of Abbreviations

Abbreviation	Meaning
LDPE	Low-density polyethylene
PA/PA6	Polyamide, nylon
PE	Polyethylene
PES	Polyester
PET	Polyethylene terephthalate
PLA	Polylactic acid
PMMA	Polymethyl methacrylate/ acrylic
POM	Polyoxymethylene
PP	Polypropylene
PS	Polystyrene
PVC	Polyvinyl chloride

Chapter 1 Introduction

1.1 Background

The exponential growth in plastic production, coupled with improper disposal practices, has led to the widespread introduction of microplastics (MPs, < 5 mm in diameter) into ecosystems through both direct release and the degradation of larger plastic products [1]. MPs have emerged as a pervasive environmental concern due to their troubling properties, including resistance to degradation, small and ingestible size, and their capacity to act as vectors for pathogens [2].

Aquatic MPs have long been the focus of research, given their widespread occurrence and mobility in water systems. As seen in Figure 1, hydrological forces play a central role in shaping MPs transportation pathways (circled in light blue in Fig. 1), facilitating the transfer of MPs across aquatic environments [3], [4].

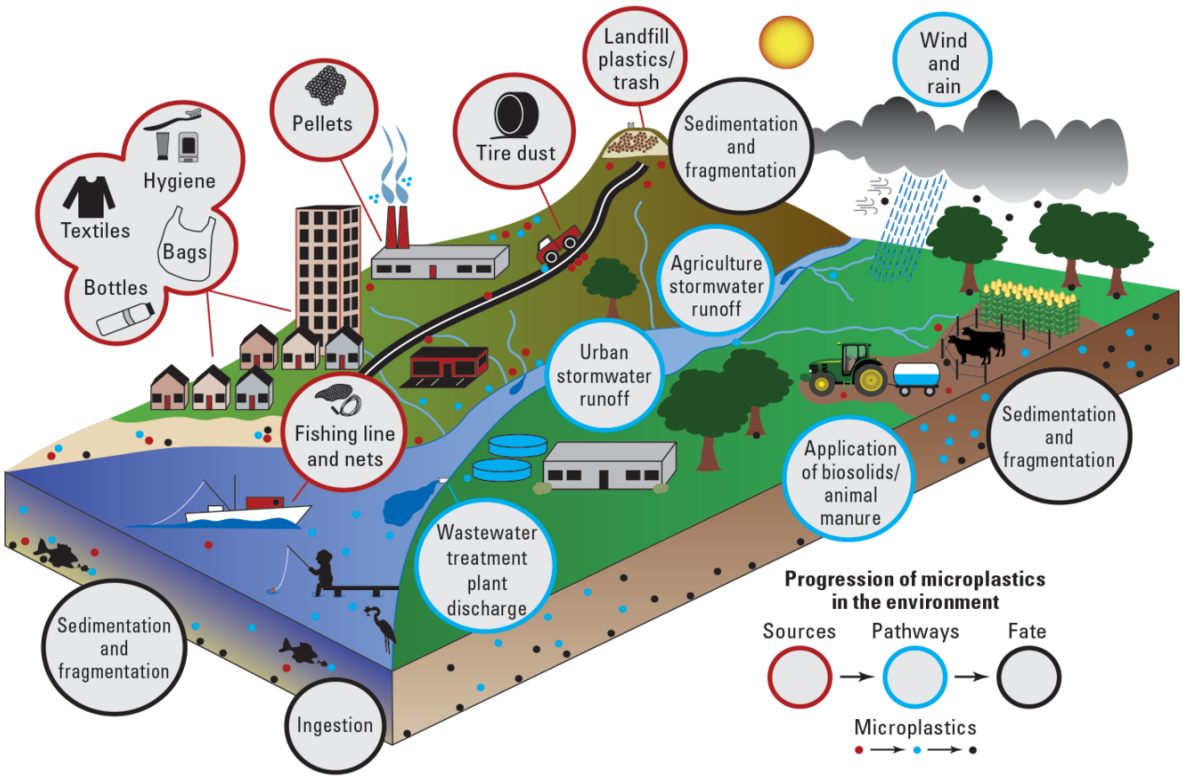

Figure 1 Microplastics sources, pathways and fate conceptual diagram. Retrieved from [3].

Mounting evidence has demonstrated that MP pollution in both marine and freshwater environments poses potential risks to aquatic organisms, disrupts ecosystem functioning, and carries implications for human health [5].The infiltration of MPs into aquatic systems has created a direct pathway to human exposure, as recent studies detected MPs in nearly all seafood samples in the United States [6]. More alarmingly, MPs had been detected in human tissues and organs such as the liver [7], lungs [8], and placenta [9], with recent studies linking their presence in major arteries to heightened risks of heart disease, stroke, and mortality within three years [10]. These findings raises growing concerns about exposure risks for both aquatic organisms and human health.

Among the hydraulic pathways, rivers play a particularly important role in MPs dynamics, serving as the primary route of transport before MPs ultimately reach long-term sinks such as the ocean [11]. At the same time, rivers function both as sources and sinks of MPs depending on flow conditions. Recent studies indicate that under low-flow conditions, fine MPs accumulate in riverbed sediments, creating localized hotspots, while high-flow events can remobilize portions of this stored pollution back into the water column [12]. River infrastructures further complicate these dynamics by unintentionally influencing MP retention. For instance, reservoirs behind dams act as long-term sinks, with sediments trapping MPs and reducing the downstream load compared to upstream inputs [13]. Similarly, low-head weirs have been shown to reduce MP concentrations in downstream waters, primarily by slowing flow velocity in backwater zones and promoting particle settling and retention [14]. Together, these findings highlight the dual role of rivers not only as conduits but also as active regulators of MP fate through both natural hydrodynamic processes and human-engineered structures.

Among various river structures, groynes are notable for their potential to trap MPs, due to their capacity to retain particles. Groynes are dike-like hydraulic structures constructed transverse to river flow [15] and are primarily employed to deflect currents away from erodible banks and regulate flow patterns [16], [17].

Beyond river training, they have also been applied in ecological restoration, as groyne fields can enhance habitat conditions and promote emergent vegetation growth [18]. Groynes are commonly classified by construction material and shape, with the choice depending on local river conditions [15]. Impermeable groynes, usually built emerged and made from rock, gravel, or gabions, are designed to redirect flow farther from the bank while encouraging sediment deposition through eddy formation behind the structure [15], [16], [19]. Particles from the main channel are advected into the groyne fields by primary circulation cells and deposited as flow velocity decreases [20], [21]. This process creates scour near the groyne tips and deposition within the fields (see Fig. 2), resulting in a net import of sediment under most flow conditions [20], [21].

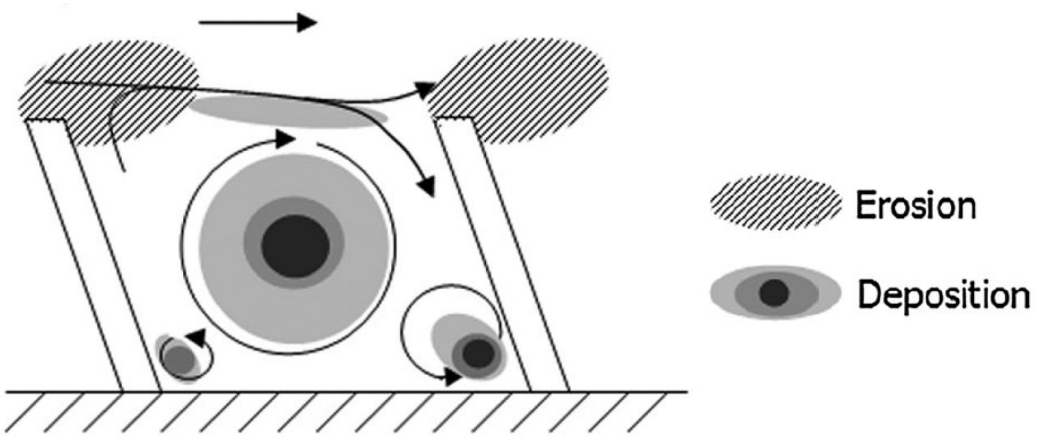

Figure 2 Typical sedimentation pattern within groyne fields of emerged impermeable upstream-facing groynes. Retrieved from [19].

In contrast, permeable groynes, typically constructed from bamboo, timber, or piles, reduce flow velocities and promote sedimentation, making them particularly effective in sediment-rich rivers; these are also better suited for submerged conditions [15], [16]. In the present study, emerged impermeable groynes were selected to reflect the low suspended sediment content of the experimental flow. Apart from materials, groynes also vary in shape, influencing flow contraction, turbulence, and sediment deposition patterns [22]. Further discussion on groyne shapes and particle deposition mechanisms within the groyne field are

provided in Section 3.1. In the present study, emerged impermeable groynes were selected to reflect the low suspended sediment content of the experimental flow, and the shape of the groynes was varied to examine its influence on MPs retention.

1.2 Objectives of the Study

This study investigates the potential of groynes to trap non-buoyant MPs, building on their well-documented ability to generate low-velocity recirculation zones that promote sediment deposition and retention. Given that the transport behavior of non-buoyant MPs closely parallels that of sediments, it is hypothesized that groynes will similarly facilitate MP retention. To test the hypothesis, the study pursues three objectives:

(1) to quantify overall MPs trapping rate of groynes under controlled hydraulic conditions using a particle tracking model;

(2) to examine differences in trapping efficiency among groyne geometries and identify shapes that maximize retention; and

(3) to assess the influence of minor differences in MPs densities on the capture of MPs of different groyne shapes.

The findings are expected to inform the design or retrofitting of groyne systems to enhance MP retention capacity and contribute to broader strategies for mitigating MP pollution in regulated river environments.

1.3 Novelty of the Study

Despite growing field evidence that river infrastructures can retain microplastics, empirical research directly quantifying the trapping efficiency of groynes remains scarce. To date, only one study has examined groynes in this context, focusing on floating macroplastics (>5 mm). Przyborowski et al. [23] demonstrated that lengthening a groyne narrowed the main channel and intensified lateral mixing, thereby

diverting more buoyant macroplastics into downstream recirculation zones. These findings highlighted the potential of groyne fields as strategic interception points for managing plastic debris in rivers.

Building on this foundation, the present study advances understanding by experimentally evaluating the trapping efficiency of groynes for non-buoyant MPs and extending the scope to compare the effects of different groyne geometries and particle densities.

1.4 Scope of the Study

This study focuses exclusively on the trapping efficiency of non-buoyant MPs particles within riverine environments. Buoyant MPs, which exhibit different transport and settling behaviors, are excluded from the scope. Although groynes are commonly found in both riverine and marine settings, this research is confined to river groynes, and therefore marine hydraulic factors such as wave action and salinity effects are not considered. The findings are thus applicable to freshwater fluvial systems where non-buoyant MPs interact with river groyne structures.

1.5 Structure of the Thesis

This thesis is organized into four chapters: **Chapter 1** provides a high-level introduction to the study, outlining its background and study motivation. **Chapter 2** presents a literature review of empirical research on MPs transport in rivers, highlighting common approaches to MPs characterization, interesting experimental designs, proposed empirical formulations, and directions for future investigation. **Chapter 3** takes reference to the literature reviewed in Chapter 2 (e.g., experimental setup, MPs characterization) and details the experimental work undertaken to test the study's hypothesis. The chapter encompasses the experimental methodology, results, and discussion. After that, **Chapter 4** concludes the thesis by synthesizing the main findings in relation to the stated objectives. Finally, **Chapter 5** discusses the methodological limitations of the flume experiments and highlights potential improvements for advancing the environmental relevance of the research.

Chapter 2 Literature Review

2.1 Introduction

Since the 1950s, the rapid growth of industrial plastic use has significantly contributed to environmental pollution, largely due to inadequate waste management practices [24]. Plastics were detected in oceans [24], freshwaters such as rivers and lakes [24], terrestrial soils [25], and the atmosphere [26]. Estimates of 2022 showed that 1.7 million tons of plastic waste ended up in the ocean annually [27], through different pathways including rivers, urban runoff, wastewater discharge, and wind [27], [28]. Among them, microplastics (MPs), generally defined as plastic particles smaller than 5 mm in size, either from direct emission (i.e., primary release) or fragmentation of larger pieces (i.e., secondary release) have become a major concern in recent years [26], [28].

Aquatic microplastics threaten ecosystems, food safety, and health. They act as vectors for pathogens and pollutants, foster harmful microbes, and are easily ingested, leading to bioaccumulation across the food chain [29]. In fact, recent findings have revealed MPs in 98.9% of U.S. seafood samples [6] and in over 80% of tap water samples worldwide [30]. As increasing number of studies had also detected MPs in human organs [31], with emerging evidence linking their presence to various health issues [10], [32].

With oceans acting as the final sinks for MPs [33], it is vital to understand and intervene at earlier stages of their transportation pathway. Notably, a majority of marine MPs originated from terrestrial sources [34], and rivers are a dominant transport pathway [27], [35]. Besides, rivers are not only conduits but also potential sinks for storing MPs temporarily in riverbanks, floodplains, aquatic vegetation, sediments, and infrastructure [36]. Therefore, targeting rivers for monitoring and mitigation can significantly reduce the flow of MPs to the ocean.

The transport processes of MPs in rivers remain poorly understood, with existing freshwater MPs research primarily focusing on sources, distribution, and ecotoxicity, leaving significant gaps in understanding their migration and behavior in riverine environments [37], [38]. Studying aquatic MPs is challenging because they persist in water and constantly transform, with data showing >90% MPs undergo natural weathering from UV light, mechanical abrasion, and biofouling, processes that alter their physical and chemical properties [39], [40]. These dynamic changes complicate efforts to track their fate and environmental impact over time.

Laboratory experiments are a critical tool for addressing these gaps by complementing field observations and numerical models with physical processes insights under controlled conditions. They enable the isolation and quantification of key transport processes while providing parameters for predictive modelling. Laboratory studies are particularly valuable for testing sediment transport analogues in microplastic research, validating theoretical formulations, and reconciling discrepancies between modelled and observed particle behavior [38], [41], [42].

The main objective of this review is to synthesize recent laboratory research on MP transport pathways and transformation effects, with emphasis on studies published between 2021 and 2025. It evaluates how experiments disentangle the roles of physical properties of MPs, ambient flow properties, and how transport processes were parameterized. Accordingly, the review is organized as follows: characterization approaches for MPs are first introduced in Section 2, followed by a brief overview of transformation processes (i.e., biological and physical weathering) of MPs in Section 3, and highlights of various experimental setups are provided in Section 4. Key findings on different transportation pathways (i.e., settlement, dispersion, vertical distribution, near-bed transport, incipient motion, infiltration and retention) are then detailed in Section 5. Finally, Section 6 discusses methodological advances, limitations, and future directions

necessary to ensure laboratory findings remain environmentally relevant and scalable to natural river systems.

2.2 Microplastics Characterization

2.2.1 Polymer Type

Most previous studies selected MP types for experiments based on field sampling data, global plastic production and waste statistics to ensure relevance to real-world conditions. For example, some relied on the most detected MPs in aquatic and sewage environments and used polyethylene terephthalate (PET), polyvinyl chloride (PVC), polystyrene (PS) and polyamide (PA) in their experiment [43]. Others tailored their MP selection to specific ecosystems, in which PA, PVC, PET were selected based on riverbeds samples [44]. Conversely, some studies intentionally selected less prevalent polymers such as polymethyl methacrylate (PMMA), polyoxymethylene (POM), acrylonitrile butadiene styrene (ABS), and polylactic acid (PLA) for their specific physical properties (e.g., density, rigidity, transparency) to isolate and study the effect of a single variable, such as elasticity or surface properties [45], [46], [47].

2.2.2 Source of Microplastics

Most MPs used in the experiment were mostly sourced from suppliers or in-house made, with some being collected from the field. Regularly shaped MPs, such as pellets, cylinders, and spheres, were typically purchased, though some were produced from thermoplastics [48] or via 3D printing [45]. Fibers were usually handmade by cutting common household materials like fishing line [48], broom hair [49], dish brushes [45], dental floss [45], and yarn [50], [51], [52], while some reported obtaining them from sources available online [53]. Fragments were commonly made by grinding or cutting larger plastic items such as food containers [54], disposable cups [50], [55], floor leather [56] and plastic files [57], while some sourced

them from plastic processing facility [53]. To obtain submillimeter MPs, some extracted PE (polyethylene) microbeads from exfoliating cosmetic products using vacuum filtration [58].

Irregularly shaped MPs were generally prepared using a liquid nitrogen grinders [43], [59], centrifugal mills [60] or granulators [61] on larger plastic pieces. On the other hand, some collected MPs from natural water bodies, where the MPs were typically separated by a sieve, rinsed with deionized water followed by air-drying, in order to remove most biofilm, then stored in glass vials in the dark [61], [62], [63].

2.2.3 Quantification of Microplastics

In experimental studies, researchers typically use microplastics with densities between 0.9 and 1.4 g/cm³, reflecting the most commonly found plastic types in aquatic environments or tailored to the specific objectives of the research. For instance, Born et al. [64] selected MPs with densities between 0.91 and 1.13 g/cm³ to ensure they were as close as possible to water density, aiming to examine how small differences in density influence the transport behavior of MPs in flowing water. Among studies which reported their method in density measurement, most reported the use or referencing of standardized procedures, namely ISO 1183-1:2019 or DIN 53 479. These two standards are highly similar as both were based on the Archimedes' principle. In addition to these standard protocols, some determined density using gravimetric methods with known-volume samples [23], [65]. Others used devices like powder density meters [66], pycnometers [60] and density kits [61]. For samples which direct measurements were impractical, the density specifications from the supplier were used.

The size range of MPs used in experiments is broad. Although global and local river data indicate that a notable proportion of MPs in surface waters and sediments have an apparent diameter of less than 0.3 mm [34], [67], larger MPs were selected for experimental practicality reasons, such as the capability of imaging systems [68], [69], the availability of sieves [70] and limitations of cutting method [71]. This size disparity represents a significant challenge in extrapolating laboratory results to predict the behavior of the most

abundant MPs in the environment. Researchers commonly measured the dimensions of MPs by using a digital caliper, or other tools including microscopes [60], [72], laser particle size analyzers [73], [74], micrometers [43] and sieve [46]. For more precise or automated measurements, some studies coupled optical tools with image-based software such as ImageJ [66], [75]. The size of non-spherical MPs was typically expressed in nominal diameter (d_n), diameter of a sphere of the same volume as the given particle, which could be computed or approximated differently depending on geometry (e.g., $d_{n,fiber} = \sqrt[3]{\frac{3ac^2}{2}}$ [51], $d_{n,fiber,plate,disk} = \sqrt{4ab/\pi}$ [52], [76], [77], and $d_{n,irregularly\ shaped} = \sqrt[3]{abc}$ [43], [53], [78]).

To account for the combined effects of particle size and density on microplastic motion, the dimensionless particle diameter (d_*) was sometimes used. For example, Yu et al. [79] studied the streamwise transport behavior of MPs varying in size and shape by normalizing experimental results using d_* enabling consistent comparison. The latter is given by

$$d_* = d_n \sqrt[3]{\frac{g'}{\nu^2}} \tag{1}$$

in which ν is the kinematic viscosity of the fluid; g' is the reduced gravity acceleration, calculated by $g' = \frac{g(\rho_s - \rho)}{\rho}$ [80], where ρ_s is the particle density and ρ is the fluid density.

Apart from particle density and size, some studies also quantified MPs by concentration. Born et al. developed a MATLAB software which divides the flume into equal sections and normalizes concentration profiles by dividing particle counts by that of a reference section [64]. Some measured particle volume concentration by using a laser particle size analyzer for MPs within the device's detection range [73], [81]. Some acquired number and mass concentrations by dividing the total particle count (counted manually or by software like ImagJ) and mass by the liquid volume [62], [73], [82], [83].

2.2.4 Shape of Microplastics

Characterizing MP shape is especially important given their wide variety of shapes which significantly influences their behavior. Although the most frequently observed MP shapes in rivers are fibers, fragments, film then pellets [34], pellets remained the most commonly used shape in experimental studies. Regularly shaped MPs (e.g., cylinders, cuboids, sheets), irregularly shaped particles (e.g., fragments, crushed particles) and fibers were also used in some studies. Researchers typically described MPs shapes using quantitative shape descriptors summarized in Table 1, with the Corey Shape Factor (CSF), which assesses particle sphericity from the ratio of its three principal dimensions, being the most common metric. However, CSF was less used for films, fibers and fragments, as studies showed it was incapable of effectively differentiating between the three [52]. As a result, sphericity, elongation, and flatness (see Table 1 for definitions) were typically employed alongside CSF to provide a more detailed characterization. Yet, there is still no universally accepted method for shape characterization for these particles. Some researchers developed shape factors tailored to irregular MPs based on both experimental and numerical results but acknowledged the difficulty in accurate implementation [84].

Table 1 Common shape factors selected for reference, where a = length of longest side; b = length of intermediate side; c = length of shortest side; A_{sph} = surface area of the volume equivalent sphere; and A_s = surface area of particle [45], [52], [61], [85]. Multiple shape factors exist, and many have alternative formulations. The choice depends on the studied MPs and research objectives.

Shape factor	**Formula**	**Implication**
Corey shape factor (CSF)	$CSF = \frac{c}{\sqrt{ab}}$	CSF = 1: equidimensional; CSF < 1: elongated/flattened [22, 23, 27, 31-33, 40, 45, 46, 52, 58, 59, 64, 66-69]
Sphericity (Φ)	$\Phi = \frac{A_{sph}}{A_s}$	Φ = 1: spherical; $\Phi \neq 1$: deviate from perfect sphere; $A_{sph} = 4\pi\left(\frac{d_n}{2}\right)^2$ [66], [75], [84], [86], [89]. Sphericity can also be approximated by $\Phi = \left(\frac{c^2}{ab}\right)^{\frac{1}{3}}$ [78].
Elongation (e)	$e = \frac{b}{a}$	e > 1: elongated [52], [54], [61], [66], [84]

Flatness (*f*)	$f = \frac{c}{b}$	f < 1: flat [54], [72], [77], [84]
Aschenbrenner shape factor (ASF)	$ASF = \frac{ac}{b^2}$	ASF = 1: spherical; ASF > 1: elongated; ASF < 1: flat [52], [69]

Some researchers also characterized microplastics using parameters that go beyond spatial dimensions. Settling velocity (w_s) is a key parameter to reflect how MPs respond to fluid flow. For example, it was used to characterize MPs in studies on horizontal transport of MPs [66] and sediment-MP interactions [73]. The w_s of a spherical particle shape is given by the Stokes' formula:

$$w_s^2 = \frac{4}{3}\frac{dg}{C_d}\left(\frac{\rho_s - \rho}{\rho}\right) \tag{2}$$

while that of non-spherical particles can be calculated by

$$w_s^2 = \frac{2Vg}{A_p C_d}\left(\frac{\rho_s - \rho}{\rho}\right) \tag{3}$$

in which g is the gravitational acceleration; d is the particle diameter, replaced by d_n for non-spherical particles; C_d is the drag coefficient, a function of pressure drag, friction drag and flow properties; V is the volume of particle; A_p is the projected area of particle; ρ is the density of fluid; and ρ_s represents the density of particle [90]. The dimensionless form of settling velocity (w_*) [72] is given by

$$w_* = \frac{w_s^3}{g'\nu} \tag{4}$$

For non-spherical MPs, w_s was determined experimentally or calculated based on other microplastic studies [47], [64], [66], [73]. Various studies have proposed modifications to C_d to account for the diverse physical properties and irregular shapes of MPs (see Section 5.1).

Other properties of MPs were characterized depending on the study objective. For instance, Wang et al. [43] investigated the influence of surface roughness on settling velocity by visually classifying MP samples as rough or smooth. Lofty et al. [47] examined the role of particle elasticity in bedload transport by

measuring Young's modulus and Poisson's ratio. Goral et al. [45] assessed the absorption capability of MPs by soaking them in water for one week, finding no significant change in density or dimensions, and thus concluding that absorption was negligible.

2.3 Transformation of Microplastics

Upon entering aquatic systems, MPs undergo physical, chemical, and biological changes. The extent and rate of these transformations are influenced by the polymer's chemical and physical properties, as well as environmental conditions such as light exposure, ambient hydrodynamics and biological activity. Common transformation processes could be divided into biotic (e.g. biofouling) and abiotic (e.g., photo-oxidation, mechanical abrasion) pathways. In the context of this review, discussion was focused on biofouling and abiotic weathering, as these processes are more extensively studied and have clearer links to changes in MPs physical properties, which, in turn, affect transport behavior.

2.3.1 Biofouling

Microplastics develop biofilms (i.e., layers of microorganisms and organic matter) once they enter natural waters, which eventually alter their density and polarity [61], [91]. While the effect of biofouling on particle density was detailed in Section 5.1.2, some studies suggested that biofouling changes MPs' polarity from nearly hydrophobic to strongly hydrophilic, which increases their cohesion with sediments [61]. However, this phenomenon was not observed in some studies [91], a discrepancy that may be due to differences in biofilm community composition or sediment type.

The extent of biofouling on MPs is shaped by multiple factors, including particle shape, polymer type, and environmental conditions such as light availability that supports the growth of photosynthetic organisms. The shape of the plastic was found to influence the maximum amount of fouling accumulated per surface unit, with films accumulating more than pellets [86], [92]. Biofouling was also polymer-specific and

Mendrik et al. [91] attributed this variability to differences in chemical composition and surface texture, which likely affect microbial adhesion and biofilm development. These differences extended beyond microbial biofilms to macro-community attachment, as visibly distinct fouling was observed across polymer types under uniform environmental conditions, suggesting the polymer substrate itself influences colonization [92]. For instance, after 63 days of freshwater incubation, biofilm mass varied significantly despite equal surface roughness, with PS exhibiting the lowest biofilm mass and PVC (polyvinyl chloride) the highest [93]. Findings also suggested that increased surface roughness facilitates microbial attachment and enhances biofilm development [56], [93].

2.3.1.1 Biofilm Cultivation Methods

Biofilms on MPs were typically cultivated using either field-based or laboratory-based approaches. Field approaches typically involved submerging fixed microplastic samples in natural waters for more than a month [56], [86], [92], [94]. In laboratory settings, some researchers placed plastic samples in tanks containing natural freshwater, concentrated algal batches collected from the site or unialgal cultures, followed by continuous shaking [58], [59], [61], [94]. Time-controlled fluorescent lamps were used to simulate natural illumination cycle under controlled temperature [59], [61], [94]. Hoellein et al. [50] on the other hand, mixed benthic sediments and overlying water with microplastics in flasks, the mixture was then placed in a shaking incubator for 7 days and stored frozen. The time required for biofouling varies by site, influenced by physicochemical conditions and seasonal fluctuations that determine the colonization of fouling organisms [41], [42]. For example, the required exposure time for biofouling to affect sinking velocities ranged from as short as 1 week to over 3 months [61], [91].

Various methods were employed to quantify biofilm on microplastics. Quantifying biofilm growth on MPs is methodologically diverse and challenging. Gravimetric methods were the most common approach, involving weight comparisons of MPs with and without biofilm. These methods varied in how the biofilm

was removed or isolated, including drying [56], [93], Fenton oxidation [58], or direct comparison of fouled and clean samples [92]. Some studies first used stereoscopic observations to confirm the presence of biofilm layers and attached macro-organisms, followed by optical density (O.D.) measurement using the Crystal Violet staining approach [92]. The resulting O.D. values were measured spectrophotometrically and normalized by MP surface area (O.D./cm²). Some studies quantified biofilm abundance using qPCR targeting 16S rRNA genes, involving DNA extraction, specific primers, and standard curve quantification [50]. Additionally, some studies introduced a Biofilm Distribution Index (BDI), ranging from 1 (uniform coverage) to 5 (irregular distribution), based on average scores assigned by independent observers [86].

Biofilm presence, architecture, and distribution on microplastics was usually visualized through a combination of visual and microscopic techniques to correlate physical structure with its impact on MP properties. Visual observation and Scanning Electron Microscopy (SEM) were frequently used to analyze surface morphology and examine fouling organisms [91], [93], [94], [95]. To further explore biofilm architecture, confocal laser scanning microscopy (CLSM) with multi-color staining was employed to visualize the 3D structure of biofilms [56].

2.3.2 Abiotic Weathering

Weathering mechanisms change the MP properties through various processes such as UV irradiation, hydrodynamic forces, and the wet–dry alternation, which often lead to changes in MP density and buoyancy. For example, experimental results showed the density of virgin PP (polypropylene) dropped from 0.90 g/cm³ to 0.66 g/cm³ after 6 weeks exposure in freshwater environments [56]. Although biofilm was formed, the decrease in density was attributed to the loss of mass from additive leaching [56].

Other common effects include change in surface morphology (e.g., increased roughness or cracks), zeta potential, adsorption capacity, hydrophilicity, formation of new functional groups, or fragmentation. For

example, weathered LDPE pellets showed a 25.6% decrease in diameter compared to 17.3% for virgin LDPE [92]. In particular, UV weathering was found to increase crystallinity and brittleness [54], [55]. It is worth noting that the effects of weathering or aging on MPs are shaped by a range of factors, including the physical properties of MPs and the surrounding environment. For instance, UV radiation and hydrodynamic weathering demonstrated polymer-specific behaviors, such as PMMA becoming more hydrophobic while PE became less [81]. These alterations have direct implications for transport: increased roughness and cracks can enhance drag and aggregation potential; changed crystallinity and density directly alter settling velocities; and increased hydrophilicity can affect interfacial behavior and sediment cohesion.

2.3.2.1 Experimental Procedures for Simulating Abiotic Weathering

Laboratory-induced weathering of MPs has been achieved through a variety of methods to simulate environmental aging under controlled conditions. Photo-oxidative aging was most studied, with most cases having MPs exposed to artificial UV radiation for at least 1 month, usually coupled with gentle shaking [54], [55], [81], [92]. Some further applied a daylight filter to simulate natural sunlight [54]. Chemical and mechanical weathering methods were also employed. Wang et al. [5] used Fenton's reagent to simulate accelerated oxidative aging of MPs over 15 days. Yang et al. [81] simulated mechanical abrasion by agitating MPs with glass beads in deionized water at 100 – 250 rpm, and also mimicked wet-dry cycling by repeating at least 8 cycles of soaking, shaking, and oven-drying.

2.4 Experimental Setups

This section covers common experimental setups such as column tests for vertical motion, and flume experiments that recreate river-like flows to investigate near-bed transport and incipient motion. It also highlights special approaches on MPs injection strategies and tracking techniques.

2.4.1 Column Test

Column tests were commonly used to study the vertical velocity of MPs but have also been adapted to study processes such as vertical mixing and resuspension, as illustrated in the following examples.

Early research on MP settling primarily investigated the influence of their physical properties, with most experiments conducted in quiescent water conditions. In most cases, the tests were conducted with wall effects neglected, though some studies applied wall factors for adjustments [43]. While dealing with small MPs (10 − 388 μm) with very low settling velocities thus highly sensitive to convective flows, Dittmar et al. [96] proposed a setup using a cooling incubator and tennis balls to reduce temperature fluctuations and vibration, thereby limiting the impact of convection.

Meanwhile, some studies employed column-based systems to study vertical mixing of MPs. [62], [97]. Li et al. developed a custom settlement and observation system to study microplastic behavior in sediment-laden turbulence [97]. The device featured a 200 cm-tall settling column with seven motor-driven vibrational grids to generate isotropic turbulence. A 40-cm thick layer of sediment was placed at the bottom of the device to simulate riverbed environments, allowing for the simultaneous observation of MPs aggregation, settling, and resuspension under controlled turbulence.

To investigate the retention of MPs in coarse riverbed sediments, Munz et al. [98] conducted experiments using columns (50 cm long, 8 cm diameter) saturated with medium gravel and coarse sand, simulating coarse riverbed sediments. Flow was induced from top to bottom, mimicking surface water infiltration under a free gradient. Once the flow stabilized, it was briefly paused to allow MPs to be put on sediment surface, after which the column was resealed and flow resumed.

Sediment–water column setup was usually adopted in MP resuspension studies. In one test, resuspension was simulated by inverting the column six times, with 10-minute settling periods between inversions. A

final 2-hour sedimentation period allowed for full particle redistribution [99]. Other researchers collected sediment columns from the field and overlying water was mixed by a vertically oscillating porous plexiglass perforated plate such that resuspension could be facilitated [63].

2.4.2 Flumes

Straight laboratory flume setups were commonly used in studies investigating the longitudinal, near-bed or vertical movement of MPs under controlled conditions. These setups often feature different flow rates, adjustable slopes, varied bed materials, or shallow zones to simulate different hydraulic environments [47], [64], [73], [100].

Flow conditions varied across studies but were consistently monitored and adjusted to simulate realistic hydraulic environments. For example, flow was recirculated in both closed- and open-circuit systems using submersible pumps [83], [101], and hydraulic load (HL) was maintained using piezometers or inlet–outlet elevation control [73], [98]. In particular, to study MP incipient motion, flow was gradually increased until MP particle displacement occurred, with thresholds defined as the point of visible deviation or the departure of 50% of the particles from a test area [5], [45], [102].

Flumes with rough beds composed of fine to coarse sand, gravel, or glass beads were employed to simulate sediment conditions, in which the roughness Reynolds number was used to represent bed roughness [5], [45], [47], [66], [102]. Sediment compaction and saturation were carefully controlled, using techniques such as bottom-up water saturation [98] or sediment support grids with uniform flow distribution [101]. Some tracked bedform dynamics using a side-view camera [82], while others used time-lapse photography [88], Particle Image Velocimetry (PIV) [83], and laser profiling [83] to capture flow velocities, bedform amplitude, and migration.

On the other hand, annular (circular) flumes provide a tightly controlled flow that approximates the Couette flow, making them ideal for observing incipient motion. For instance, some suppressed pump-induced turbulence and minimized secondary circulations by counter-rotating the lid and channel [102]. A custom control program allowed bed shear to be increased at a fixed rate (0.0001 N/m^2s), allowing the first motion of settled MPs to be observed.

Also studying the incipient motion of MPs, the circular flume used by Goral et al. [45] generated flow by lid rotation and thus required a conversion from rotation speed to shear, as well as a small correction for secondary currents. They first calibrated lid velocity to shear velocity by fitting the near-bed velocity profiles (measured by a Laser Doppler Velocimetry device) to smooth wall theory; they then accounted for circular-channel secondary flow via an Engelund-based angle correction. With hydraulically smooth conditions verified, the lid velocity of the fully developed flow was increased by 0.02 m/s, with 3-minute wait after each increment.

To study the infiltration of MPs in migrating bedforms, Alhusban [82] used a paddle-driven annular flume for producing and quantifying ripples. The flow was driven by 8 perforated paddles on the lid, while the flume was filled with quartz sand (0.4 – 0.8 mm), fluorescent MPs (0.2 – 5 mm) and water; three flow velocities were interchanged to create migrating bedforms through sediment motion. Bedform dynamics were monitored by a side-looking, calibrated camera, with flow velocity estimated via particle-tracking velocimetry. After each run, the bed was cored to 10 cm and sliced to map and quantify MPs infiltration. The study concluded that MPs infiltration is controlled mainly by size, with density and flow conditions playing less important roles.

2.4.3 Microplastics Injection

For column tests, MPs were released at least 1 cm below the water surface to minimize the influence of surface tension [43], [53], [72]. For flumes, MPs were introduced in varying ways: water surface placement [73], [98], pulse injection into the flow [83], homogeneous mixing throughout the sediment bed [88], or near-bed placements [5], [45], [47], [66]. In most cases, MPs were soaked in water for at least 4 hours before the test to reduce static surface charge.

In some situations, extra effort was required to avoid issues like clogging the feeding devices or unevenly mixed samples. For example, Dittmar et al. [60] injected small MPs (size = 0.01 – 0.4 mm) from stock suspensions which were pre-mixed with surfactants and degassed. Born et al. used a vibrating feeder provided a steady MP supply, while using different air-free setups for sinking and buoyant MPs [64]. Sinking particles were introduced through a 35° inclined, water-fed pipe into a calm flume zone, while buoyant particles were released just above the water surface to minimize air bubble attachment [64]. Yu et al. introduced MPs into the flow using a plexiglass ramp installed at the top of the flume inlet. The ramp was angled at 45 degrees from the horizontal and divided into 25 evenly spaced slots, with its lower end extending below the water surface [79]. Microplastics were then placed in each of the 25 channels on the ramp, and all were released simultaneously into the flow by removing a barrier plate [79].

2.4.4 Microplastics Tracking

2.4.4.1 Individual Particle

To monitor the trajectory and velocities of individual MP particles, particle movement was captured and analyzed by optical devices frame-by-frame, an approach commonly known as Particle Tracking Velocimetry (PTV) [69], [74], [82], [103]. When needed, multiple synchronized high-speed cameras were used to capture spatial details [64], [66], [74]. MP trajectories were usually captured by backlighting approach [51], [54], [66], [104] or by actively illuminating MPs (sometimes fluorescent coated [82], [87]

or embedded [74], [83], [100], [105]) by strong light (e.g. UV light [82], [83], [87], laser light [100]) to boost contrast and suppress background noise, improving trackability.

Settling velocity (w_s) was usually measured by capturing the falling distance and duration using digital cameras or stopwatches [48], [50]. The measured w_s values were then compared with theoretical models, often drawn from sediment or other MP-related studies. Some studies also captured MPs trajectories, MPs orientation and secondary movement by high speed cameras [51], [60], [104], where images were processed by self-developed scripts [52], [96], [104]. For instance, Choi et al. [69] captured both front and side view of settling fibers with only one camera by utilizing mirror reflection, such that the 3D coordinates of the particle could be reconstructed.

In near-bed studies, particle trajectories and transport modes (rolling, saltation, suspension) were classified using software-based or visual criteria conditions [47], [66], [105]. Detailed particle-bed interactions were captured by having multiple observers to distinguish between short transitory MP retention and longer-term burial events [105].

2.4.4.2 Multi-particle

To quantify microplastic concentrations and movement in a flume, some studies used fluorometric techniques. By staining microplastic with Nile Red, they could be detected by fluorometers, and such data could be converted to concentrations through calibration [46], [106]. Recent studies found the method was reliable for polymers with densities larger then 0.9 g/cm³ and particle sizes less than 150 μm [46]. However, as lighter MPs showed poor detectability, higher initial concentrations or alternative detection methods were suggested [46].

Complementary approaches have enhanced detection capabilities. For example, Xia et al. [63] used a Nile Red–methanol staining protocol combined with laser confocal microscopy and ImageJ analysis, resulted in > 90% detection efficiency for particles ≥ 50 μm. Similarly, Munz et al. [98] used fully stained red fluorescent PS fragments (≥ 100 μm) with defined excitation ranges and fluorescence imaging, reporting 100% recovery with a low false discovery rate. For real-time monitoring, Boos et al. [83] deployed internally fluorophore-coated microbeads and used both portable fluorometers and a Fluorescence Imaging System (FIS) to continuously track microplastic transport and infiltration across water–sediment interfaces, detecting particles as small as 10 μm.

Additionally, recent work has extended fluorometric methods to study MPs dispersion within vegetated channels using Hostasol methacrylate (HMA)-tagged PS MPs, alongside Rhodamine WT as solute tracer [107]. Fluorometer sensor data (10 Hz) collected at multiple channel positions enabled calculation of longitudinal dispersion coefficients via the method of moments, with results confirming minimal tracer loss and highlighting the utility of dual-tracer fluorometry for resolving microplastic transport under complex flow conditions.

2.5 Riverine Microplastics Transport Mechanisms

The transport of particles in hydraulic environments is mainly governed by a balance of three physical forces acting on each particle, namely the gravitational force (F_G), the buoyancy force (F_B) acting upwards and the fluid drag, F_D which is due to the shear stress from the fluid and which acts in the opposite direction to the relative flow velocity [42]. In the vertical direction, the balance between F_G and F_B, supplemented by lift (F_L), determines whether a particle will sink, remain suspended, or float near the surface, with the net balance dictating its vertical position in the water column [41]. Horizontal particle motion is governed by the combination of vertical force balance and F_G, while particles at the bed additionally experience

frictional resistance (F_F) counteracting drag [41]. These force interactions determine whether particles remain immobile, move along the bed, or are suspended [41], [42].

The mechanics of sediment transport in rivers are extensively studied, providing the foundation for understanding MPs movement, which closely mirrors that of natural sediments [46]. However, MPs transport is shaped by the physiochemical properties of MPs particles and the riverine environments [38], as they drive mechanical, photochemical, and biological transformations of MPs [37], [42]. These deviations highlight the importance of accounting for the unique physical properties of MPs, surrounding hydrodynamics [37], and sediment composition [108] when understanding transport.

Microplastics exhibit a wide range of behaviors (Fig. 3) depending largely on their density, size, and surface characteristics [38], [109]. Buoyant MPs remain suspended in the water column, with their vertical position influenced by surface area and size [48], and are readily transported by currents [110]. In contrast, dense MPs tend to sink and move horizontally under stronger flows [57] . Bedload transport primarily occurs through sliding and rolling motions [46], with a portion buried in sediment while others are reintroduced into the flow through resuspension [41], [109]. Vertical transport of MPs is further influenced by external factors such as turbulence and interactions with suspended solids [41], [97].

This section reviews the main transport pathways of MPs in freshwater systems, focusing on (i) settling, (ii) incipient motion, (iii) dispersion, (iv) vertical distribution, (v) near-bed transport, and (vi) infiltration and retention. For each subsection, recent findings into the underlying mechanisms are summarized, supplemented by insights into temporal transformations and newly proposed empirical models where available.

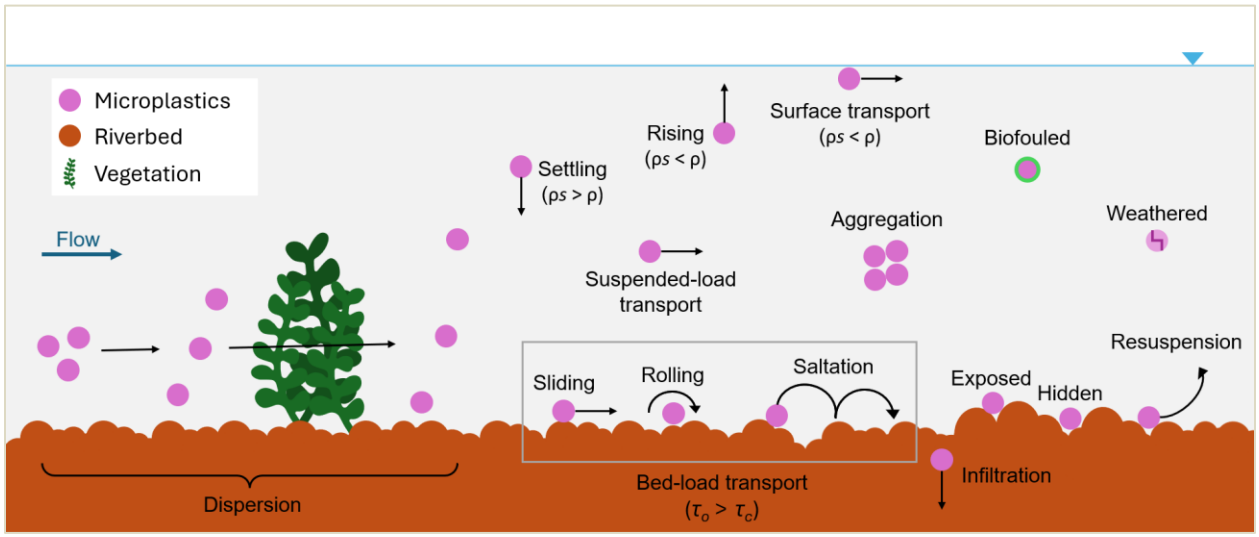

Figure 3 Schematic representation of MPs transport in Rivers.

2.5.1 Settling

Settling velocity (w_s) represents the balance of F_G, F_B, and F_D acting on a particle in static water, where the sinking rate of non-buoyant particle is constant. For positively buoyant particles, the analogous parameter is the rising velocity (or upward terminal velocity), which is conceptually the same physical quantity as w_s but opposite in direction [59]. It is foundational for understanding the vertical transport and concentration profiles of microplastics in aquatic environments, and by far the most well-studied mechanism among other processes.

As shown in Eq. 2, drag coefficient (C_d) is a critical parameter governing w_s. When the particle Reynolds number ($Re_p = \frac{w_s d}{\nu}$) is less than 0.1, C_d is commonly approximated by $C_d = \frac{24}{Re_p}$ for spherical particles. However, in cases where inertial forces become significant ($Re_p > 0.1$) or the projected area (A_p) of the particle is unknown, the relationship between w_s and C_d becomes more complex, thus, an empirical approach is necessary. Across the reviewed studies, modifications on C_d by relating it to MPs size, shape, orientation and shear remained an ongoing effort, while emerging studies focused on the impact of MPs transformation.

This section will focus on the primary factors governing MPs settling in natural flows: (1) their intrinsic physical properties, (2) biofouling, and (3) influence from the surroundings [42].

2.5.1.1 Influence of Microplastics Properties on Settling

The key in formulating settling equations for MPs was to parameterize shape-dependent drag characteristics. Different from sediments, MPs exhibit a greater variety of shapes with a significantly higher proportion of asymmetric and irregularly shaped particles (recall that fibers and fragments are the predominant shapes in river surface water and sediments [34]). Irregularly shaped MPs generally settle more slowly than spherical particles because their complex shapes increase drag [85]**.**

Waldschläger and Schüttrumpf [53] were among the first to compare sediment drag models to existing and their own experiment data on MPs. They modified Stokes' formula (Eq. 2) by incorporating CSF into C_d to capture shape-related variations, particularly for MPs pellets, fragments and fibers (see Table 2). Moving forward, some studies suggested that using both sphericity (Φ) and CSF in parallel was more effective in distinguishing the drag on microplastics with varying geometries [61], [89]. Others highlighted the need to consider three-dimensional settling dynamics on MPs settling, particularly for fibers and fragments, as secondary motion (i.e., rotation, oscillation, or tumbling of particles [48], [65], [69], [72]) can significantly alter the trajectories and settling rates of irregularly shaped particles and standard settling models do not adequately capture [84].

For instance, MPs fibers complicate settling velocity calculations due to their elongated, irregular shapes. Khatmullina and Isachenko [48], being the first to explore this complexity, derived an approximation for long cylindrical MPs by observing a linear relationship between the product of C_d and Re_p (C_dRe_p) and the particle length, which resulted in a revised formula for w_s through algebraic derivation (see Table 2). After

that, Nguyen et al. [51] investigated the settling motion of polyester (PES) textile fibers with various lengths and curliness. It was observed that fibers with a projected length (L_p) ≥1 mm exhibited slower settling when they were oriented more horizontally or curlier. Despite the effect of both factors, the authors suggested that C_d of longer fibers (L_P ≥1 mm) can be reasonably estimated by Re_p (see Table 2).

Table 2 Overview of shape-dependent drag models for MPs settling

Studies	**Equation**	**Microplastics properties**	**Application condition**
Waldschläger & Schüttrumpf (2019) [53]	$C_{d,pellets\ \&\ fragment} = \left(\frac{3}{CSF \times \sqrt[3]{Re_p}}\right)$ $C_{d,fiber} = \left(\frac{4.7}{\sqrt{Re_p}} + \sqrt{CSF}\right)$	Irregularly shaped; d_n = 0.4 – 5 mm; CSF = ~0.1 - 1; ρ_s = 1.01 – 1.37 g/cm^3	Quiescent fluid; neighboring/swarm effects neglected
Choi et al. (2022) [69]	$C_d = \frac{41.28 ASF^{0.49} S_c^{0.82}}{Re_p^{0.7}}$ (Sc is the crosswise sphericity, a shape factor dependent on settlement orientation)	Fibers; d_n = 1.69 – 4.03 mm; ρ_s = 1.31 g/cm^3	Re_p < 160; quiescent fluid; neighboring/swarm effects neglected
Nguyen et al. (2022) [51]	$C_d = \begin{cases} 3.78\, Re_p^{-2}, & for\ fiber\ length = 1mm \\ 7.57\, Re_p^{-2}, & for\ fiber\ length = 2mm \\ 15.22 Re_p^{-2}, & for\ fiber\ length = 4mm \end{cases}$	Fibers (diameter = 16.3 μm); ρ_s = 1.38 g/cm^3; curly	$Re_p \leq 3.01$; quiescent fluid; neighboring/swarm effects neglected
Yu et al. (2022) [89]	$C_d = \frac{\frac{432}{d_*^3}(1 + 0.022 d_*^3)^{0.54} + 0.47[1 - \exp(-0.15 d_*^{0.45})]}{\left(d_*^{-0.25} \phi^{d_*^{0.03}} CSF^{d_*^{0.33}}\right)^{0.25}}$	Various shapes; d_n = 0.26 – 3.56 mm; CSF = 0.01–1.00; Φ = 0.06–1.00; (ρ_s – ρ)/ρ = 0.02–0.56	Re_p = 1 – 300; quiescent fluid; neighboring/swarm effects neglected; particles with low secondary motion
Zhang & Choi (2022) [52]	$C_d = \frac{58.58 ASF^{0.1936}}{Re_p^{0.8273}}$	Fibers, films, fragments; d_n = 0.63 – 4.03 mm; ρ_s = 0.95 – 1.43 g/cm^3	Quiescent fluid; neighboring/swarm effects neglected
Goral et al. (2023) [78]	$C_d = \left(1 + \frac{3.2}{\sqrt{Re_p}} + \frac{32}{Re_P}\right) \cdot \min(0.44 \Phi^{-2}, 1)$	Irregularly shaped; d_n = 0.26 – 3.85	Re_p = 0.4 – 1000; quiescent fluid;

		mm; CSF = 0.01–1.00; Φ = 0.06–1.00; ρ_s = 1.02–1.98 g/cm^3	neighboring/swarm effects neglected
Ji et al. (2024) [84]	$C_d = \exp\left[3.5 \times e^{-1.943 + 2.01 \times e^{-0.07 d_*}} - 0.62 \times ln(ISF) - 0.8\right]$ (ISF is the irregular shape factor which is dependent on particle volume and maximum projected area)	Irregularly shaped; d_n = 0.6 – 3.1 mm; e = 0.28 – 0.98; f = 0.22 – 0.92; ρ_s = 1.2 g/cm^3	Re_p < 400; quiescent fluid; neighboring/swarm effects neglected

On the other hand, Choi et al. [69] showed that including settling orientation and the ASF (see Table 1) in the drag model significantly improved predictions of MP fiber settling over earlier models [48], [52], [53] mainly due to the consideration of secondary motion and the capability of ASF in differentiating fibers, films and fragments (see Table 2). Similarly, for MPs with a preferred settling orientation (i.e., fibers, cylinders, plates and disk), some suggested the use of the shortest edge (c), instead of d_n, as length scale in describing settling behavior [78]. Based on experimental observations, such particles typically settle with their largest surface area oriented perpendicular to the direction of motion. As a result, by rearranging Eq. 2, the research team proposed and proved that c (i.e. $c = \frac{V}{A_p}$) was more accurate and simpler to use [78].

The effect of shape decreases with particle size. For instance, settling motion of MPs fibers with length larger than 5 mm displayed orientation dependence but not shorter fibers [69], [104]. One study examined the settling velocity and motion of small MPs (size between 0.01 and 0.4 mm), and compared the experimental results with predictions from 10 existing settling models [60]. The findings revealed that models specifically developed for MPs (size larger than 0.5 mm) generally overestimated w_s of small MPs, while those developed for general particles performed better. In another recent study, Dai et al. [104] investigated the settling of MP fibers with lengths between 0.3 and 0.6 mm under laminar flow conditions.

Due to the significant discrepancy between the predicted C_d from existing models and those obtained experimentally, the aforementioned authors proposed a new C_d equation for short MPs fibers (length < 0.6 mm) which incorporates orientation angle, ASF, and particle Reynolds number, Re_p. Both studies highlight the important differences in settling dynamics between small MPs and those larger than 0.5 mm, underscoring the need for further research focused on the smaller size range.

Apart from refinements on C_d, some researchers proposed other ways. Francalanci et al. [65] introduced CSF-dependence into the coefficients of the Ferguson and Church (2004) empirical model for sediments to improve predictions for irregularly shaped MPs as shown below:

$$w_* = \frac{d_*^2}{C_1 + (0.75 C_2 d_*^3)^n} \tag{5}$$

Instead of using Eq. 4 to calculate w_*, the researchers suggested incorporating the shape-adjusted d_* into the calculation. Other empirically derived coefficients in the equation, namely C_1, C_2 and exponent n, also depended on geometric shape descriptors. Some other researchers also proposed equations to predict MP settling velocity based on various shape factors by using empirical fitting approaches (see Table 3).

Table 3 Overview of terminal velocity models for MPs of different shapes.

Studies	**Equation**	**Microplastics properties**	**Application condition**
Khatmullina and Isachenko (2017) [48]	$w_s = \frac{\pi}{2}\frac{1}{\nu} g' \frac{ab}{55.238a + 12.691}$	Fibers (diameter = 0.15 – 0.71 mm, length = 0.5 – 5mm); ρ_s = 1.13 – 1.17 g/cm^3	Re_p = 2.5 – 635; quiescent fluid; neighboring/swarm effects neglected
Kaiser et al. (2019) [85]	$w_s = 11.68 + 0.1991(ac^2)^{\frac{1}{3}} + 0.0004(ac^2)^{\frac{2}{3}} - 0.0993(\rho_s - \rho) + 0.0002(\rho_s - \rho)^2$	Irregularly shaped; d_n = 6 – 251 μm; ρ_s = 1.14 – 1.39 g/cm^3	$Re_p << 1$; $d_n \geq 25$ μm; salinity 0, 15 or 36; quiescent fluid; neighboring/swarm effects neglected
Francalanci et al. (2021) [65]	$w_* = \frac{d_*^2}{18a^{-0.38}\left(\frac{a^2+b^2+c^2}{3}\right)^{-0.19} + (0.2781 CSF^{-0.1602} d_*^3)^{0.4942 CSF^{-0.059}}}$	Pellets, fragments; d_n = 0.63 – 5.44 mm; CSF > 0.068;	Re_p within viscous to turbulent flow regime; quiescent

		ρ_s = 0.95 – 1.43 g/cm^3	fluid; neighboring/swarm effects neglected
Wang et al. (2021) [43]	$w_s = 1.0434\left(\frac{\rho_s - \rho}{\rho}\right)^{0.495} \frac{d^{0.777} CSF^{0.71}}{\nu^{0.124}}$	Near-sphere, irregularly shaped; d_n= 0.27 – 2.33 mm; ρ_s = 0.95 – 1.43 g/cm^3; CSF = ~0 – 1	Re_p = 1 – 1000; quiescent fluid for ρ_s < 1250; neighboring/swarm effects neglected
Yang et al. (2023) [77]	$\log(w_*) = -6.314 + 4.204\log(d_*) - 0.918\log(d_*)^2 + 0.101\log(d_*)^3 - 0.004\log(d_*)^4$	Plates (side length = 1.5 – 5 mm, thickness = 0.15 – 0.5 mm); ρ_s = 1.04 – 1.34 g/cm^3	Re_p = 20 – 200; quiescent fluid; neighboring/swarm effects neglected

2.5.1.2 Environmental Drivers Influencing Settling

All above-mentioned studies on MP settling velocities were conducted under static conditions, typically using settling columns, which were suitable for examining the influence of particle-intrinsic properties but insufficient for capturing environmental conditions, such as turbulence, sediment interactions, salinity, and transformation processes like biofilm formation, and aggregation. Emerging laboratory studies have begun to incorporate these environmental factors, particularly biofouling, to better replicate real-world conditions and improve the understanding of microplastic settling in aquatic settings.

Impact of Biofouling on Microplastics Settling

Biofouling plays a critical role in MP settling by altering particle density, orientation, and surface properties. The colonization of MPs by microorganisms adds biomass that increases the overall mass, volume and density of the plastic–biofilm complex, generally enhancing settling velocity [50], [56], [95]. Experiments showed that after 44 days of incubation, PET and PVC squares displayed higher densities and faster settling than their pristine counterparts [56], and biofouled PES fibers showed a 35% density increase and correspondingly faster settlement [86]. Some studies even reported that biofilm presence had the strongest influence on settling velocity, regardless of suspended sediment concentration, with an average 40% and maximum 130% increase [91]. In some instances, biofouling has converted buoyant PE MPs films

(5mm) into negatively buoyant particles within 6 weeks that remained submerged for over a year [94]. Notable, biofouling is not always sufficient to turn buoyant microplastics non-buoyant. In some cases, even with 30% increase in total mass after 12 weeks of incubation, buoyant PE microbeads continued to float [58].

In addition to increasing density, biofilms can also affect settling by modifying particle drag. For instance, it was reported that biofouled buoyant films rose up to 3 times faster than their pristine counterparts, likely due to increased drag from water trapped within the biofilm layer [92]. In some cases, uneven colonization enhances hydrodynamic drag and destabilizes motion, leading to slower descent, as seen with dense PET sheets [86]. Thus, while biofouling typically increases MPs settling through density augmentation, its effects may be moderated by particle shape and biofilm distribution.

Effects of Microplastics Properties on Biofouling

The polymer-dependent nature of biofouling was reflected in the distinct variations in settling behavior. For MPs with similar shapes, low-density plastics required approximately 100 days to exhibit significant sinking velocity changes, while high-density polymers responded within 35 days [92]. However, the extent of these changes was not uniform; for example, PVC fragments showed smaller increases in settling velocity than PET fragments [91].

The shape of MPs strongly influences how biofouling affects their settling behavior. Biofilm colonization was less extensive on fibers compared to pellets and fragments, as evidenced by lower gene copy counts on fibers [50]. Moreover, biofouling was observed to have a pronounced effect on the settling velocity of MPs films but little impact on spherical pellets [61].

The influence of biofouling on MPs settlement is size-dependent. For larger buoyant MPs, such as MPs films (side widths of 5 mm) with surface area-to-volume ratios < 100, microbial biofilms alone are typically insufficient to induce sinking [94]. Instead, biofilm colonization primarily reduces surface hydrophobicity, allowing these plastics to submerge just below the surface [94]. In some cases, when biofouling caused buoyant MP fragments (e.g., PP) to sink in freshwater, it was observed that smaller MPs (125 – 250 μm) transitioned to a sinking state earlier than their larger counterparts (325 – 500 μm) [59].

Biofouling's effect on MPs settling is also highly dependent on MPs density. For non-buoyant MPs (e.g., PET, PS), biofilm growth followed an exponential pattern during a 63-day incubation period while this pattern was absent in buoyant MPs like LDPE (Low-density polyethylene) and PP, likely due to their intermittent exposure to air and limited submersion, which restricts continuous microbial colonization [93]. Supporting this, Principal Component Analysis of another study revealed that density significantly contributed to the variation in biofilm-induced settling behavior among different MPs films [92].

Empirical models have been developed to quantify the effect of biofouling on microplastic settling. Kooi et al. [111] introduced the first theoretical model, though it did not account for salinity gradients or suspended sediments. Later, Karkanorachaki et al. [92] proposed an empirical relationship linking time, biofouling, and settling velocity, independent of the microplastic's physical properties:

$$u_{\infty} = \frac{A}{1 + e^{-B(t-C)}} \tag{6}$$

where u_{∞} is the terminal sinking velocity in the absence of walls; A, B and C are the coefficients determined by fitting experimental data; and t is the biofouling exposure time. Notably, parameter A reflects the maximum sinking velocity that the MPs can attain, with higher values in fouled samples, indicating that biofouling increases settling or rising potential.

In contrast, Jalón-Rojas et al. [86] adapted existing drag-based formulations by modifying the model proposed by Dellino et al. [112] with a multiplicative correction factor linked to the Biofilm Distribution Index (BDI), a parameter that quantifies how evenly biofilms colonize the MPs film surface:

$$C_{D,film} = \frac{0.9297}{\Psi^{5.05} Re_p^{0.0799}} BDI^{0.573} \quad (7)$$

where Ψ is the shape factor dependent on sphericity (Φ), particle perimeter and the perimeter of the circle equivalent to particle maximum projected area; and BDI ranges from 1 (uniform biofilm) to 5 for highly irregular distribution. The adjustment demonstrates that while uneven colonization reduces settling velocity despite increase in MPs density due to biofouling [86].

UV Weathering

On the other hand, some studies showed that weathering also affects the settling motion of MPs by altering their density, especially under UV radiation. This occurs because UV exposure can lead to regular packing of polymer chains, forming denser crystalline parts within them [54], [55]. For example, crystallinity in PS MPs disks increased from 0% to 37% after UV weathering, contributing to a higher density and a 53% increase in settling speed [55]. Apart from density change, the aforementioned authors also suggested the increased hydrophilicity due to aging further promoted faster settling by reducing drag forces acting on the MPs [55]. Complementing these findings, UV-aged PET and PS microplastics also showed accelerated settling, with average terminal velocities increasing by 4.56% and 37.32%, respectively, after 60 days of exposure, in which the authors also attributed to increased density resulting from enhanced crystallinity [54].

Aggregation

Microplastics in aquatic environments interact with suspended materials such as inorganic sediments and organic detritus, which results in altered settling behavior. While some studies have documented the positive influence of sediments on MP settling [74], [113], there remains a lack of quantitative assessments

on the impact of sediment aggregation on microplastic settling velocity. Mancini et al. [87] conducted settling experiments on MPs of varying shapes and densities, both with and without suspended sediment. Results showed that for MPs with w_s lower than sediments, the presence of sediments significantly increased the settling velocity of most MPs, particularly those with lower CSF (e.g., 105% - 150% increase in w_s for MP fiber), due to enhanced turbulence and particle interactions. Their experiments with sediments yielded results consistent with the proposed equation of Francalanci et al. [65], except that the exponent n required slight adjustments for MPs rougher and stickier, promoting further aggregation with other suspended particles and subsequent settling [50], [95].

Turbulence

Ijaz et al. [75] investigated the impact of turbulence on MPs settling by conducting experiments in a recirculating flume, where non-buoyant spherical MPs were tracked using both top-view and side-view cameras. A relationship between C_d and Re_p, in line with Rouse model, was observed for Re_p = 35 – 640. To better account for the variability in the data, the authors proposed a more explicit model (R^2 = 0.7) that relates C_d to shear velocity (u_*) and the settling velocity in still water (w_s):

$$C_d = \frac{9.4851 u_*}{w_s} + 0.3268 \tag{8}$$

Additionally, they observed that the settling of MPs with diameter ≤ 2 mm with Stokes numbers < 0.52 was enhanced by turbulence, while noting more investigations were needed to validate this pattern for other types and shapes of MPs.

Research on MPs settling has centered on shape-dependent drag, with numerous studies modifying C_d to account for diverse particle geometries, orientations, and sizes, especially shapes where secondary motions complicate predictions. While some models generalized across MPs shapes, others were tailored to specific shapes such as elongated fibers. A growing number of studies examine transformation processes, notably biofouling, which generally accelerates settling by increasing density but can reduce velocity under uneven

biofilm distribution; empirical models have been proposed to link exposure time and biofilm distribution to settling dynamics. UV aging similarly enhances settling by increasing crystallinity, density, and hydrophilicity of polymers. Interactions with suspended sediments and organic matter promote aggregation and higher settling velocities, particularly for irregular MPs. Turbulence was also found to enhance the settling MPs with low Re_p, with studies linking C_d to shear velocity and still-water settling velocity. Despite these advances, no universally accepted drag or settling model has been established across different MPs shapes, the distinct behavior of submillimeter MPs compared to larger ones remains an open research topic, and the combined impacts of transformation processes and turbulence on settling are still poorly understood. Together, these findings underscore that MP settling is governed by an interplay of particle morphology, transformation processes, and environmental drivers, but key uncertainties limit predictive capability.

2.5.2 Incipient Motion

The initiation of sediment motion in open channel flow occurs when the destabilizing forces acting on a particle (i.e., F_D, F_L and F_B) exceed the stabilizing gravitational force (F_G) [80]. Once this threshold is surpassed, particles begin to move and can be classified as either “bed load” or “suspended load” [80]. Bed load transport begins when the bed shear stress (τ_o) exceeds a critical value threshold, known as the critical shear stress (τ_c), while its dimensionless form is referred as the critical Sheilds parameter (θ_c) [80]. These parameters plays a central role in sediment transport mechanics and is typically determined using the Shields diagram or through controlled physical experiments [90]. Nonetheless, the Shields diagram was designed for uniform sediments. In systems with non-uniform particles, the 'hiding–exposure effect' plays an important role [37]. For example, smaller MPs resting among larger particles are shielded from the flow, resulting in a higher critical shear stress for their entrainment, and vice versa [102].

At lower flow velocities, motion of non-buoyant MPs aligned with predictions from classical Shields sediment transport theory [46]. Yet, in most cases, MPs tended to initiate motion at lower shear stresses

than natural sediments, primarily due to their distinct shape and density combinations. Studies consistently observed that most microplastic data points fall below the classical Shields curve, indicating earlier incipient motion [45], [102]. This shift has been attributed to the lower critical shear stresses required to initiate microplastic movement, which resulted from their lower densities and irregular shapes compared to natural sediments [66], [102]. This behavior was reflected in the newly proposed phase diagram, which showed a shallower slope compared to that of natural sediments [66].

2.5.2.1 Factors Influencing Microplastics Incipient Motion

The incipient motion of MPs is influenced by a combination of MPs properties, including shape, density, and aging. Shape plays a role in erosion behavior through its impact on drag and lift forces. Spherical MPs tend to initiate motion more easily due to their minimal bed contact, requiring less force to dislodge, and were observed to move earlier than smaller or less dense pellets. In contrast, fibers require higher shear stresses, as they can become entangled in sediment pores [102]. While shape influences motion onset, Goral et al. [45] found that once static friction and hiding–exposure effects were accounted for, shape parameters such as sphericity or CSF had no additional significant effect. Apart from MPs shape, multivariable regression revealed that critical shear stress (τ_c) depends strongly on the combined effects of particle density, diameter, and shape, as well as sediment grain size [102]. Besides, aging has been shown to increase the critical velocity required for MPs motion, with effects varying based on particle density, size, and bed roughness [5].

Bed roughness significantly influences MPs incipient motion by increasing critical shear stress, primarily through sheltering effects [44], [102]. MPs on rough beds require higher τ_c to be mobilized compared to those on smooth beds [44]. Experimental results also showed that low-density, small-grain MPs were more easily affected by rough beds (i.e., higher incipient velocity) [5]. This results from the inherent susceptibility of such MPs to fluid entrainment, which amplified the rough bed's influence on their movement [5].

2.5.2.2 Modelling Microplastics Incipient Motion

Recent advancements in empirical formulas for predicting MPs incipient motion have focused on incorporating key sediment interaction effects, including hiding–exposure, static friction, and sheltering.

Waldschläger and Schüttrumpf [102] was the first to transfer the hiding–exposure concept to MPs and developed an equation for estimating θ_C of MPs on natural sediment beds (see Table 4). Goral et al. [45] demonstrated that accounting for the lower static friction between plastics and sand shifts MPs data closer to the classical Shields curve. They also showed that the hiding–exposure function effectively captures the reduced exposure effect for particle-to-grain size ratio $d_n/d_{50} \geq 10$ (see Table 4). Building on existing studies, Yu et al. [44] modified the existing power-law relationship between τ_c of MPs and MP size, as shown in Table 4. Their proposed formula reduced prediction errors by approximately 40% compared to existing models, with average relative errors of 21.7% and 15.8% for low and high density MPs, respectively. Meanwhile, Wang et al. [5] enhanced existing incipient velocity model for fine sediments to improve prediction accuracy for aged MPs, yet the sheltering effect was not considered as idealized rough sediment bed was used in their experiment [5].

Table 4 Proposed empirical models which describes MPs incipient motion.

Studies	**Equations**	**Parameters**	**Application conditions**
Waldschläger and Schüttrumpf (2019) [102]	$\theta_c = 0.5588\theta_{c,sed}\left(\frac{d_n}{d_{50}}\right)^{-0.503}$	θ_c = critical Sheilds parameter of MPs; $\theta_{c,sed}$ = critical Sheilds parameter of bed sediment; d_{50} = median size of sediment grains.	Shape of MPs = Pellets, fragments, fibers; d_n = 0.75 – 5.04 mm; ρ_s = 1.01 – 1.37 g/cm^3; d_{50} = 0.45 – 3 mm
Goral et al. (2023) [45]	$\theta_c = \mu_s^*[0.165(Re_s + 0.6)^{-0.8} + 0.045\exp(-40Re_s^{-1.3})] \cdot \Lambda\left(\frac{d_n}{d_{50}}\right)$ in which	μ_s^* = ratio of the static friction coefficient of plastics to that	Shape of MPs = irregularly shaped; d_n = 0.26 – 3.85 mm; CSF =

	$Re_s = \frac{d_{50}u_*}{\nu}$ $\Lambda\left(\frac{d_n}{d_{50}}\right) = \max\left[\left(\frac{d_n}{d_{50}}\right)^{-0.8}, 0.15\right]$	of sediment; Re_s= grain Reynolds number; $\Lambda\left(\frac{d_n}{d_{50}}\right)$ = hiding-exposure function; d_{50} = median size of sediment grains.	0.01–1.00; Φ = 0.06–1.00; ρ_s = 1.02–1.98 g/cm^3; d_{50} = 0.18 mm; hydraulically smooth flow
Yu et al. (2023) [44]	$\begin{cases}\frac{\tau_c}{\tau_{cs,50}} = 0.103\left[\frac{(\rho_s-\rho)d_n}{\rho D_{50}}\right]^{150.98d_n} & for\ \frac{(\rho_s-\rho)}{\rho} \le 0.11 \\ \frac{\tau_c}{\tau_{cs,50}} = 0.166\left[\frac{(\rho_s-\rho)}{\rho d_{50}}\right]^{0.562} & for\ \frac{(\rho_s-\rho)}{\rho} > 0.11\end{cases}$	$\tau_{cs,50}$ = critical shear stress of sediments of median size; d_{50} = median size of sediment grains.	CSF = 0.2–1.0; ρ_s = 1.01–1.4 g/cm^3; d_n = 0.75–5.04 mm; d_{50} = 0.5–5.0 mm; roughness Reynolds number = 26 – 94
Wang et al. (2024) [5]	$u_{*c} = 0.76\left(\frac{h}{d_n}\right)^{0.14}\left[\frac{(\rho_s-\rho)}{\rho}gd_n + 0.000000246\left(\frac{10+h}{d_n^{0.9}}\right)\right]^{0.5}$	h = flow depth	CSF = 0.78–0.9; ρ_s = 1.11–1.37 g/cm^3; d_n = 0.52–2.52 mm; d_{50} = 0.5–5.0 mm; MPs aged by Fenton reagent; hydraulically smooth flow

Overall, studies on incipient motion highlight that MPs mobilization is strongly controlled by particle shape, density, and bed roughness, with fibers and irregular fragments showing lower critical thresholds than spheres. Recent empirical models, adapted from sediment transport frameworks, capture these influences by incorporating the hiding–exposure effect, frictional properties, and particle aging, thereby extending applicability beyond uniform sediments. However, current formulations remain limited by a reliance on simplified laboratory conditions and narrow flow conditions. Future work should expand testing to finer particles, transformed MPs (e.g., biofouled), and mixed beds to improve predictive accuracy and better represent the heterogeneous conditions of natural rivers.

2.5.3 Dispersion

Few empirical studies examined the dispersion of MPs. Yet recent studies revealed submillimeter spherical MPs (ρ_s = 0.94 – 1.40 g/cm^3) exhibited transport behavior closely resembling that of solutes under a range of hydraulic conditions, which enabled the application of the advection-dispersion equation ($R^2 > 0.95$) across various MP concentrations [46]. Supporting this, the measured longitudinal dispersion coefficients (D_x) for MPs and the solute showed no significant difference and displayed a consistent linear increase with flow velocity in well-mixed water column [46], [107]. The measured D_x also matched with theoretical values predicted by the Chikwendu's N-zone model [46], [107], which divides the water column into N discrete vertical zones. The longitudinal dispersion is expressed as:

$$D_x(N) = \sum_{j=1}^{N-1}\left[\frac{\left(q_1 + q_2 + \cdots + q_j\right)^2\left[1 - \left(q_1 + q_2 + \cdots + q_j\right)\right]^2\left[u_{1,2\ldots j} - u_{(j+1)\ldots N}\right]^2}{b_{j(j+1)}}\right] + \sum_{j=1}^{N} q_j D_{xj} \quad (9)$$

where D_{xj} is the longitudinal diffusivity within zone j; q_j is the fractional depth of zone j, defined as the ratio of the zone thickness (h) to the total flow depth (H); $u_{1,2\ldots j}$ is the mean velocity of zones 1 through j; and $u_{(j+1)\ldots N}$ is the mean velocity of zones $j+1$ through N [114]. The $b_{j(j+1)}$ term is the vertical diffusivity between adjacent zones j and $j+1$, which is calculated by

$$b_{j(j+1)} = \frac{2D_{zj(j+1)}}{H^2\left(q_j + q_{j+1}\right)} \quad (10)$$

where $D_{zj(j+1)}$ is the vertical diffusivity, and can be estimated using Elder's scaling:

$$D_{zj(j+1)} = \kappa u_* H q(1-q) \quad (11)$$

where κ represents the von Kármán constant which is 0.4 [115].

Beyond classical dispersion behavior, MPs also showed superdiffusive transport. Yu et al. [79] observed scaling diffusion exponents (γ) ranging from 1.58 to 1.77 over a dimensionless time interval of 0.06 – 10.0, values comparable to those reported for continuously mobilized sediments. The diffusion exponent γ quantifies how particle spreading deviates from normal diffusion, in other words, characterizes how the

variance of particle displacement (σ_x^2) grows with time (Δt) through the scaling law: $\sigma_x^2 \propto (\Delta t)^{2\gamma}$ [116]. With $\gamma > 0.5$, the diffusion of MPs falls into the superdiffusive regime where particles spread faster than normal diffusion, which typically happens when particle motions are correlated (e.g., inertia, continuous motion) [116]. The similarity of γ values for MPs and sediments suggests that, despite differences in material composition, MPs can follow analogous dispersive dynamics when moving near the bed.

2.5.3.1 Influence of Microplastics Physical Properties on Dispersion

To date, experimental investigations have relied on spherical MPs, the influence of non-spherical geometries on longitudinal transport dynamics remains unaddressed. Stride et al. [46] showed that spherical MPs ($d \leq 150$ μm) with density within 0.94 – 1.32 g/cm³ exhibited longitudinal dispersion patterns comparable to solutes at velocities above 0.101 m/s, while lighter (e.g. PP, $\rho_s = 0.9$ g/cm^3) and denser (e.g. PVC, $\rho_s = 1.4$ g/cm^3) MPs ascended to the water surface and settled, respectively. It was only when velocities were increased to >0.169 m/s that denser polymers remained suspended in the water column [46].

The study showed that while solute transport models can reliably predict dispersion for spherical MPs under most riverine conditions, deviations emerge at low velocities where density governs deposition and resuspension dynamics. As this effect might be amplified for fibers and fragments whose shape could modify buoyancy and drag, extending such experiments to non-spherical geometries would provide valuable insights for improving our understanding of microplastic transport in rivers.

2.5.3.2 Role of Turbulence on Microplastics Dispersion

Flow structure and turbulence further shape MPs dispersion patterns. Shear-induced dispersion was found to decrease with vertical distance from the bed, as higher D_x values were recorded near the bed surface [46]. Additionally, streamwise velocity fluctuations increased with particle Shields parameter (θ_p), highlighting the role of shear velocity in intensifying near-bed turbulence and MP velocity variability [79]. It was also

suggested that the 'diffusive effect' of turbulence could cause dispersion on bed-load microplastic, as observed in the broadened distribution of saltation length, saltation height, and saltation transport velocity with higher relative turbulent forces [47]. Such variability reflects the increased stochastic influence of turbulence on particle saltation dynamics.

2.5.3.3 Role of Vegetation on Microplastics Dispersion

Guo et al. [107] revealed that vegetation significantly enhanced dispersion of spherical MPs, particularly at higher flow rates. In canopy-covered channels, MPs diffusivity increased by 10 – 40 times compared to unvegetated conditions [107]. This increase was linked to the observed shift in the dominant mixing mechanism where turbulence generated by plant–flow interactions became the primary driver, instead of shear-induced velocity gradients. When these authors ran the N-zone model, results showed that under canopy conditions the turbulence-induced term (i.e., second term in Eq. 9) dominated the longitudinal dispersion process, while the shear-induced term (i.e., first term in Eq. 9), usually the main driver in open-channel flows, became comparatively minor [107] .

The distance between successive rows of plant arrays (i.e., canopy spacing) was also found to significantly influence D_x of MPs. The same study compared two scenarios with vegetation spacing of 1.5 m and 0.5 m respectively [107]. In the denser canopy setup, turbulence length scales were less than half those observed in the other scenario. The authors attributed this to higher flow resistance and increased wake turbulence in denser arrangements, which in turn allow the flow to adjust more gradually to velocity changes [107]. As a result, under denser canopy conditions, D_x was more sensitive to event small changes to since the persistent wakes amplified particle dispersion along the flow [107].

Building on the proven effectiveness of the Chikwendu's N-zone and Elder's models at capturing spherical MP dispersion coefficients (RMSE values <0.006) [46], Guo et al. demonstrated that the N-zone model,

when combined with modifications based on existing turbulent diffusivity prediction equations (Eq. 9), accurately estimated longitudinal dispersion in vegetated and unvegetated channels [107].

They further developed a framework to model turbulent diffusivity and vertical profiles of turbulent kinetic energy (k_t) based on canopy morphology and spacing, where the resulting N-zone model yielded dispersion predictions with acceptable accuracy. As mentioned in Section 5.2.3, the presence of aquatic vegetation shifted the primary mixing mechanism from shear-induced to canopy-driven turbulence. Given this turbulence-induced regime, the authors adopted the turbulent diffusivity theory proposed by Nepf (1999) such that longitudinal and vertical diffusivity could be computed by the following:

$$D = \alpha\sqrt{k_t l_t} \tag{12}$$

where α is the scaling factor dependent on the solid fraction of the vegetation; and l_t is the integral length scale [117]. The empirical factor, α, was optimized by fitting to observed longitudinal dispersion data, with distinct values for dense and sparse plant arrangements, independent of flow rate.

To estimate l_t, the authors proposed a model based on canopy morphology and spacing by fitting to experimental data:

$$l_t = \begin{cases} \frac{1}{5}(z - 0.03) \times C_{cs} \times Q, & z < 0.075\ m \\ (-0.013z + 0.0097) \times C_{cs} \times Q, & z \geq 0.075\ m \end{cases} \tag{13}$$

where z is the depth; C_{cs} is a dimensionless parameter dependent on canopy spacing (for experiments with spacings of 0.5 m and 1.5 m, C_{cs} was set as 1 and 0.5 respectively); and Q is the flow velocity. It was observed that l_t peaks near the bed and scales with flow rate and canopy spacing, with larger coherent structures forming in sparser canopies due to wake expansion.

Meanwhile, k_t was computed as the sum of bed- and vegetation-induced turbulence kinetic energy using existing models. The model incorporated measured velocity profiles, plant frontal area density, average

canopy volume fraction and estimated drag coefficients and an empirical constant proportional to vegetation-induced turbulence.

Overall, dispersion studies suggested that solute transport models can adequately capture the spreading of spherical MPs under most flow conditions, but deviations arise at low velocities where density-driven deposition and resuspension dominate [46]. Vegetation has been shown to further enhance dispersion, with empirical models successfully reproducing canopy-induced turbulence effects [107]. However, as these findings remain largely restricted to spherical MPs, extending investigations to fibers and fragments, whose irregular geometries alter buoyancy and drag, would be essential to improve predictive capability and ensure dispersion models remain representative of natural riverine transport.

2.5.4 Vertical Distribution

The Rouse model, originally developed for sediment transport, is a classic framework used to describe how particles are distributed vertically within a flowing water column. It links the settling velocity of particles to the upward mixing effect caused by turbulence.

The key parameter in this model is the Rouse number (P), which is determined by:

$$P = \frac{w_s}{\beta \kappa u_*} \tag{14}$$

where β is the diffusion parameter. The dimensionless number expresses the balance between vertical particle motion driven by gravity or buoyancy and turbulent entrainment. Depending on this balance, particles can travel close to the bed, remain suspended throughout the water column, or be carried at the surface.

The importance of the Rouse model lies in its ability to provide predictive concentration profiles of particles across the water depth and classify particle transport modes (e.g., bedload, wash load). Originally applied

to sediments with densities around 2.65 g/cm^3, there has been discussion on its ability to predict the vertical distribution of MPs [118], which exhibit a comparatively lower and more diverse range of densities.

2.5.4.1 Application of Rouse Framework to Microplastics

Recent studies have used the Rouse number P to predict the transport mode of MPs, showing good agreement for spherical MPs with densities higher than water, particularly in distinguishing between suspended and bed load transport [47], [64]. For MPs less dense than water, Born et al. [64] confirmed that the framework can be extended through negative Rouse numbers by testing nearly spherical plastics with densities below that of water (ρ_s = 0.91 – 0.94 g/cm^3). This demonstrates that P is effective not only for sediments but also for plastics of contrasting buoyancy, offering a consistent framework for classifying their dominant transport modes (see Table 5). While this supports the conceptual extension of the Rouse model to positively buoyant MPs, the authors emphasized that further refinement is needed for use, especially to account for the diminished shear stress at the free surface and the unique surface-related forces acting on plastics [64].

Table 5 The Rouse number ranges for transport modes of floating MPs proposed by Born et al. were listed below [64]. *The wash-load transport threshold is defined as the point at which half of the particle concentration is distributed at mid-depth in the water column.*

Mode of transport	**Suggested Rouse number range**
Wash load	$-0.6 < P < 0.8$
Rising suspended transport	$-1.8 < P < -0.6$
Surface transport	$P < -1.8$

The measured vertical concentration distributions of both sinking and buoyant spherical MPs were also compared with Rouse-calculated profiles [64]. Overall, there was a good fit across particle types, with

deviations observed at higher turbulence and flow velocities, suggesting reduced accuracy under strongly non-uniform conditions. As the Rouse formula assumes particle sphericity and uniform flow, researchers cautioned that limitations remain for more turbulent regimes and for particle shapes and sizes beyond the spherical granules and pellets tested in their study [64].

2.5.4.2 Role of Turbulence on Vertical Distribution of Microplastics

Turbulence of the ambient environment plays a critical role in controlling the vertical distribution and transport of MPs in aquatic systems as it counteracts settling and rising velocities by generating both upward and downward flow fluctuations. Using ADV to measure turbulent kinetic energy (k_t) at 5 mm depth increments, studies showed that as k_t increased, concentration profiles of MPs (ρ_s = 0.91 – 1.13 g/cm^3) shifted, highlighting the influence of flow conditions on vertical MP distribution [64]. Besides, k_t was highest near the bed due to steep velocity gradients, indicating that the most vigorous vertical mixing occurs near the channel bottom. As a result, particles in this region are more easily entrained and suspended [64], [100].

Molazadeh et al. [100] also demonstrated the dominant role of turbulence over bed composition in controlling PE particle motion by showing that particle velocity variability remained consistent across bed types but decreased with lower turbulence intensity. On the other hand, experimental results of Yang et al. [81] showed that turbulence outweighed the influence of MPs size, or even MPs density given the turbulence was sufficiently strong, in determining MPs vertical motion. For instance, while PMMA (ρ_s = 1.19 g/cm^3) settled under mild turbulence, it exhibited a maximum floating rate of 34.4% under intense turbulence. Floating or settling rate was quantified based on changes in MPs concentration in the bottom proportion of sampled volume while turbulence was controlled using a shaker, with mild and intense turbulence corresponding to 100 rpm (turbulent kinetic energy dissipation rate, ε = 0.14 W/kg) and 250 rpm (ε = 1.90 W/kg), respectively [81].

Increased turbulence and higher flow velocities promote the entrainment of buoyant particles, often carrying them down to the bed [64], [100]. Experiments showed that the vertical velocity of buoyant PE particles in turbulent flow was 4 times different from their predicted rise velocity under quiescent conditions [100]. Particle motion within the water column was facilitated by flow eddies as rapid conveyance of particles both upwards and downwards was observed [100]. Such turbulence-induced mixing is influenced by external drivers like wind, waves, river discharge, and thermal gradients, all of which modulate MP fate beyond gravity and buoyancy alone [100].

For sinking MPs, increased flow velocity and turbulence shift their transport mode from bedload to suspended load, with particle concentrations moving upward exponentially [64]. This suspension effect is less for larger particles. For instance, 3 mm PA6 particles showed markedly lower concentrations in the water phase compared to 1 mm PA6 under the same conditions. Overall, less buoyant, larger, or irregularly shaped MPs tend to be mixed deeper than smaller, more buoyant ones, highlighting the role of particle properties in determining vertical distribution [100].

Building on the turbulence-scaling framework introduced by Chor et al. (referred as floatability parameter in original text) [119], DiBenedetto et al. [62] characterized vertical mixing with a Rouse-type parameter M, computed as

$$M = \frac{RV}{u_*} \tag{15}$$

where RV is the rising velocity, characterizing MPs buoyancy while u_* characterizes turbulent mixing induced by water surface shear. By computing the M value for MPs samples, they could be sorted into 3 regimes: surface-trapped ($M > 2$), partially mixed ($0.5 \leq M \leq 2$) and well-mixed ($M < 0.5$) [62]. For the partially mixed regime, MPs concentration decreases with depth in an exponential manner:

$$c(z) = c_0 e^{\frac{z}{L_m}} \tag{16}$$

in which $c(z)$ is the MPs concentration at depth z; c_0 is the surface MP concentration; and L_m is the mixing length scale (fitted to experimental data). In the partially mixed regime, the upward flux driven by particle buoyancy (which depends on MPs properties such density and shape) is counteracted by the downward turbulent flux, producing an exponential decay in concentration with flow depth. By extrapolating MPs concentration of the remaining 2 regimes, then integrating and summing the vertical distribution of each regime, the total concentration was acquired. As a result, the regime-specific approach increased the estimated concentration by 47% relative to a single-profile fit and is thus recommended to reduce underestimation of total MP load. Notably, the MPs in this study were mixed by wind shear and breaking waves, such insights were transferable to rivers only if the dynamical differences are explicitly accounted for [62].

For non-buoyant MPs in shallow and unidirectional flow, some studies suggested the vertical transfer of MPs followed a streamwise exponential decay due to sediment-induced deposition [73]. MP concentration at distance x downstream is given by $C_{max} \cdot e^{-K_x}$, where C_{max} is MPs concentration at source; and K_x is the sedimentation rate. Experimental result showed the exponential law held across all runs, and K_x increased linearly with suspended-sediment concentration [73].

2.5.4.3 Factors Influencing Resuspension of Microplastics

Similar to the downward motion (see Section 5.1), MPs resuspension is influenced by particle size and density. Smaller MPs (50–100 μm) are more readily resuspended than larger ones (100–500 μm), as shown by Xia et al. [63]. Density and shape also play key roles. Low-density MP films exhibit more heterogeneous vertical distributions, while high-density fibers dominate in the water column post-disturbance [99]. Interestingly, some low-density MPs still settle on the sediment surface. The authors attributed the unexpected settling of low-density MPs to aggregation with sediments, disturbance effects, and particle

shape, with certain forms such as films being especially prone to surface deposition due to their large surface area and deformation behavior, particularly in fine sediments where interactions enhance trapping [99].

Flow energy also had a huge impact on MPs resuspension, potentially converting sediments from MPs sink to source. In Boos et al. [83], 95% of stored MPs were resuspended in 191 seconds under high-flow conditions, compared to over 300 seconds in low-flow scenarios. Similarly, Yang et al. [120] found that resuspension rates increased with mixing energy, particularly for low-density MPs (ρ_s = 0.89 to 0.98 g/cm³), with a critical energy dissipation threshold of 0.02 – 0.14 W/kg. In high-energy states, over 60% of low-density MPs were resuspended within the first 10 minutes, highlighting the heightened mobility of low-density MPs under turbulent conditions. Li et al. [97] also observed that increasing turbulent shear strength enhanced MP resuspension from sediments into the water column.

To conclude, research on vertical distribution underscores that particle properties and turbulence jointly determine whether MPs remain suspended, settle, or accumulate near the surface. While the Rouse model and its extensions capture key trends for both buoyant and sinking particles, deviations under strong turbulence and for irregular geometries suggest that existing formulations are insufficient. Recent development on transport mode-based approaches have improved predictions of MPs vertical profiles, though their application on riverine settings requires adjustment for differences in turbulence dynamics. Future work should expand experimental efforts beyond spherical MPs, refine turbulence-scaling approaches, incorporate resuspension dynamics, and integrate surface-related forces to ensure vertical distribution models remain representative of real riverine conditions.

2.5.5 Near-bed Transport

Microplastics, particularly nonbuoyant types, exhibit classical near-bed sediment transport modes, namely rolling, saltation, and suspension, similar to natural sediments [66]. Although some material-specific

differences were observed in energy loss upon impact, the Rouse number (see Eq. 14) was shown to effectively characterize key saltation trajectory features (i.e., saltation length, height and velocity) for spherical MPs and spherical natural grains [47].

2.5.5.1 Influence of Microplastics Shape on Near-bed Transport

Particle shape plays a role in MP near-bed transport behavior. During bed-load transport, particle motion is governed by the combined action of hydrodynamic forces, gravity, and inter-particle interactions [80]. For spherical grains, force balance can be reasonably described by particle size and density, whereas irregular geometries modify both the magnitude and orientation of acting forces, leading to altered thresholds for motion [45]. For instance, spheres typically exhibit more predictable saltation trajectories, while fibers and fragments are prone to rolling, sliding, or erratic bouncing due to uneven torque and asymmetric impacts [47]. Shape also influences how particles interact with the bed surface due to the hiding-exposure effect (more details in Section 5.2), thereby modifying the critical shear stress required for continuous motion [44].

As a result, studies have shown that fibers tend to remain suspended longer, while spherical particles exhibit greater mobility along the bed [66], [102]. This influence is further supported by Principal Component Analysis, which revealed that shape descriptors such as CSF, elongation, sphericity, and aspect ratio collectively explain up to 55% of the variance in transport stages [66].

2.5.5.2 Role of Sediment Bed on Microplastics Near-bed Transport

As anticipated, bedload transport of MPs was strongly influenced by sediment bed composition and topography. Yu et al. [79] found that bed roughness (k_s) was the only factor, compared to flow velocity, and density (ρ_s), nominal diameter (d_n), shape of MPs, which was statistically significant on the scaling

diffusion exponent γ (more details in Section 5.3) by conducting a multiple linear regression analysis (p-value < 0.001). For instance, γ decreased from 1.73 to 1.66 when k_s increased from 0.5 mm to 2.5 mm.

On the other hand, Isachenko and Chubarenko [105] found that MPs tend to accumulate in trapping zones formed at transitions from finer to coarser sediments, particularly affecting smaller or more flexible MPs. At finer sediment zones, retention is primarily driven by contact friction, while in areas where particle and sediment grain sizes are similar, direct interactions (e.g., MPs transport orientation, sediment pore shape and size) dominate. This localized trapping driven by particle–bed interactions can play a more decisive role than flow variations. MPs remained in trapping zones even under increased shear stress. This could be explained by the hiding–exposure effect where the probability of MPs motion decreases when they encounter a coarser bottom, increasing their likelihood of remaining trapped [105].

2.5.5.3 Empirical Models for Near-Bed Dynamics of Microplastics

Although Rouse number (Eq. 14) was able to distinguish between bed-load and suspended-load transport of spherical MPs, it was insufficient for distinguishing between saltation and rolling/sliding, yielding a low R^2 of 0.223 [47]. To improve predictive accuracy, Lofty et al. [47] proposed a modified Rouse number, $k_s w_s/du_*$, which incorporates bed roughness (k_s), particle size, settling velocity, and shear velocity. This formulation combines settling-turbulence balance (i.e., w_s/u_*) and the effect of bed roughness relative to particle size (i.e., k_s/d) [47]. The modified Rouse number substantially improved the correlation (R^2 = 0.817), highlighting the critical role of bed roughness and particle scale in determining the dominant near-bed transport mode. Notably, the performance of the modified Rouse number for non-spherical microplastics remains untested [47].

In contrast, Al-Zawaidah et al. [66] focused on the ratio of shear velocity to settling velocity (u_*/w_s), or referred as the transport stage, rather than P, as the former was considered more appropriate in describing

near-bed dynamics, thus enabled clearer characterization of near-bed MPs motion. They then introduced a phase diagram based on transport stage that effectively predicts microplastic motion regimes. Their analysis showed that mean forward velocity (U_p) and mean vertical position in the water column (Z_p) are strongly correlated with transport stage, fitting well to a power function as confirmed by multivariable ANOVA.

Recent studies found that MPs streamwise velocities (v_x) followed a normal distribution under all tested conditions. To parameterize this distribution, they proposed new equations linking the ensemble mean of v_x to flow and particle dynamics. Specifically, the mean velocity (μ_{vx}) was expressed as a function of bed shear velocity (u_*) critical shear velocity (u_{*c}) [79]:

$$\bar{v}_x = 13.67(u_* - 0.76u_{*c}) \quad (17)$$

The linear equation was selected over other multivariable equations based on better empirical fit (relative error of 5.2%) and clearer physical interpretation (last term of Eq. 17 identified as disentrainment threshold, i.e., $0.76u_{*c}$). The equation is valid for a range of MPs (d_n = 2.8 – 4.2 mm; ρ_s = 1.2 – 1.4 g/cm3; CSF = 0.58 – 0.89), bed roughness (k_s = 0.5 – 2.5 mm) varying flow velocities.

In general, near-bed transport of microplastics largely mirrors that of natural sediments but is strongly modulated by particle shape and bed roughness. Fibers and fragments displayed less predictable trajectories than spheres, while bed composition and roughness govern trapping and mobility, often overriding flow effects. Although classical frameworks such as the Rouse number capture broad transport regimes, recent studies have proposed alternative frameworks to better classify and predict rolling, saltation, and short-term burial. Future research should extend these formulations to irregular and sub-millimeter particles, and integrate localized trapping processes to better represent riverine near-bed dynamics.

2.5.6 Infiltration and Retention

Microplastic retention in sediment beds has been experimentally shown to range from 2% to 40%, indicating their role as long-term sinks [88]. Field observations confirmed that small microplastics (< 0.5 mm) dominate river sediments, comprising over 80% of detected particles [63]. Recent laboratory studies further highlight that infiltration into sediments is governed by a complex interplay of factors, including particle size, shape, and density, as well as sediment grain size and hydrodynamic conditions.

2.5.6.1 Influence of Microplastics Physical Properties on Infiltration

Microplastic infiltration into sediments is strongly size-dependent, with smaller particles penetrating deeper and exhibiting greater vertical mobility. Studies have shown that MPs abundance decreases exponentially with depth, with larger particles (0.5 – 2 mm) retained in the upper 5–30 cm, while particles < 500 μm reached depths up to 50 cm [98]. Similarly, Alhusban [82] observed that 3–5 mm MPs were confined to the top 3 cm, whereas the smallest particles reached as deep as 7 cm. These findings were supported by regression analyses showing particle size had a statistically significant effect (p-value < 0.05) on maximum infiltration depth, exerting a stronger influence than either celerity (i.e., the migration speed of sediment bedforms, calculated as ripple displacement over time) or density [82]. Fluorescence Imaging System (FIS) monitoring further confirmed that maximum infiltration depth declined with increasing particle size and that larger particles exhibited delayed infiltration onset. For instance, 3 μm particles began infiltrating at 152 seconds, while 10 μm particles did not begin until 449 seconds [83].

The shape of MPs plays a critical role in determining retention and burial within sediments. Spherical MPs were found to be most readily retained, while irregular pellets exhibited lower burial potential, indicating that shape governs mobility [88]. MPs with low CSF, such as fibers, showed less deep infiltration compared to more spherical MPs. This suggests that higher CSF values are associated with greater vertical mobility of microplastics [101].

2.5.6.2 Role of Sediment Bed and Flow Rate on Microplastics Infiltration

Sediment grain size also influences MP infiltration and retention. In fine sediments (40–80 μm), high-density MPs tended to accumulate deeper in the sediment column, while in coarse sediments (>630 μm), they remained near the surface [98], [99]. Fine sands also trapped MPs for longer durations compared to coarse sands [83]. Some studies suggested that the relationship between microplastic and sediment size was crucial for infiltration, with the size ratio, d_{max}/d_{50} (i.e., d_{max} = maximum diameter of MPs, d_{50} = median size of sediment grains), proposed as a key indicator. Lower ratios facilitate deeper infiltration, whereas higher ratios ($d_{max}/d_{50} > 1$) result in greater accumulation at the sediment surface [101].

Bedform dynamics play a significant role in MP infiltration. The study found that faster bedform migration (higher celerity) results in less microplastic being retained in the sediment, showing that retention decreases as bedform speed increases [88]. Flume experiments further showed that taller and more mobile bedforms promoted greater infiltration. Log-transformed regression analysis revealed a positive correlation between particle abundance and distance from stationary sediment layers, highlighting the influence of bedform height on vertical particle transport [82].

Hydrodynamic conditions influence microplastic infiltration, particularly within the superficial sediment layer. Flow-induced shear promotes deeper infiltration and redistribution but has limited effect beyond the surface [98], [101]. Experiments showed that the percentage of MPs infiltrating below the superficial layer increased from 52.7% to 61.3% when hydraulic load increased from 0.25 m to 1 m [101], and that higher flow rates enhanced penetration depth [98]. Field data from river sediment further confirmed seasonal variations in MPs accumulation within bed sediments led by hydrodynamic variations [63].

2.5.6.3 Empirical Models for Microplastics Infiltration

Munz et al. [98] effectively adapted the filter coefficient (λ) originated from earlier filtration studies to quantify MPs retention and predict maximum penetration depths in saturated riverbed sediments. The colloid transport framework of Bradford et al. [121] is grounded in first-order deep bed filtration theory and describes how particle concentrations decrease exponentially with depth due to mechanisms such as attachment, straining, and interception. Building on the framework, Munz et al. [98] applied λ to model the exponential decline of secondary polystyrene fragments with depth, based on a first-order reaction kinetics framework, and systematically related it to key hydrogeological parameters. The relative MP abundance at a specific depth was therefore represented by the following:

$$\frac{C_L}{C_{Tot}} = e^{-\lambda_L \cdot z} \tag{18}$$

in which C_L is the concentration of MPs of size L; C_{Tot} is the total MP concentration; λ_L is the filter coefficient of a clean filter medium with respect to particle of size L; and z is the depth within the sediment column. A low λ_L indicated deeper penetration (weaker filtering), while a high λ_L reflected stronger surface retention. To evaluate λ_L, the authors fitted an exponential decay function to measured retention profiles, yielding optimized λ_L values ranging from 0.18 to 1.0 cm^{-1} for different experimental conditions. They developed a generalized multiple linear regression model linking the logarithm of λ_L to dimensionless flow velocity, microplastic size, and sediment grain size ($R^2 = 0.92$, p-value < 0.01), which showed λ_L increases with particle size but decreases with flow velocity and sediment grain size. Among the predictors, sediment grain size had a slightly greater effect than flow velocity, which echoed with the above-mentioned findings.

To conclude, infiltration and retention processes highlight the riverbed's role as a dynamic sink for microplastics. The processes are primarily regulated by MPs size and shape, while smaller and more spherical particles exhibit greater vertical mobility, coarse sediments and high bedform celerity limit long-term burial. Laboratory studies demonstrated that trapping zones and hiding–exposure effects can anchor MPs even under elevated shear. Although classical deep-bed filtration frameworks and filter coefficients

provide useful means to quantify retention, empirical models for infiltration remain largely lacking, and findings are highly sensitive to experimental conditions. Moreover, studies explicitly addressing the influence of transformation processes and turbulence on MPs infiltration are scarce.

2.6 Conclusion

This review synthesized laboratory investigations on the characterization, transformation, and transport of MPs in riverine systems. Across these studies, it is evident that MPs' fate is governed by an interplay between particle-specific properties, such as shape, size, density, and surface conditions, and external environmental drivers including turbulence, vegetation, sediment composition, and bed roughness. While sediment transport theory provided a useful foundation, MPs' irregular morphologies, broad density spectrum, and ongoing transformations introduced complexities that require tailored approaches [37], [42].

Laboratory studies revealed that MPs in rivers are transported through multiple pathways, each shaped by particle traits and environmental conditions. Settling was the most extensively studied transport mechanism. MPs' irregular geometries and densities created wide deviations from sediment models, requiring shape-corrected drag formulations [53], [69]. Transformation processes, particularly biofouling and UV weathering, could shift buoyant plastics into sinking states or alter drag profiles [84], [86]. Sediment aggregation and turbulence further modified settling rates [87]. Despite advances, models remained inconsistent for sub-millimeter MPs and irregular shapes [85].

Regarding incipient motion, experiments demonstrated that MPs mobilized at lower shear stresses than sediments, reflecting their lower density and distinct morphologies [45], [102]. Fibers and elongated fragments, however, often required higher thresholds due to entanglement and torque effects [44]. Bed composition and hiding–exposure effects further influenced entrainment [45]. While Shields-based frameworks provide a useful starting point, polymer- and shape-specific adjustments are still needed [5].

Similarly, dynamics are shaped by MPs' size, density, and morphology, while some studies also examined the effects of turbulence and the presence of vegetation. Under high flows, MPs often mimicked solute dispersion patterns [46], while at low velocities or in vegetated channels they deviated, showing clustering and enhanced mixing [107]. Fluorometric detection methods improved measurement of dispersion coefficients [46]. Vegetation-driven turbulence emerged as a critical driver of MPs dispersion but remains underexplored [107].

Vertical concentration profiles depend on settling, turbulence, and resuspension. Rouse-type models captured general patterns but underestimated irregular and near-neutrally buoyant MPs [64]. Turbulence intensity and resuspension thresholds exerted greater control over vertical structure, dictating whether MPs accumulated at the surface, remained suspended, or settled to the bed [99]. Mode-based approaches combining rolling, saltation, and suspension improved predictive skill but remain limited for irregular morphologies [47]. Within the bed-load transport regime, non-buoyant MPs exhibited sediment-like behaviors such as rolling, saltation, and suspension, but shape and bed roughness drove strong deviations [66]. Fibers and fragments displayed less predictable trajectories than spheres, while rough or coarse beds promoted retention and burial [47]. Empirical refinements to Rouse-based models incorporating bed roughness and transport stage improved predictions, though irregular and small MPs remain poorly represented [105].

When looking at the infiltration of bed-load MPs, riverbeds acted as temporary sinks for MPs, with retention rates ranging from 2% to 40% in laboratory studies [101]. Smaller and spherical MPs tended to penetrate deeper, while fibers and pellets remained trapped near the surface. Sediment grain size, biofilm development, and bedform migration further shaped retention depth and persistence [83]. Empirical

infiltration models based on filtration theory successfully reproduced concentration declines with depth [82], but the influence of surface chemistry and charge remains underexplored [93].

In conclusion, laboratory research has significantly advanced understanding of MPs transport in rivers, revealing the central role of morphology, density, and transformation in shaping settling, motion, dispersion, vertical distribution, near-bed transport, and infiltration. Yet, bridging the gap between controlled experiments and the complexity of natural rivers remains the foremost challenge. Developing predictive tools that integrate particle-specific and multi-stressor dynamics will be critical for quantifying MPs fate across scales and, ultimately, for informing effective monitoring and mitigation strategies to reduce microplastic pollution in freshwater systems.

2.7 Discussion

The size of microplastics selected for experiments has not always reflected those observed in natural riverine environments. Field datasets indicated that many particles in surface waters and sediments were smaller than 0.3 mm [34], [67], whereas most lab studies focused on particles within 0.3 – 0.5 mm, mainly for practical reasons. Although studies are increasingly using MPs with a broader range of characteristics, discrepancies were often observed between laboratory evidence and field observations of riverine MPs. More studies proved differences in settling, and vertical distribution for < 0.5 mm particles compared to larger counterparts [60], [63], [104], but similar studies of other transport process remained scarce. To address this gap, future experiments should incorporate advanced particle-tracking techniques such as laser-induced fluorescence and fluorescence imaging systems, which enable real-time detection of sub-millimeter MPs [83], and fluorescent tagging, which enhances visibility for understanding both the interaction between MPs and the surrounding fluid and the motion of MPs within the bulk flow [82], [87]. In parallel, coupling with particle image velocimetry (PIV) would allow simultaneous resolution of flow structures and particle

trajectories, thereby capturing fine-scale interactions that govern transport, deposition, and resuspension dynamics of small MPs [41].

The shapes of microplastics used in laboratory studies also fail to capture the dominance of fibers and irregular fragments observed in rivers. Fibers and irregular fragments, which took up 75% of MPs detected in surface water and sediments in rivers, remained underrepresented relative to spheres or other regular shapes. Overall, shape influences on transport other than basic settling have not been examined systematically. Processes like dispersion, shear-layer mixing, infiltration, and vertical concentration profiles have seen limited testing with realistic non-spherical particles (e.g., curled fibers, thin films). Rouse-based profiles have been evaluated across narrow shape–size ranges and mostly under steady flows [47], [64]. Performance under variable turbulence, near-surface, and for elongated or sheet-like particles is unclear. This suggests that the dominance of fiber-like MPs in nature is not yet well represented in experimental frameworks.

Unlike natural sediments, which exhibit a relatively uniform density of ~2.6g/cm^3, MPs span a much wider range. This variability means that MPs of different polymers can float, remain neutrally suspended, or sink, making density a fundamental determinant of their transport mode and vertical distribution. While non-buoyant MPs generally follow transport behaviors comparable to sediments (e.g., settling, vertical distribution), fewer studies focused on MPs with densities close to or equal to that of water. When plastic density is close to that of water, even small deviations from buoyancy neutrality cause large shifts in rise velocity and mixing, creating an intermediate regime where turbulence, buoyancy, and particle size interact in complex ways, making their transport much harder to predict [122]. Among the studies reviewed, only Born et al. [64] directly addressed the effects of minor differences in MP densities by showing that MPs with densities near water (0.91–1.13 g/cm^3) exhibited sharply different transport behaviors. These near-

neutrally buoyant polymers present distinct challenges, as their vertical distributions are highly sensitive to turbulence and remain poorly constrained in laboratory studies [122].

Finally, particle-specific attributes provide another important frontier for future investigation. Some particle attributes were also seldom measured alongside transport. Polymer-specific wettability and surface charge vary across polymers and with aging but were rarely paired with transport metrics in flumes. Increased surface roughness and biofilm can shift contact angles and charge, processes that plausibly modify drag and aggregation with minerals or organic flocs [58], [93], [94]. Studies also showed that polymer-dependent zeta potentials (i.e., the electrokinetic surface potential influencing particle stability in suspension) could lead to different MP fates [120]. Finally, emerging flume and visualization studies showed that interactions with bedforms and porous beds control infiltration and retention, but routine co-measurement of particle wettability with sediment exchange remains uncommon.

The environmental fate of MPs in natural waters is ultimately governed by the interplay of multiple dynamic behaviors, such as turbulence, presence of vegetation, biofouling and MPs weathering, rather than single processes in isolation [41]. Yet, as reflected in most of the reviewed studies, the interaction between these mechanisms and environmental conditions remains insufficiently understood. Though a growing body of studies now tests combined drivers (e.g., dispersion in the presence of vegetation [107]; mixed effect of turbulence, aging and hydrophobicity on vertical distribution [120]; settlement in the presence of sediments [87]), such multi-stressor experiments remain comparatively scarce relative to single-factor design. For instance, while recent studies showed that adding realistic turbulence or bedforms alters settlement and MP retention [75], [88], many laboratory investigations continue to rely on steady, uniform conditions in straight flumes.

The interaction between MPs and sediments deserves greater research attention because it fundamentally shapes multiple transport processes, including settling, infiltration, and bed load dynamics. Studies highlighted that high concentrations of suspended particles in rivers enhance the likelihood of MPs forming heteroaggregates, particularly once biofouling occurs and under turbulent conditions, resulting in flocs that markedly alter settling rates and vertical distributions [37], [41]. Beyond the water column, the properties of the sediment bed govern the initiation and mode of bed load transport, with factors such as grain size distribution and hiding–exposure effects determining thresholds for motion (Section 5.2). Supporting this, Isachenko and Chubarenko [105] demonstrated that MPs tend to accumulate in trapping zones created at transitions from finer to coarser sediments, further underscoring that MP–sediment interactions can dictate localized retention and long-term fate.

A recent study by Park and Nepf [123] showed that biofilms on sediment beds reduce the deposition of fine, non-cohesive particles, including microplastics, compared to bare sand under similar flow conditions. This suggested that the effectiveness of the trapping zones described by Isachenko and Chubarenko [105] depends on biofilm presence as clean or lightly coated sediments may trap particles, while heavy biofilm coverage can limit burial and increase resuspension. Thus, trapping zones may be especially effective in environments with limited biofilm growth but less so where biofilms are abundant. This is an example of how the environmental fate of MPs in natural waters is ultimately governed by the interplay of multiple dynamic processes, highlighting the need to consider both transport mechanisms and environmental conditions together.

These gaps in research emphasize the need for more comprehensive studies that integrate both hydrodynamic and sedimentological factors to better understand MP behavior in natural riverine environments. To better understand MPs transport requires shifting from simplified laboratory setups to approaches which capture the complexity of natural river systems. Since MPs dynamics are governed not

only by physical properties such as size, shape and density, but also by transformation processes like biofouling and interactions with sediments. Future research should combine transport mechanisms with various hydrodynamic conditions, thereby integrating turbulence, variable flow regimes, and particle heterogeneity into both experiments and models to bridge the gap between controlled studies and environmental reality.

Chapter 3 Experimental Study on Trapping Efficiency of Non-Buoyant Microplastics by River Groynes

3.1 Introduction

Since the 1950s, the rapid expansion of industrial plastic use, coupled with inadequate waste management, has become a major driver of environmental pollution [24]. Microplastics (MPs), small plastic particles less than 5 mm in diameter, have been detected in diverse environments, including oceans, rivers, lakes, terrestrial soils, and even the atmosphere [25], [26], with 2022 estimates indicating that 1.7 million tons of plastic waste enter the ocean each year [27]. The ecological and health risks posed by aquatic MPs are significant: they can transport pathogens and pollutants, promote harmful microbial growth, and are readily ingested by aquatic organisms, leading to bioaccumulation through the food chain [29]. Alarmingly, MPs have also been detected in human organs [124], with emerging evidence linking their presence to various health impacts [10], [32].

Most marine MPs originate from terrestrial sources, with rivers acting as the primary transport pathway [34], [35] and the oceans serving as the final sinks [33]. However, rivers also function as temporary storage zones for MPs, retaining them in riverbanks, floodplains, aquatic vegetation, sediments, and infrastructure [36]. Given this dual role, monitoring and mitigation efforts in rivers could substantially reduce MPs inputs to the oceans.

With ongoing urbanization, hydraulic structures such as dams and weirs have been widely introduced into river systems. These structures typically alter flow dynamics by creating zones of reduced velocity, which promote the deposition of suspended particles [34], and offer optimal locations for MPs removal. Field studies have reported higher MPs concentrations upstream of man-made structures compared to downstream reaches [125], [126]. While most research has focused on dams, there is limited evidence on

the MPs retention efficiency of other river infrastructure, such as weirs or dikes. Recent findings indicate that sluice gates and weirs in flume experiments can increase non-buoyant MPs retention by > 70% [127]. Similarly, numerical simulations have shown that MPs accumulate in stagnant zones behind weirs, where they can remain for prolonged durations [128].

Groynes, also known as spur dikes, are a series of structures built transverse to the river flow [129]. Historically, they were constructed to reduce flood risk and to maintain sufficient water depths for navigation, such as the River Elbe in Central Europe and Lake Windermere in Canada [130], [131]. At present, groynes are used to deflect flow away from erodible banks and to control flow in the bends of meandering rivers [16], [17]. In addition, groynes have also been used to enhance river habitats by promoting emergent vegetation growth within the groyne field, which supports aquatic life and contributes to water purification [18]. There are different shapes of groynes, including I-head, T-head, L-head, and hockey stick-shaped forms (Fig. 4) [16]. They are also classified based on their inclination, with attracting spurs angled downstream (45° – 60°) and repelling spurs angled upstream (60° – 80°) [132]. These variations influence flow contraction, turbulence, and sediment deposition [133].

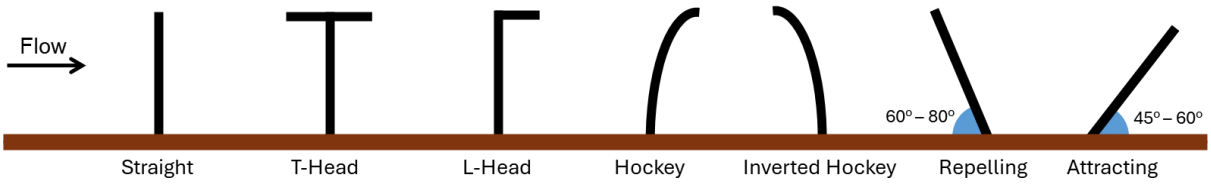

Figure 4 Plan view of common groyne shapes.

Building on the sediment-trapping capacity of groynes, recent studies have investigated their effectiveness at trapping floating macroplastics (size > 5 mm). Przyborowski et al. (2024) found that extending the length of a groyne narrowed the main channel, which intensifying lateral mixing and diverted more buoyant

macroplastics into the downstream recirculation zone. These results suggested groyne fields can act as strategic interception zones for riverine plastic debris management.

This effect is driven by the recirculation and mixing layers generated by groynes, which divide the channel into the mainstream and the groyne fields. Within the groyne fields, backflow develops, resulting in velocities typically only 25 – 30% of those in the main stream [18]. These zones are therefore often referred to as stagnant water areas or dead zones [17], [18]. The velocity difference between the mainstream and groyne fields generates mixing interfaces, where mass and momentum exchange occur through a turbulent mixing layer [21]. These exchange processes are generally governed by two-dimensional large-scale circulation, with coherent vortices in the mixing layer playing a key role [21], [134]. In particular, high shear forces generated by these vortices influence the formation of sand waves further downstream [135]. Particle Image Velocimetry (PIV) data showed that the mixing layer initiates at the upstream groyne, where vortices are shed, and that the flow within the dead zone can contain multiple gyres [134].

This study aims to look into how effectively groynes trap non-buoyant MPs, utilizing the well-established role of groynes in creating low-velocity recirculation zones where sediments settle and are retained. Because the transport of non-buoyant MPs resembles that of sediments, we hypothesize that groynes will similarly retain MPs. Specifically, this study will (1) measure overall MPs trapping efficiency under controlled hydraulic conditions, (2) compare the effectiveness of alternative groyne geometries to determine shapes that maximize retention, and (3) evaluate how particle density influences capture and retention. Outcomes provide insights into designing or retrofitting groynes to increase MPs trapping and shedding light on MP mitigation strategies in regulated rivers.

This paper is structured as follows: following the introduction, Section 2 outlines the theoretical considerations underlying MPs settling and transport. Section 3 describes the experimental setup, including

flume conditions, groyne configurations, and particle tracking methodology. Section 4 presents the results of the trapping efficiency tests across different groyne configurations and particle densities. Section 5 discusses the implications of these findings in relation to existing literature and river engineering practices. Finally, Section 6 concludes with key insights and potential applications for enhancing MPs retention in regulated rivers.

3.2 Theoretical Considerations

The terminal settling velocity (w_s) is the constant velocity a particle sinks in a fluid when the gravitational force is balanced by the drag force, assuming no additional vertical forces act upon it. The w_s of a spherical particle shape is given by the Stokes' formula:

$$w_s^2 = \frac{4}{3}\frac{dg}{C_d}\left(\frac{\rho_s - \rho}{\rho}\right) \quad (1)$$

in which g is the gravitational acceleration; d is the particle diameter, replaced by equivalent spherical diameter (d_{eq}) for non-spherical particles; C_d is the drag coefficient; ρ is the density of fluid; and ρ_s is the density of particle. The drag force quantifies the resistance a particle experiences during settling and is often the most difficult parameter to determine, as it depends on multiple variables including the particle Reynolds number (i.e., $Re = w_s d/\nu$, where ν is the kinematic viscosity of the fluid), shape, and orientation.

Since MPs differ markedly from natural sediments in these physical properties, numerous studies have examined their settling behavior by modifying or recalibrating C_d to account for such differences. The semi-empirical drag model proposed by Bagheri and Bonadonna (2016) was adopted in this study (detailed in SI §1). The model was selected based on findings from review studies on existing models [60], [61].

3.3 Experimental Setup

3.3.1 Flume

The experiments were conducted in the Hydraulics Laboratory at the University of Ottawa using a recirculating rectangular flume 5 m long, 0.62 m wide and 0.3 m deep, with a smooth bed and filled with tap water at 25°C (Fig. 5).

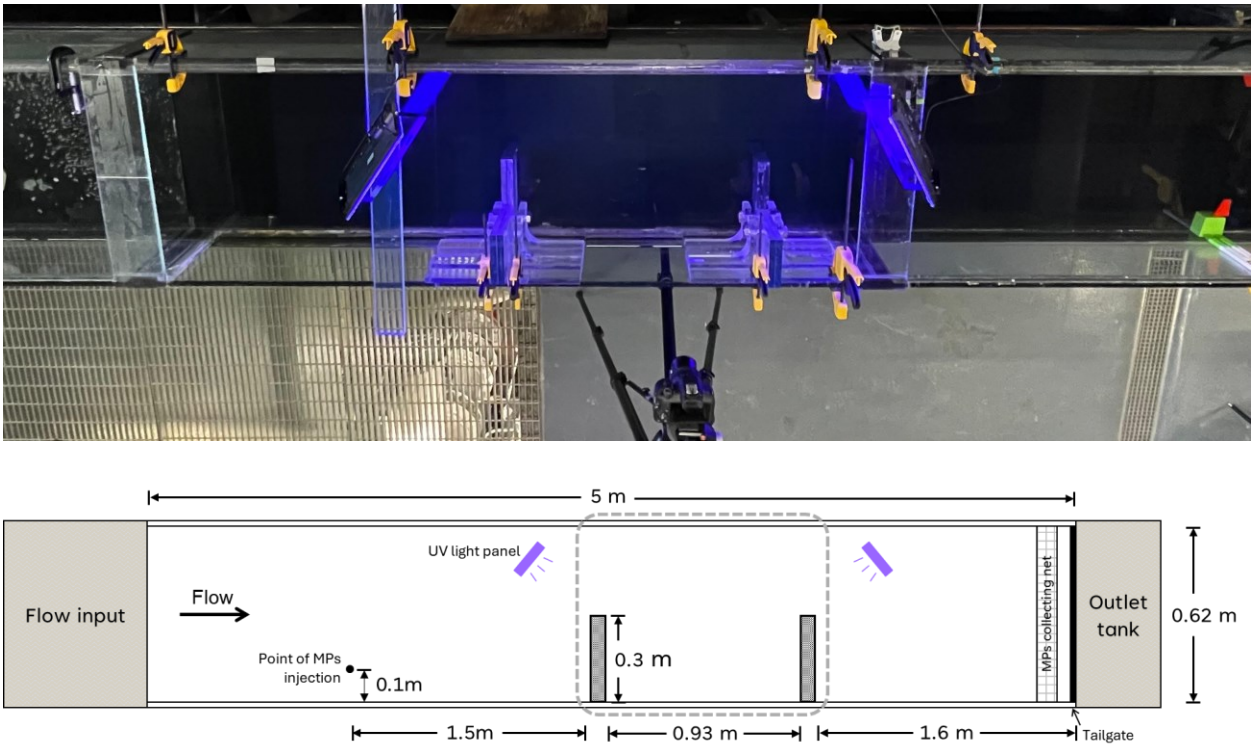

Figure 5 (Top) Plan view photo *of experimental flume with two groynes mounted on one and two LED UV-A panels placed above the flume. The camera in the image was positioned away from the flume to provide a clear view of the region of interest. During runs, the camera is adjusted to 40 cm above the flume with the lens perpendicular to the flume. (Bottom) Plan view schematic of the experimental flume (not to scale). The black dot marks the particle injection point, and the gray dashed line outlines the region of interest (ROI) used for particle tracking.*

A perforated plate at the inlet ensured flow straightening, while a tailgate at the outlet controlled water depth. Subcritical turbulent flow conditions were established by adjusting the inlet valve and tailgate, with

the flow rate determined by slowly increasing until > 95% of originally static MPs particles (ρ_s = 1.11 g/cm^3) were mobilized. Flow velocity was measured with an electromagnetic flowmeter (*Fluvia RC3*, Aqua Data Ltd.), and hydraulic smoothness was confirmed via the shear Reynolds number criterion. Velocity profiles were then fitted to the law of the wall to estimate shear velocity (u_*), a fundamental descriptor of boundary shear conditions in the flume [137].

In the final setup, the flow conditions were characterized by a mean flow of 14.4 cm/s, flow depth (h) of 12.5 cm, Froude number of 0.130, a Reynolds number of 1.80×10^4, and u_* of 0.00632 m/s.

3.3.2 Groynes

Parameters such as angle, material, shape, spacing, and height have been varied in the construction of groynes for river training [138]. Among these, spacing, typically expressed as the ratio of groyne spacing (S) to groyne length (L), or S/L ratio, is a key factor [16]. In this study, the S/L ratio was chosen based on preliminary tests that took into account both the MPs entrainment rate and commonly used engineering configurations with S/L ratio between 2 and 6 [16]. A S/L ratio of 3.1 was adopted for all tests, comparable to that reported for the River Waal [20]. The spacing was kept constant to enable direct comparison of tip effects.

Two acrylic plates 3.5 cm thick, 30 cm long (L) and 40 cm tall were used to resemble impermeable groynes, with length constricted to 50% of the channel width (Fig. 5). Ten configurations were tested by combining four shapes, including common groyne shapes, namely I-shape (referred to as straight groyne hereafter), repelling (70^o inclined upstream), inverted hockey-stick shape (referred to as hockey-stick shape hereafter) and T-shape (geometries detailed in Table S1). These included cases where both groynes shared the same shape, as well as mixed cases in which at least one groyne was straight. For each case, groyne pairs were

installed on the right flume wall, 2.4 m downstream from the inlet, and different groyne tip shapes were achieved by attaching 3D-printed parts to the acrylic plates.

3.3.3 Microplastics Particles

Microplastic pallets were produced using a 3D printer (*FLsun v400*) with a printing precision of ± 0.1 mm. Fluorescent yellow printing material (*AMZ3D*) was selected to facilitate particle tracking during the experiments. The particles were produced as circular cylinders with a diameter and height of 2 mm with rounded sides (Fig. S1a). The spherical equivalent diameter (d_{eq}) was calculated by the equation $d_{eq} = \sqrt[3]{3abc/2}$, where a, b, and c are the lengths of the long, intermediate, and short sides, respectively. Density was determined by weighing the particles on an electronic balance (precision 0.01 g) and measuring their volume in a 50 mL volumetric cylinder after air bubble removal. Final values represent the mean of 10 repeated measurements. By adjusting the air content during printing, two target densities (1.08 and 1.11 g/cm³) were achieved. These values were chosen to reflect environmentally relevant conditions as polyethylene (PE; ρ_s = 0.88–0.96 g/cm^3) has been reported as the most common polymer in river sediments [34]. Particle density was set slightly higher (i.e., 1.08 and 1.11 g/cm³ compared to ρ_s of PE) to account for biofouling (i.e., the accumulation of organic matter on MP surfaces) in aquatic environments and practical constraints associated with 3D printing. Recent studies have shown that biofouling can substantially increase density of buoyant MP pellets and lead to persistent negative buoyancy, even during colder winter months [59], [94].

Given the particle settling velocity (w_s) and shear velocity (u_*), particle transport can traditionally be characterized by the Rouse number (P). However, as subsequent studies showed that P is not fully applicable to near-bed MP motion [47], this study employed the phase diagram of Al-Zawaidah et al. (2024), which predicts transport mode based on the transport stage (u_*/w_s) rather than P. According to the

phase diagram of Al-Zawaidah et al. (2024), the transport of the MPs used in this study was dominated by suspension (approximately 50 – 65% of time).

Table 6 Properties of the MP particles used in the experiments, including their density (ρ_s), spherical equivalent diameter (d_{eq}) settling velocity (w_s), drag coefficient (C_d), particle Reynolds number (Re_p) and transport stage (u_*/w_s).

Type	ρ_s **(g/cm^3)**	d_{eq} **(mm)**	w_s **(mm/s)**	C_d	Re_p	u_*/w_s
PLA	1.08	2.29	0.235	43.26	0.604	2.69
PLA	1.11	2.29	0.323	32.04	0.829	1.96

3.3.4 Particle Tracking

A particle tracking technique was employed to track the bulk movement of the MPs (i.e., retention zone) within the groyne fields. Videos were taken using a *Canon EOS R100* mirrorless camera equipped with an 18 – 45 mm IS STM lens, recording at 1920 × 1080 pixels and 60 fps. The camera was positioned 40 cm from the flume center between the two groynes (Fig. 5), while illumination was provided by two 150 W LED UV-A panels placed perpendicular to the camera and directed towards the flume (Fig. 5). All experiments were conducted in darkness to reduce reflections, with the flume bed and walls covered in black adhesive sheets to maximize particle–background contrast.

The videos taken after each run were processed by a self-developed particle tracking model (PTM) which employed the open-source Python library *Trackpy* [139]. Prior to the analysis, each frame was cropped and filtered by applying thresholds on hue, saturation, and value of each frame to create a binary mask to suppress noise and remove falsely detected flume structures. The processed frames were then supplied to *Trackpy*, where particles were identified and linked across consecutive frames (detailed in SI §3).

A key challenge of the PTM lies in reliably identifying particle displacements, particularly in the turbulent region around the groyne where the wavy water surface causes frequent refractions. This often led to temporary misdetections, with particles appearing either as duplicates or false disappearance. Since all particles should only enter the region of interest from the inlet side, any new appearance of MPs in the groyne field was attributed to refraction, meaning these cases were in fact false splits of a single particle trajectory. To address this, trajectory fragments were merged through an iterative linking procedure: false splits, defined as particles that either first appeared and/or disappeared within the groyne field, were first detected. False duplicates, which are coexisting trajectories that either started or ended within a short frame window and distance threshold were then linked (Fig. S4a). After this, the remaining false splits were resolved by linking trajectory endpoints to nearby trajectory start points across frames using short-range distance (Fig. S4b) or particle velocity prediction (Fig. S4c). Multiple co-occurrence checks and repeated iterations over expanding search radii ensured reconstruction of continuous particle trajectories (Fig. 6).

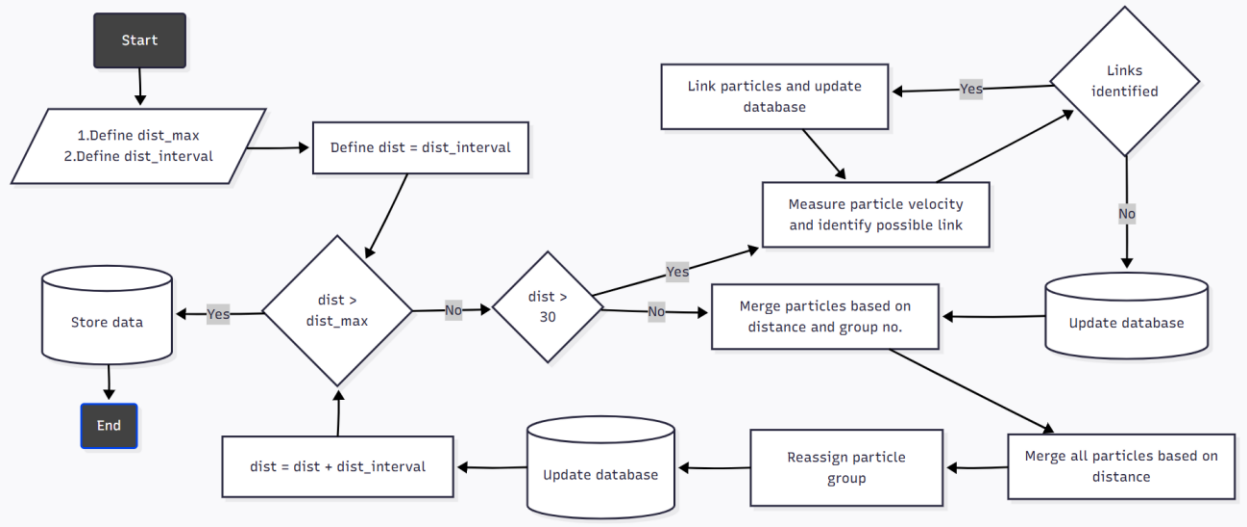

Figure 6 Flow chart for optimizing particle trajectories. Variables dist_max and dist_interval were defined as the maximum search radius and the search radius interval. By increasing the search radius by the defined interval on every iteration, the program will check if current radius > 30 pixels. This search radius threshold, determined through trial and error to balance computational effort and accuracy, triggers

trajectory linking with particle velocity prediction, which was more accurate for larger search radii than distance-based search but requires more computational effort. Each particle was assigned a group number to facilitate linking (more detailed in SI §3).

3.3.5 Procedures

At the start of each experiment, the flow was run for 15 min to ensure full development and quasi-uniform flow conditions. Water depth and temperature were measured. Microplastic particles were then injected at the bed, 10 cm from the right wall and 1.5 m upstream of the first groyne. A fluid extractor originally designed for automotive use was modified for particle injection and connected to a long injection pipe to minimize flow interference. Injection was performed at a rate of 100 particles per 10 s, for a total of 1000 particles, with injection speed kept minimal to avoid accelerating the particles. After injection, the flow continued for 5 minutes, a duration determined from preliminary tests, which showed that the fraction of MPs leaving the groyne field of all 10 configurations did not differ substantially between test periods of 5 to 10 minutes. At the end of the test, MPs in the groyne field were collected and counted manually. Each scenario was repeated 20 times and videos were recorded for the region of interest.

3.4 Results

A total of 20 experimental scenarios were tested, each repeated 20 times (n = 20, except in one scenario where an outlier was removed), to evaluate the influence of groyne configuration and particle density on MPs trapping dynamics (Fig. 7). Scenarios were coded by groyne shape and particle density, separated by a hyphen. The groyne shapes were denoted as S (straight), R (repelling), T (T-shaped), and H (hockey stick-shaped), ordered according to their sequence facing the inlet. Particle density was indicated as D (dense) or L (light). For example, for the scenario where the upstream groyne was straight and downstream groyne was T-shaped, with dense MPs used, it is coded as “ST-D". Each scenario and their corresponding code were illustrated in Table S2.

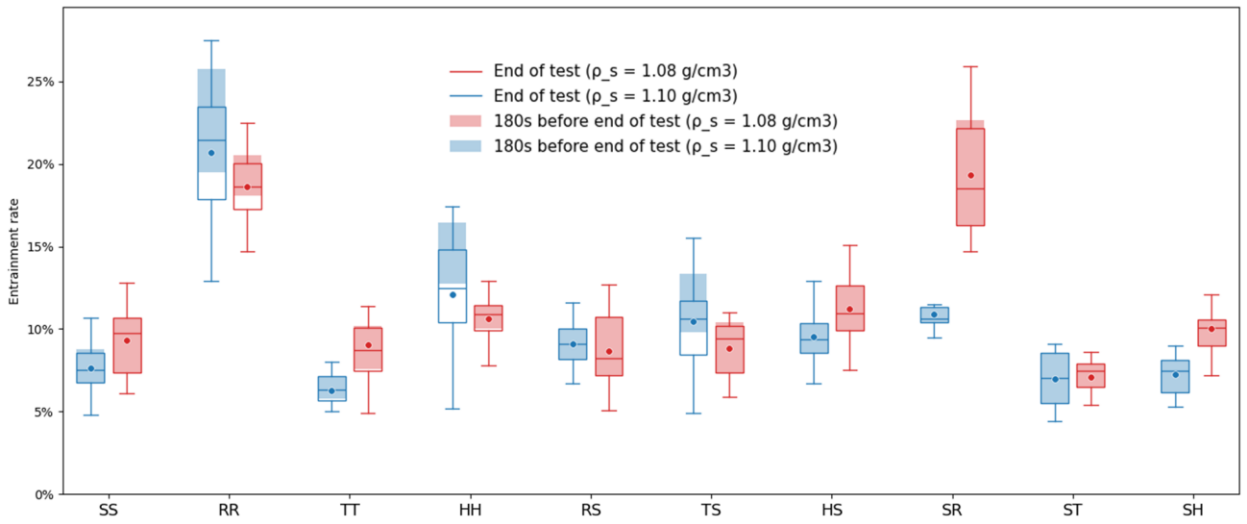

Figure 7 Microplastic entrainment rates across different groyne configurations for two MPs densities (ρ_s = 1.10 g/cm^3 and ρ_s = 1.08 g/cm^3) are plotted. Boxplots show the interquartile range (IQR; 25th–75th percentile) for 180s before end of test and at test completion in shaded and outlined boxes, respectively. Whiskers, median lines, and mean markers are shown only for the end-of-test measurements. Repelling groynes (RR) produced the highest entrainment ($p < 0.05$), while escape rates of most cases were negligible. Only scenario SR, SH and TT showed significant entrainment rate ($p < 0.001$) differences between denser and lighter particles.

Trapping efficiency of groyne configurations was assessed through particle entrainment and escape rates. The entrainment rate was calculated as the ratio of particles counted at the end of each run to the number of MPs injected. The escape rate was the ratio of particles leaving the groyne field within the last 180 s of each test to the maximum number of particles in the field during the same period. Particle counts were obtained by manual counting and independently verified using a trained automated counting program.

Due to the small sample size and violations of normality in some cases (SI §4), non-parametric tests were applied. Entrainment rates of each scenario were analyzed using the Kruskal–Wallis test (i.e., non-parametric alternative to one-way ANOVA) to evaluate overall differences among groups. When

significance was observed (i.e., $p < 0.05$, where p represents the probability that the observed result could occur just by chance alone), pairwise comparisons were conducted using the Dwass–Steel–Critchlow–Fligner (DSCF) test (i.e., post-hoc test following Kruskal–Wallis test). Corresponding effect sizes were reported to quantify the magnitude of effects, reported as epsilon-squared (ε^2) for overall differences and absolute Cliff's delta ($|\delta|$) for pairwise comparisons.

The influence of specific configurations on entrainment counts, retention location, and effects of particle densities will be examined in greater detail in the following sections.

3.4.1 Code Validation

The PTM code used for identifying retention zones within groyne fields were primarily validated through visual comparison of observed and tracked particle behavior. The observed and plotted retention zones showed good agreement, indicating that the main transport patterns were well captured. The code was further evaluated by comparing manually counted entrainment numbers with program outputs across 80 experimental results covering different scenarios. On average, the code underestimated the final number of particles in the groyne field by 26.1%, which was expected given its limited ability to resolve overlapping or clustered particles. Nonetheless, this error was considered negligible since the PTM code focused on bulk MPs movements rather than individual particle trajectories.

3.4.2 Entrainment Number

Across all scenarios, groynes were able to trap a minimum of ~6% of particles within the 5-minute test period. The repelling groynes consistently produced the highest mean entrainment rates (μ) for both tested particle densities, peaking at approximately 20% of entrainment for scenarios RR-D, while other configurations generally showed lower trapping efficiency. Escape rates were consistently low (< 3%) with light particles, while denser particles produced mixed results with about half near zero but some exceeding

7%, particularly when both groynes had the same shape (Table S3). The variability of entrainment performance was substantial, with coefficients of variation (CV) ranging from 10.9% to 29.6%, highlighting the inherent variability in particle–groyne interactions, even under controlled conditions.

Scenarios with both groynes having the same geometries (i.e., SS, RR, TT and HH) showed the largest and most significant differences in entrainment rate ($p \ll 0.001$; $\varepsilon^2_{dense} = 0.72$, $\varepsilon^2_{light} = 0.61$). For both MPs densities, RR yielding the highest entrainment ($\mu_{RR\text{-}D} = 20.7 \pm 3.7\%$; $\mu_{RR\text{-}L} = 18.6 \pm 2.0\%$), followed by HH ($\mu_{HH\text{-}D} = 12.1 \pm 3.6\%$; $\mu_{HH\text{-}L} = 10.6 \pm 1.2\%$), while SS ($\mu_{SS\text{-}D} = 7.6 \pm 1.7\%$; $\mu_{SS\text{-}L} = 9.3 \pm 2.1\%$) and TT ($\mu_{TT\text{-}D} = 6.3 \pm 1.2\%$; $\mu_{TT\text{-}L} = 9.0 \pm 2.3\%$) consistently showed the lowest entrainment. Statistical pairwise comparisons also proved that the difference in trapping efficiencies of repelling groynes (RR) for both MPs densities was highly significant compared to other shapes ($p \ll 0.001$, $|\delta| \geq 0.91$). By contrast, the difference between straight and T-shaped groynes for either density was insignificant, while comparisons involving hockey stick-shaped groynes were marginally significant or nonsignificant depending on density (Table S4). Overall, when both groynes share the same shape, strong sensitivity of trapping efficiency to groyne geometry was observed among all groups, with repelling groynes consistently achieving the highest entrainment, while SS and TT were the weakest. Notably, SS and TT had minimal MPs escape (< 3%), whereas HH-D exhibited the highest escape (15.1%) and RR-D also showed elevated loss (7.2%).

For scenarios with an upstream straight groyne followed by another shape (i.e., SR, ST, SH and SS), similarly large but more selective contrasts were observed. Differences in entrainment rate were highly significant ($p \ll 0.001$; $\varepsilon^2_{dense} = 0.45$, $\varepsilon^2_{light} = 0.69$), with SR consistently trapping more MPs than other configurations ($p \ll 0.001$, $|\delta| \geq 0.85$). Across densities, SR was the most effective combination ($\mu_{SR\text{-}D} = 10.9 \pm 1.7\%$; $\mu_{SR\text{-}L} = 19.4 \pm 3.7\%$), exceeding that of SS, ST ($\mu_{ST\text{-}D} = 7.0 \pm 1.7\%$; $\mu_{ST\text{-}L} = 7.1 \pm 1.6\%$) and SH ($\mu_{SH\text{-}D} = 7.2 \pm 1.5\%$; $\mu_{SH\text{-}L} = 10.0 \pm 1.6\%$). Relative to the straight-only scenario (SS), downstream substitution with T- or hockey-stick shaped groynes produced insignificant changes for all tests using dense particle, while significant difference were observed when ST-L was compared to SS-L ($p < 0.05$) and ST-

L ($p < 0.01$). Escape rates were negligible (< 1% in most cases), with SR showing slightly higher values (0.9 ± 1.6% for dense MPs, 1.6 ± 2.0% otherwise). Overall, when a straight groyne was placed upstream, combining it with a repelling groyne downstream markedly improved trapping efficiency, while ST and SH offered little or no advantage over straight pairs.

Lastly, for scenarios with a downstream straight groyne preceded by another shape (i.e., RS, TS, HS and SS), significant differences were shown but they were comparatively smaller than the cases described above ($p \approx 0.001 - 0.002$; $\varepsilon^2 \approx 0.15 - 0.17$). Post-hoc tests indicated that most pairwise contrasts were nonsignificant, with only HS outperforming TS ($p = 0.0239$) and RS ($p = 0.0420$), while downstream T-shaped groynes slightly exceeded straight groyne-only pairs ($p = 0.0461$). For completeness, the entrainment rates of HS ($\mu_{HS\text{-}D}$ = 9.6 ± 1.7%; $\mu_{HS\text{-}L}$ = 11.2 ± 1.9%), TS ($\mu_{TS\text{-}D}$ = 10.4 ± 3.1%; $\mu_{TS\text{-}L}$ = 8.6 ± 1.6%) and that of RS ($\mu_{RS\text{-}D}$ = 9.1 ± 1.4%; $\mu_{RS\text{-}L}$ = 8.7 ± 2.3%) was reported. Escape rates were generally low (< 2%), though TS-D showed a noticeable 9.3%. Overall, while HS provided a slight advantage, low sensitivity of trapping performance towards groyne geometries was observed when the straight groyne was positioned downstream.

Apart from the straight groyne arrangement-based comparison, pairwise comparisons within the same shape family (i.e., RR/RS/SR, TT/TS/ST, HH/HS/SH) were also conducted. For repelling groynes, the RR-D configuration showed significantly greater entrainment than the other two dense-particle cases ($p \ll 0.01$), whereas differences between RR-L and SR-L were not significant. Hockey stick-shaped groynes were highly sensitive to particle density where denser MPs exhibited significant shape dependence in entrainment with HH being the highest and SH the lowest ($p < 0.05$), while lighter MPs showed none of such variations. In T-shaped groynes, significant contrasts were detected only between TT-D and TS-D ($p < 0.01$), with other scenarios yielding marginal or non-significant differences.

3.4.3 Microplastics in Groyne Field

In all scenarios, MPs entered the groyne field from the downstream end (Fig. S6), forming a gyre in clockwise direction with flow directed from left to right, consistent with observations in other studies [134], [140]. After entry, particles typically formed a cluster near the center of the field, slightly biased toward the downstream groyne. Spatial distributions over the final 150s were averaged and visualized for each scenario. As both particle densities showed comparable distributions, the focus is placed on dense particles, with light-particle results included in supplementary information (Fig. S7).

While most configurations produced a single retention zone, the size of this area varied across groyne arrangements. Configurations with inclined groynes (second column from the left of Fig. 8 and S7) consistently exhibited broader retention zones than all others. In particular, RR and SR showed upstream extensions, with SR-D displaying a tendency to split into two distinct zones. This effect was even more pronounced for light particles, where MPs clustered near the upstream groyne, a pattern distinct from other cases. Although RS-D and TS-D exhibited similar color intensity in their trapping zones, RS-D had a markedly lower escape rate despite its more horizontally spread distribution, indicating a steadier retention zone. For RS-L and TS-L, escape rates were similar.

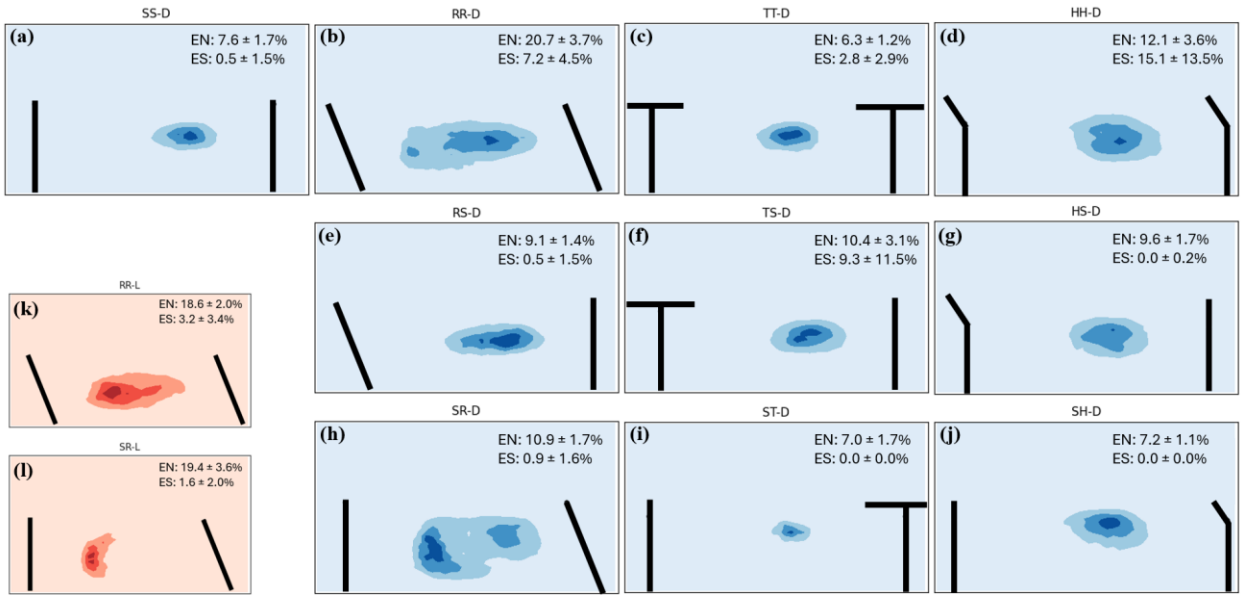

Figure 8 Spatial distribution of MPs particles in groyne fields during the final 150 s of the experiment. Flow directed from left to right. Panels (a) – (j) show dense particles, while panels (k) – (l) show light particles. Shading represents particle concentration, with mean entrainment (EN) and escape (ES) rates indicated for each configuration. Most setups generated a single retention zone, though its extent and intensity varied with groyne geometry and particle density.

Apart from the TS-D case, downstream T-shaped groynes generally produced a more centralized cluster, with retention zones that were small in size but high in intensity. This was evident when comparing ST-D with SH-D, where both configurations showed comparable entrainment and escape rates, yet the retention zone of ST-D was only about a quarter of the size of SH-D (Fig. 8i, 8j). The same pattern was also observed in the light-particle cases.

Configurations with upstream hockey stick-shaped groynes produced the most diffused retention zones among all scenarios when dense particles were used, with HH-D showing broad spatial spread but high escape. In contrast, the corresponding light-particle cases exhibited compact retention zones with markedly lower escape rates.

3.4.4 Effect of Microplastics Density

Pairwise DSCF tests (i.e., a post-hoc multiple comparison procedure following Kruskal–Wallis) indicated that light particles had significantly higher entrainment than dense particles in SR ($p << 0.001$, $|\delta| = 1$), SH ($p << 0.001$, $|\delta| = 0.86$), and TT ($p < 0.001$, $|\delta| = 0.76$). For the remaining configurations, differences between dense and light particles were not statistically significant (Table S5).

Beyond entrainment, lighter particles also exhibited either lower (e.g., RR, HH, TS) or more compact retention zones compared to dense particles (Fig. 8). As previously noted, MPs trapping patterns of different groyne shapes were influenced by particle density to some extent. Configurations with hockey stick-shaped

groynes were the most sensitive, showing marked density-dependent differences in both entrainment number and retention area, while repelling groynes also displayed sensitivity through shifts in retention zone structure.

3.5 Discussion

3.5.1 Microplastics Entrainment

Entrainment was consistently observed across all configurations during the five-minute experimental duration, confirming that groynes were effective in trapping non-buoyant MPs. This finding aligned with flow patterns reported in sediment studies, where deposition between groynes was attributed to momentum exchange at the mixing interfaces formed between the main channel and the groyne field [134].

This study demonstrated that configurations with repelling groynes trapped more particles than other shapes, consistent with their established role in enhancing bank protection and promoting sedimentation by minimizing bank erosion compared to alternative designs [129], [141]. The retention zones associated with repelling groynes were also consistently larger than those of other configurations, a result in line with previous observations that stronger vortices are generated by repelling groynes compared to straight ones [142]. While upstream-inclined groynes enhanced mixing and thereby increasing particle entrainment, it could also reduce residence times [134], as reflected in the high escape rate observed in the RR-D scenario.

For configurations with double T-shaped groynes, the experimental results were consistent with previous findings that particle retention was promoted by still-water zones created by wide-headed groynes [133]. This effect persisted when the upstream groyne was replaced by a straight groyne, but disappeared when the downstream groyne was substituted, indicating that the downstream T-shaped groyne was critical for stable particle retention. Notably, the ST configuration exhibited the smallest retention zone among all configurations for both particle densities, potentially offering an optimal spot for targeted MPs collection.

In fact, across all scenarios with dense particles, upstream straight perpendicular groynes consistently produced the lowest escape rates. This outcome may be explained by the stronger flow obstruction generated by straight groynes compared to T-shaped ones, which created more pronounced eddies and turbulence behind the groyne head and thereby facilitating particle retention [143].

As earlier studies have shown, eddies shed from the upstream groyne form large coherent structures within the mixing layer, which strongly influence mixing and subsequent particle deposition in the groyne field [20]. Based on this, particle trapping rates were expected to be primarily dependent on the shape of the upstream groyne. However, the experimental results revealed the opposite: trapping rates were more strongly governed by the shape of the downstream groyne. This was likely caused by the fact that particles predominantly entered the groyne field near the downstream end, their retention being directly influenced by the downstream groyne.

3.5.2 Effect of Microplastics Density

The difference in particle density resulted in distinct transport modes. Suspended load deposition is expected to follow gyre structures within the groyne field, as suggested by Sukhodolov et al. (2002), whereas bedload moving as sand waves is more closely governed by the distribution of critical bed shear stress [21], [140]. This mechanism may explain why distinct retention zone patterns across particle densities were particularly evident under conditions of larger vortices and stronger mixing, as in configurations with repelling groynes. As a result, lighter particles, following the gyre structure, were observed to settle in the relatively static upstream end of the groyne field.

Previous studies further showed that vortices and turbulent structures vary across water depths within groyne fields [142]. In particular, turbulence at intermediate depths was reported to be lower than that at the surface or near the channel bed [142], which may explain the consistently low escape rate of less dense

particles that were likely transported predominantly at intermediate depths. Given the wide range of MPs densities, the distribution of trapped particles within groyne fields can therefore be expected to remain highly heterogeneous across water depth.

3.5.3 Scale Effect

To ensure meaningful comparisons between experimental results and prototype observations, scale effects must be addressed. Among the various modelling similitudes, dynamic similarity is critical for maintaining consistent force ratios, yet it is impossible to replicate identical ratios for all forces in both model and prototype [145], [146]. Consequently, open-channel flow research has traditionally adopted Froude scaling to balance inertial and gravitational forces for physical models [146], [147]. In line with this approach, our study selected a low Froude number to mirror field observations of rivers [148], while maintaining a high Reynolds number to preserve turbulent flow conditions.

Given the complex nature of particle transport, where particle size, friction forces, and settling velocity can all disrupt similitude between model and prototype, the scaling approach adopted for sediments was usually different from the rest of the physical model [149]. The similitude used for sediments is based on the Shields diagram where it was assumed that the prototype and model shared the same point on the Shields diagram [146]. By equating the similitude ratios of the Shields number and Re_p, the following relationship was established as $d_r = \alpha_r^{-1/3}$, in which d is the particle size, α is the submerged specific gravity; and the subscript r denotes the prototype-model ratio [146]. This implies that if the MPs in the model are e.g. two times larger than those in the prototype, their density must be reduced to $2^{-1/3}$ times that of the prototype to preserve mobility similarity. In the present study, both ratios were taken as unity, thereby satisfying particle similitude.

Nevertheless, this idealized relationship may not fully represent MPs mobility, as previous studies have shown that static friction and hiding–exposure effects can cause substantial deviations in incipient motion compared with natural sediments [45], [102]. In the present study, however, such effects are expected to be limited because the experiments were conducted over a smooth bed, minimizing additional resistance forces.

3.5.4 Recommendations for Future Studies

The present study was conducted in an optimized and controlled flume environment, which excluded several sources of variability typically observed in natural settings, particularly the involvement of sediments. Specifically, the use of a smooth and fixed bed did not account for the bedform variations resulting from sediment reallocation caused by groynes. Prior research has demonstrated that the movement of sediments in groyne fields can be substantial due to localized flow conditions [21], and that experiments with mobile versus fixed beds produce markedly different velocity gradients across groyne fields and the main channel [18]. Beyond sediments, vegetation is another important factor that was not considered in this study, despite its frequent occurrence in groyne fields where low flow velocities and high nutrient retention promote growth; vegetation has been shown to significantly alter velocity distributions [18]. These omissions are especially relevant in the context of microplastic transport, as both sediments and vegetation have been found to strongly influence vertical and streamwise transport dynamics [87], [99], [107].

In addition to possible improvements regarding sediments and vegetation, the current study only examined a single groyne, whereas in reality groynes typically occur in series. Prior research has demonstrated that the first groyne often behaves differently from subsequent ones, as it is strongly affected by upstream flow traction [21]. Similarly, while morphological patterns within groyne fields tend to be consistent, the first groyne frequently deviates from this pattern [21]. Furthermore, studies have reported that scour and deposition patterns are generally comparable across groynes, with notable exceptions occurring near the

first and last structures in the flume [20]. These findings suggest that testing multiple groynes, rather than a single structure, would provide a more realistic representation of groyne field dynamics.

3.6 Conclusion

In this study, the effectiveness of a single pair of groynes in trapping non-buoyant MPs under subcritical turbulent flow was investigated. A total of ten configurations, derived from combinations of four groyne shapes (straight, repelling, T-shaped, and hockey stick-shaped), were tested. To study the role of MPs density, pellets (d_{eq} = 2.29 mm) with two densities (ρ_s = 1.08 and 1.11 g/cm^3) were tested. Across all scenarios, microplastic entrainment, escape rates, and retention zones were compared, from which the following conclusions can be drawn.

1) For configurations with identical shapes, entrainment rate was strongly influenced by groyne geometry, with repelling groynes demonstrating the highest entrainment rate (18.6 – 20.7%), followed by hockey stick-shaped groynes (10.6 – 12.1%), while straight (I-shaped) and T-shaped groynes had the lowest entrainment rates (6–9%). In cases where the upstream groyne was straight and the downstream geometry was varied, configurations with a downstream repelling groyne consistently trapped more MPs than other combinations ($p \ll 0.001$, $|\delta| \geq 0.85$), whereas other arrangements showed no distinct differences. By contrast, trapping performance was largely insensitive to groyne geometry when the upstream groyne geometry was varied with the straight groyne positioned downstream.
2) For configurations with identical shapes, straight and T-shaped groynes enabled minimal MPs escape (< 3%), repelling groynes showed moderate escape rates (3.2 – 7.2%), and hockey stick-shaped groynes exhibited the highest escape of denser particles (15.1%). Notably, configurations combining straight upstream groynes with varying downstream groynes effectively reduced escape rates, particularly for denser MPs.

3) After entering from the downstream end, MPs typically clustered near the groyne field center, tending toward the downstream groyne. Downstream T-shaped groynes generally produced more centralized clusters with small but intense retention zones, suggesting an optimal location for MP collection. With the exception of cases involving repelling groynes, retention zones tended to extend upstream.
4) The effect of MPs density on entrainment rate was not evident in most configurations, likely due to the relatively small density differences among the tested particles. However, lighter particles consistently exhibited significantly lower escape and smaller retention zones, indicating that particles of different densities respond sensitively to the vertical flow dynamics within the groyne field.

Chapter 4 Conclusion and Limitations of the Study

This study aimed to address a knowledge gap regarding how river groynes affect the retention of non-buoyant MPs. Although rivers are increasingly recognized as both transport pathways and temporary reservoirs of MPs, most attention has focused on field observations of hydraulic structures such as dams and weirs. In contrast, groynes, mainly used in river engineering to control flow, manage sediment, and enhance habitats, have rarely been examined for their capacity to entrain MPs despite their sediment trapping design. By investigating a range of groyne geometries under controlled flume conditions, this research contributes new insights into how such structures can influence MPs dynamics.

Across all tested scenarios, the paired groynes trapped at least 6% of injected non-buoyant MPs within the 5-minute test period, with escape rates remaining below 3%. The highest entrainment rate, reaching 20%, was observed for paired repelling groynes. These findings suggest that existing river groynes can function as passive, low-cost traps for microplastics. As groynes in natural rivers typically occur in series, it is further expected that their cumulative trapping effect would be enhanced, given that only a single groyne pair was examined in this study.

When both groynes shared the same shape, entrainment was strongly dependent on geometry. Repelling groynes consistently achieved the highest trapping efficiency, with entrainment rates approaching 20%. Hockey stick-shaped groynes followed with intermediate performance, while straight and T-shaped groynes yielded the lowest entrainment (around 6–9%). These differences underline the importance of groyne inclination in shaping local recirculation and mixing, which directly governs particle entry and retention within the groyne field.

Escape dynamics showed contrasting trends across geometries. Straight and T-shaped groynes enabled minimal escape (< 3%), suggesting strong retention once MPs entered the groyne field. Repelling groynes

produced moderate escape (3 – 7%), while hockey stick-shaped groynes exhibited the highest escape of dense particles, exceeding 15% in some scenarios. These outcomes indicate that high entrainment does not necessarily translate to stable retention, and that geometry can simultaneously promote particle entry and loss through enhanced mixing.

When upstream groynes were straight and downstream geometries varied, trapping performance was particularly sensitive to the downstream shape. Configurations with a downstream repelling groyne consistently outperformed all other arrangements, with statistical tests confirming highly significant improvements in entrainment. By contrast, substitutions with downstream T-shaped or hockey stick-shaped groynes showed little or no advantage over straight-only pairs. This pattern reflects the fact that MPs predominantly entered the groyne field from the downstream end, making the downstream groyne critical in determining retention.

The location and intensity of retention zones also varied with groyne geometry. After entering from the downstream end, MPs typically clustered near the field center, biased toward the downstream groyne. T-shaped groynes in the downstream position generated compact, centralized retention zones of high intensity, offering promising conditions for targeted MPs collection. In contrast, configurations with repelling groynes produced broader zones that extended upstream, reflecting stronger mixing but also higher variability in residence times. Hockey stick-shaped groynes yielded the most diffused zones, especially for dense particles, which corresponded with their higher escape rates.

The influence of particle density was generally subtle but detectable in escape and spatial retention patterns. Such response was primarily a consequence of the small density differences (ρ_s = 1.08 and 1.11 g/cm^3) among the tested MPs, which resulted from technical constraints such as the availability of non-PLA fluorescent 3D printing filaments and printer nozzle size. Although entrainment rates were not significantly

affected in most configurations, lighter particles consistently showed lower escape and more compact retention zones compared to dense particles, suggesting that MPs of different densities respond to vertical flow structures within the groyne field, with lighter particles more likely to follow gyre circulation and accumulate in relatively quiescent regions. Although the density range tested was relatively narrow and limited to sinking polymers, even slight differences still produced observable changes in transport and retention. As other studies showed the motion of near-neutrally buoyant polymers is especially sensitive to small density deviations [64], [122], future studies should extend the range of tested microplastic densities and place greater emphasis on particles with densities close to that of water.

The controlled flume experiments provided clear evidence that groyne geometries influence the trapping and retention of non-buoyant MPs. However, several limitations in the experimental design constrain the environmental realism of the findings. These limitations are not unique to this study but are also commonly observed across other empirical MPs transport experiments reviewed in Section 2.

One important limitation is the use of a smooth and immobile bed, which neglected the fundamental influence of groynes on sediment migration. This reduces the extent to which the results represent real-world application of river groynes. Besides, bed roughness and mobile sediments also affect MPs transport, such as the hiding–exposure effects, infiltration, and long-term retention within bedforms. Previous laboratory studies have shown that MPs can accumulate in trapping zones created by sediment heterogeneity or become retained in migrating ripples [82], [105]. These processes cannot be captured in a smooth-bed flume. Incorporating rough or mobile beds in future groyne experiments would therefore improve the representation of MPs–sediment interactions and allow more realistic assessments of groyne-related trapping efficiency.

Another limitation is that the study examined only a single pair of groynes, although groynes typically occur in series. Research has shown that the first groyne behaves differently from subsequent ones due to

upstream flow traction, while overall morphological patterns within groyne fields are generally consistent except at the first structure [21]. Likewise, scour and deposition patterns are similar across groynes but differ near the first and last in a series [20]. Thus, testing multiple groynes would better capture the dynamics of groyne fields.

The choice of MPs also presents limitations that mirror common shortcomings in other laboratory studies. Cylindrical pellets of relatively large size classes were used here, whereas field surveys consistently show that MPs smaller than 0.3 mm and irregular in shape, particularly fibers and fragments, dominate riverine samples [34], [67]. The underrepresentation of small and irregular particles has been a recurring issue across empirical studies, largely due to technical difficulties in visualization and tracking. Yet, evidence indicates that particle size and shape exert strong controls on settling, resuspension, and dispersion [47], [51]. Future work could address this by adopting advanced visualization techniques, such as fluorescent tagging and particle image velocimetry, which now allow the tracking of sub-millimeter MPs and more complex particle geometries without compromising accuracy [63], [83].

Another limitation lies in the use of steady, subcritical flows. While such controlled conditions are essential for isolating mechanisms, they cannot capture the variability of natural rivers, where flow unsteadiness, turbulence bursts, and interactions with vegetation strongly influence MPs fate. As emphasized in other empirical studies, MPs transport is rarely the product of a single driver but emerges from the combined influence of turbulence, sediment suspension, and transformation processes [73], [79]. Multi-stressor designs remain comparatively scarce but are increasingly recognized as necessary for bridging the gap between laboratory evidence and field observations. Future groyne experiments could therefore benefit from introducing unsteady hydrographs or coupling groynes with vegetated and sediment-rich conditions.

Finally, the MPs used in this study were pristine, while natural MPs undergo weathering and biofouling that alter density, drag, and surface properties. Other experimental studies have shown that transformations such as biofilm growth or UV aging can significantly accelerate settling, promote aggregation with suspended matter, or reduce retention when biofilm-coated sediments are present [56], [86], [93]. Incorporating aged or biofouled MPs into experimental designs would therefore provide a more realistic test of whether the observed trapping efficiencies persist once particles have been altered by environmental processes.

In conclusion, this study provides the first experimental evidence that groyne geometry can substantially influence the retention of non-buoyant MPs. By demonstrating that trapping efficiency is strongly dependent on groyne configuration and that retention stability can differ from entrainment potential, the work highlights both the opportunities and challenges of using groynes as part of MPs mitigation strategies. Although conducted under controlled laboratory conditions, the findings establish a foundation for future field-relevant research and suggest that groynes, when strategically designed, could contribute to reducing microplastic transport in river systems.

4.1 Recommendations for Future Studies

Building on the abovementioned limitations, several directions for future research are suggested. First, future experiments should incorporate mobile and rough beds to better capture sediment–flow interactions and their influence on MPs transport, including hiding–exposure effects, infiltration, and long-term retention within bedforms. Second, future experiments should test a wider variety of particle sizes and shapes, particularly fibers, films, and fragments that dominate in rivers, as well as near-neutrally buoyant polymers. Third, future work should adopt experimental designs that capture the combined effects of multiple environmental drivers. For example, experiments conducted under unsteady flow regimes could reveal how transient hydraulics influence retention. Similarly, coupling groyne fields with vegetation would

help clarify how substrate complexity and ecological interactions affect MPs aggregation, burial, and resuspension. Fourth, testing groynes in series, rather than individually, would provide a more realistic representation of groyne field dynamics. Finally, advanced visualization and tracking methods, such as fluorescent tagging, particle image velocimetry, and high-resolution imaging, would allow more accurate characterization of the transport dynamics of sub-millimeter MPs. Together, these approaches would provide a more realistic representation of riverine environments and strengthen the applicability of laboratory findings to field conditions.

References

[1] M. Streit-Bianchi, M. Cimadevila, W. Trettnak, and SpringerLink, *Mare Plasticum - The Plastic Sea Combatting Plastic Pollution Through Science and Art*, 1st ed. 2020. Cham: Springer International Publishing, 2020. doi: 10.1007/978-3-030-38945-1.

[2] A. Thacharodi *et al.*, "Microplastics in the environment: A critical overview on its fate, toxicity, implications, management, and bioremediation strategies," *J. Environ. Manage.*, vol. 349, p. 119433, Jan. 2024, doi: 10.1016/j.jenvman.2023.119433.

[3] U.S. Geological Survey, "Microplastics Sources, Pathways and Fate Conceptual Diagram | U.S. Geological Survey." Accessed: Apr. 06, 2025. [Online]. Available: https://www.usgs.gov/media/images/microplastics-sources-pathways-and-fate-conceptual-diagram

[4] L. Su *et al.*, "Global transportation of plastics and microplastics: A critical review of pathways and influences," *Sci. Total Environ.*, vol. 831, pp. 154884–154884, 2022, doi: 10.1016/j.scitotenv.2022.154884.

[5] X. Wang, Z. Li, B. Sun, F. Wang, Z. Li, and C. Gualtieri, "Impact of Fenton aging on the incipient motion of microplastic particles in open-channel flow," *Sci. Total Environ.*, vol. 953, pp. 176220-, 2024, doi: 10.1016/j.scitotenv.2024.176220.

[6] S. D. Traylor, E. F. Granek, M. Duncan, and S. M. Brander, "From the ocean to our kitchen table: anthropogenic particles in the edible tissue of U.S. West Coast seafood species," *Front. Toxicol.*, vol. 6, pp. 1469995-, 2024, doi: 10.3389/ftox.2024.1469995.

[7] T. Horvatits *et al.*, "Microplastics detected in cirrhotic liver tissue," *EBioMedicine*, vol. 82, p. 104147, Aug. 2022, doi: 10.1016/j.ebiom.2022.104147.

[8] L. C. Jenner, J. M. Rotchell, R. T. Bennett, M. Cowen, V. Tentzeris, and L. R. Sadofsky, "Detection of microplastics in human lung tissue using μFTIR spectroscopy," *Sci. Total Environ.*, vol. 831, p. 154907, Jul. 2022, doi: 10.1016/j.scitotenv.2022.154907.

[9] A. Ragusa *et al.*, "Plasticenta: First evidence of microplastics in human placenta," *Environ. Int.*, vol. 146, p. 106274, Jan. 2021, doi: 10.1016/j.envint.2020.106274.

[10] R. Marfella *et al.*, "Microplastics and Nanoplastics in Atheromas and Cardiovascular Events," *N. Engl. J. Med.*, vol. 390, no. 10, pp. 900–910, 2024, doi: 10.1056/NEJMoa2309822.

[11] M. Strokal, P. Vriend, M. P. Bak, C. Kroeze, J. van Wijnen, and T. van Emmerik, "River export of macro- and microplastics to seas by sources worldwide," *Nat. Commun.*, vol. 14, no. 1, p. 4842, Aug. 2023, doi: 10.1038/s41467-023-40501-9.

[12] F. Xia, Q. Tan, H. Qin, D. Wang, Y. Cai, and J. Zhang, "Sequestration and export of microplastics in urban river sediments," *Environ. Int.*, vol. 181, p. 108265, Nov. 2023, doi: 10.1016/j.envint.2023.108265.

[13] L. Watkins, S. McGrattan, P. J. Sullivan, and M. T. Walter, "The effect of dams on river transport of microplastic pollution," *Sci. Total Environ.*, vol. 664, pp. 834–840, May 2019, doi: 10.1016/j.scitotenv.2019.02.028.

[14] E. A. Wicaksono, S. Werorilangi, and A. Tahir, "The influence of weirs on microplastic fate in the riverine environment (case study: Jeneberang River, Makassar City, Indonesia)," *IOP Conf. Ser. Earth Environ. Sci.*, vol. 763, p. 012054, May 2021, doi: 10.1088/1755-1315/763/1/012054.

[15] E. C. for A. and the F. E. United Nations, *River Training and Bank Protection*. United Nations., 1953.

[16] B. Przedwojski, K. W. Pilarczyk, and R. Blazejewski, *River Training Techniques: Fundamentals, Design and Applications*. CRC Press, 1995.

[17] W. S. Uijttewaal, "Effects of Groyne Layout on the Flow in Groyne Fields: Laboratory Experiments," *J. Hydraul. Eng.*, vol. 131, no. 9, pp. 782–791, Sep. 2005, doi: 10.1061/(ASCE)0733-9429(2005)131:9(782).

[18] J. Xu, Y. Xue, S. Huang, L. Zhang, and F. Zhang, “Effects of Groin Type and Bed Properties on Flow in Groin Fields: Comparison of Fixed- and Mobile-Bed Experiments,” *Water*, vol. 14, no. 14, p. 2265, Jan. 2022, doi: 10.3390/w14142265.
[19] M. Henning and B. Hentschel, “Sedimentation and flow patterns induced by regular and modified groynes on the River Elbe, Germany,” *Ecohydrology*, vol. 6, Aug. 2013, doi: 10.1002/eco.1398.
[20] M. Yossef and H. J. de Vriend, “Sediment Exchange between a River and Its Groyne Fields: Mobile-Bed Experiment,” *J. Hydraul. Eng. N. Y. N*, vol. 136, no. 9, pp. 610–625, 2010, doi: 10.1061/(ASCE)HY.1943-7900.0000226.
[21] J. Qin, D. Zhong, T. Wu, and L. Wu, “Sediment exchange between groin fields and main-stream,” *Adv. Water Resour.*, vol. 108, pp. 44–54, Oct. 2017, doi: 10.1016/j.advwatres.2017.07.015.
[22] M. Yossef, “The effect of groynes on rivers,” *Delft Clust. Publ. 030304*, Jan. 2002.
[23] Ł. Przyborowski, Z. Cuban, A. Łoboda, M. Robakiewicz, S. Biegowski, and T. Kolerski, “The effect of groyne field on trapping macroplastic. Preliminary results from laboratory experiments,” *Sci. Total Environ.*, vol. 921, p. 171184, Apr. 2024, doi: 10.1016/j.scitotenv.2024.171184.
[24] R. Geyer, J. R. Jambeck, and K. L. Law, “Production, use, and fate of all plastics ever made,” *Sci. Adv.*, vol. 3, no. 7, pp. e1700782–e1700782, 2017, doi: 10.1126/sciadv.1700782.
[25] H. Yang, Y. Yumeng, Y. Yu, H. Yinglin, B. Fu, and J. Wang, “Distribution, sources, migration, influence and analytical methods of microplastics in soil ecosystems,” *Ecotoxicol. Environ. Saf.*, vol. 243, p. 114009, Sep. 2022, doi: 10.1016/j.ecoenv.2022.114009.
[26] S. Yang, G. Brasseur, S. Walters, P. Lichtig, and C. W. Y. Li, “Global atmospheric distribution of microplastics with evidence of low oceanic emissions,” *Npj Clim. Atmospheric Sci.*, vol. 8, no. 1, pp. 1–10, Feb. 2025, doi: 10.1038/s41612-025-00914-3.
[27] Organisation for Economic Co-operation and Development, *Global Plastics Outlook Economic Drivers, Environmental Impacts and Policy Options*. Paris: OECD Publishing, 2022. doi: https://doi.org/10.1787/de747aef-en.
[28] A. Rossatto, M. Z. F. Arlindo, M. S. de Morais, T. D. de Souza, and C. S. Ogrodowski, “Microplastics in aquatic systems: A review of occurrence, monitoring and potential environmental risks,” *Environ. Adv.*, vol. 13, p. 100396, Oct. 2023, doi: 10.1016/j.envadv.2023.100396.
[29] H. Zhong *et al.*, “The hidden risk of microplastic-associated pathogens in aquatic environments,” *Eco-Environ. Health*, vol. 2, no. 3, pp. 142–151, Sep. 2023, doi: 10.1016/j.eehl.2023.07.004.
[30] S. Chandra and K. B. Walsh, “Microplastics in water: Occurrence, fate and removal,” *J. Contam. Hydrol.*, vol. 264, pp. 104360-, 2024, doi: 10.1016/j.jconhyd.2024.104360.
[31] A. J. Nihart *et al.*, “Bioaccumulation of microplastics in decedent human brains,” *Nat. Med.*, 2025, doi: 10.1038/s41591-024-03453-1.
[32] Y. Li, L. Chen, N. Zhou, Y. Chen, Z. Ling, and P. Xiang, “Microplastics in the human body: A comprehensive review of exposure, distribution, migration mechanisms, and toxicity,” *Sci. Total Environ.*, vol. 946, p. 174215, Oct. 2024, doi: 10.1016/j.scitotenv.2024.174215.
[33] M. Bergmann, L. Gutow, and M. Klages, *Marine Anthropogenic Litter*. 2015. doi: 10.1007/978-3-319-16510-3.
[34] C. Chen *et al.*, “Significant regional disparities in riverine microplastics,” *J. Hazard. Mater.*, vol. 472, p. 134571, Jul. 2024, doi: 10.1016/j.jhazmat.2024.134571.
[35] L. J. J. Meijer, T. van Emmerik, R. van der Ent, C. Schmidt, and L. Lebreton, “More than 1000 rivers account for 80% of global riverine plastic emissions into the ocean,” *Sci. Adv.*, vol. 7, no. 18, p. eaaz5803, Apr. 2021, doi: 10.1126/sciadv.aaz5803.
[36] T. van Emmerik, Y. Mellink, R. Hauk, K. Waldschläger, and L. Schreyers, “Rivers as Plastic Reservoirs,” *Front. Water*, vol. 3, Jan. 2022, doi: 10.3389/frwa.2021.786936.
[37] R. Kumar *et al.*, “Effect of Physical Characteristics and Hydrodynamic Conditions on Transport and Deposition of Microplastics in Riverine Ecosystem,” *Water*, vol. 13, p. 2710, Sep. 2021, doi: 10.3390/w13192710.

[38] H. Liu and Y. Wen, “Evaluation of the migration behaviour of microplastics as emerging pollutants in freshwater environments,” *Environ. Sci. Pollut. Res.*, vol. 31, pp. 58294–58309, Sep. 2024, doi: 10.1007/s11356-024-34994-0.
[39] J. Hu, F. Y. Lim, and J. Hu, “Characteristics and behaviors of microplastics undergoing photoaging and Advanced Oxidation Processes (AOPs) initiated aging,” *Water Res.*, vol. 232, p. 119628, Apr. 2023, doi: 10.1016/j.watres.2023.119628.
[40] G. Binda *et al.*, “Microplastic aging processes: Environmental relevance and analytical implications,” *TrAC Trends Anal. Chem.*, vol. 172, p. 117566, Mar. 2024, doi: 10.1016/j.trac.2024.117566.
[41] J. Brooks and J. Hopkins, “Factors influencing the vertical distribution and transport of plastics in riverine environments: Theoretical background and implications for improved field study design,” *Environ. Pollut.*, vol. 373, p. 126151, May 2025, doi: 10.1016/j.envpol.2025.126151.
[42] M. Guo, R. Noori, and S. Abolfathi, “Microplastics in freshwater systems: Dynamic behaviour and transport processes,” *Resour. Conserv. Recycl.*, vol. 205, p. 107578, Jun. 2024, doi: 10.1016/j.resconrec.2024.107578.
[43] Z. Wang, M. Dou, P. Ren, B. Sun, R. Jia, and Y. Zhou, “Settling velocity of irregularly shaped microplastics under steady and dynamic flow conditions,” *Environ. Sci. Pollut. Res. Int.*, vol. 28, no. 44, pp. 62116–62132, 2021, doi: 10.1007/s11356-021-14654-3.
[44] Z. Yu, M. Loewen, S. Guo, Z. Guo, and W. Zhang, “Investigation of the Sheltering Effects on the Mobilization of Microplastics in Open-Channel Flow,” *Environ. Sci. Technol.*, vol. 57, no. 30, pp. 11259–11266, 2023, doi: 10.1021/acs.est.3c02500.
[45] K. D. Goral *et al.*, “Shields Diagram and the Incipient Motion of Microplastic Particles,” *Environ. Sci. Technol.*, vol. 57, no. 25, pp. 9362–9375, 2023, doi: 10.1021/acs.est.3c02027.
[46] B. Stride, S. Abolfathi, G. D. Bending, and J. Pearson, “Quantifying microplastic dispersion due to density effects,” *J. Hazard. Mater.*, vol. 466, pp. 133440–133440, 2024, doi: 10.1016/j.jhazmat.2024.133440.
[47] J. Lofty, D. Valero, C. Wilson, M. J. Franca, and P. Ouro, “Microplastic and natural sediment in bed load saltation: Material does not dictate the fate,” *Water Res. Oxf.*, vol. 243, pp. 120329-, 2023, doi: 10.1016/j.watres.2023.120329.
[48] L. Khatmullina and I. Isachenko, “Settling velocity of microplastic particles of regular shapes,” *Mar. Pollut. Bull.*, vol. 114, no. 2, pp. 871–880, 2017, doi: 10.1016/j.marpolbul.2016.11.024.
[49] P. L. Forsberg, D. Sous, A. Stocchino, and R. Chemin, “Behaviour of plastic litter in nearshore waters: First insights from wind and wave laboratory experiments,” *Mar. Pollut. Bull.*, vol. 153, p. 111023, Apr. 2020, doi: 10.1016/j.marpolbul.2020.111023.
[50] T. J. Hoellein, A. J. Shogren, J. L. Tank, P. Risteca, and J. J. Kelly, “Microplastic deposition velocity in streams follows patterns for naturally occurring allochthonous particles,” *Sci. Rep.*, vol. 9, no. 1, pp. 3740–3740, 2019, doi: 10.1038/s41598-019-40126-3.
[51] T. H. Nguyen, T.-C. Kieu-Le, F. H. M. Tang, and F. Maggi, “Controlling factors of microplastic fibre settling through a water column,” *Sci. Total Environ.*, vol. 838, p. 156011, Sep. 2022, doi: 10.1016/j.scitotenv.2022.156011.
[52] J. Zhang and C. E. Choi, “Improved Settling Velocity for Microplastic Fibers: A New Shape-Dependent Drag Model,” *Environ. Sci. Technol.*, vol. 56, no. 2, pp. 962–973, Jan. 2022, doi: 10.1021/acs.est.1c06188.
[53] K. Waldschläger and H. Schüttrumpf, “Effects of Particle Properties on the Settling and Rise Velocities of Microplastics in Freshwater under Laboratory Conditions,” *Environ. Sci. Technol.*, vol. 53, no. 4, pp. 1958–1966, 2019, doi: 10.1021/acs.est.8b06794.
[54] C. Li, X. Bai, S. Krause, and D. Luo, “Prediction of vertical transport of microplastics: Shape- and aging-dependent drag models,” *J. Hazard. Mater.*, vol. 480, p. 136412, Dec. 2024, doi: 10.1016/j.jhazmat.2024.136412.

[55] O. S. Alimi *et al.*, "Effects of weathering on the properties and fate of secondary microplastics from a polystyrene single-use cup," *J. Hazard. Mater.*, vol. 459, p. 131855, Oct. 2023, doi: 10.1016/j.jhazmat.2023.131855.
[56] L. Miao *et al.*, "Effects of biofilm colonization on the sinking of microplastics in three freshwater environments," *J. Hazard. Mater.*, vol. 413, p. 125370, Jul. 2021, doi: 10.1016/j.jhazmat.2021.125370.
[57] P. Núñez, A. Romano, J. García-Alba, G. Besio, and R. Medina, "Wave-induced cross-shore distribution of different densities, shapes, and sizes of plastic debris in coastal environments: A laboratory experiment," *Mar. Pollut. Bull.*, vol. 187, p. 114561, Feb. 2023, doi: 10.1016/j.marpolbul.2022.114561.
[58] U. Rozman, S. Filker, and G. Kalčíková, "Monitoring of biofilm development and physico-chemical changes of floating microplastics at the air-water interface," *Environ. Pollut.*, vol. 322, p. 121157, Apr. 2023, doi: 10.1016/j.envpol.2023.121157.
[59] P. O. Semcesen and M. G. Wells, "Biofilm growth on buoyant microplastics leads to changes in settling rates: Implications for microplastic retention in the Great Lakes," *Mar. Pollut. Bull.*, vol. 170, p. 112573, Sep. 2021, doi: 10.1016/j.marpolbul.2021.112573.
[60] S. Dittmar, A. S. Ruhl, K. Altmann, and M. Jekel, "Settling Velocities of Small Microplastic Fragments and Fibers," *Environ. Sci. Technol.*, vol. 58, no. 14, pp. 6359–6369, Apr. 2024, doi: 10.1021/acs.est.3c09602.
[61] M. Van Melkebeke, C. Janssen, and S. De Meester, "Characteristics and Sinking Behavior of Typical Microplastics Including the Potential Effect of Biofouling: Implications for Remediation," *Environ. Sci. Technol.*, vol. 54, no. 14, pp. 8668–8680, Jul. 2020, doi: 10.1021/acs.est.9b07378.
[62] M. H. DiBenedetto, J. Donohue, K. Tremblay, E. Edson, and K. Lavender Law, "Microplastics segregation by rise velocity at the ocean surface," *Environ. Res. Lett.*, vol. 18, no. 2, p. 024036, Feb. 2023, doi: 10.1088/1748-9326/acb505.
[63] F. Xia, Q. Yao, J. Zhang, and D. Wang, "Effects of seasonal variation and resuspension on microplastics in river sediments," *Environ. Pollut.*, vol. 286, p. 117403, Oct. 2021, doi: 10.1016/j.envpol.2021.117403.
[64] M. P. Born, C. Brüll, D. Schaefer, G. Hillebrand, and H. Schüttrumpf, "Determination of Microplastics' Vertical Concentration Transport (Rouse) Profiles in Flumes," *Environ. Sci. Technol.*, vol. 57, no. 14, pp. 5569–5579, 2023, doi: 10.1021/acs.est.2c06885.
[65] S. Francalanci, E. Paris, and L. Solari, "On the prediction of settling velocity for plastic particles of different shapes," *Environ. Pollut. 1987*, vol. 290, pp. 118068–118068, 2021, doi: 10.1016/j.envpol.2021.118068.
[66] H. Al-Zawaidah, M. Kooi, T. Hoitink, B. Vermeulen, and K. Waldschläger, "Mapping Microplastic Movement: A Phase Diagram to Predict Nonbuoyant Microplastic Modes of Transport at the Particle Scale," *Environ. Sci. Technol.*, vol. 58, no. 40, pp. 17979–17989, 2024, doi: 10.1021/acs.est.4c08128.
[67] I. Semmouri, M. Vercauteren, E. Van Acker, E. Pequeur, J. Asselman, and C. Janssen, "Distribution of microplastics in freshwater systems in an urbanized region: A case study in Flanders (Belgium)," *Sci. Total Environ.*, vol. 872, p. 162192, May 2023, doi: 10.1016/j.scitotenv.2023.162192.
[68] S. Kotar *et al.*, "Quantitative assessment of visual microscopy as a tool for microplastic research: Recommendations for improving methods and reporting," *Chemosphere*, vol. 308, no. Pt 3, p. 136449, Dec. 2022, doi: 10.1016/j.chemosphere.2022.136449.
[69] C. E. Choi, J. Zhang, and Z. Liang, "Towards realistic predictions of microplastic fiber transport in aquatic environments: Secondary motions," *Water Res.*, vol. 218, p. 118476, Jun. 2022, doi: 10.1016/j.watres.2022.118476.
[70] F. Stock *et al.*, "Pitfalls and Limitations in Microplastic Analyses," 2020. doi: 10.1007/698_2020_654.

[71] R. Mossotti, G. Dalla Fontana, A. Anceschi, E. Gasparin, and T. Battistini, “Preparation and analysis of standards containing microfilaments/microplastic with fibre shape,” *Chemosphere*, vol. 270, p. 129410, May 2021, doi: 10.1016/j.chemosphere.2020.129410.
[72] N. Kowalski, A. M. Reichardt, and J. J. Waniek, “Sinking rates of microplastics and potential implications of their alteration by physical, biological, and chemical factors,” *Mar. Pollut. Bull.*, vol. 109, no. 1, pp. 310–319, 2016, doi: 10.1016/j.marpolbul.2016.05.064.
[73] M. Mancini, T. Serra, J. Colomer, and L. Solari, “Suspended sediments mediate microplastic sedimentation in unidirectional flows,” *Sci. Total Environ.*, vol. 890, pp. 164363–164363, 2023, doi: 10.1016/j.scitotenv.2023.164363.
[74] F. Parrella, S. Brizzolara, M. Holzner, and D. M. Mitrano, “Microplastics Settling in Turbid Water: Impacts of Sediments-Induced Flow Patterns on Particle Deposition Rates,” *Environ. Sci. Technol.*, vol. 59, no. 4, pp. 2257–2265, Feb. 2025, doi: 10.1021/acs.est.4c10551.
[75] U. Ijaz, A. B. M. Baki, W. Wu, and W. Zhang, “Settling velocity of microplastics in turbulent open-channel flow,” *Sci. Total Environ.*, vol. 946, p. 174179, Oct. 2024, doi: 10.1016/j.scitotenv.2024.174179.
[76] C. Ji, J. Zhang, G. Liu, Q. Zhang, and E. Xing, “Towards better predicting the settling velocity of film-shaped microplastics based on experiment and simulation data,” *Mar. Pollut. Bull.*, vol. 203, p. 116493, Jun. 2024, doi: 10.1016/j.marpolbul.2024.116493.
[77] G. Yang *et al.*, “Settling behaviors of microplastic disks in water,” *Mar. Pollut. Bull.*, vol. 188, p. 114657, Mar. 2023, doi: 10.1016/j.marpolbul.2023.114657.
[78] K. D. Goral *et al.*, “Settling velocity of microplastic particles having regular and irregular shapes,” *Environ. Res.*, vol. 228, p. 115783, Jul. 2023, doi: 10.1016/j.envres.2023.115783.
[79] Z. Yu, M. Loewen, Y. Zhou, Z. Guo, A. B. Baki, and W. Zhang, “Continuous Near-Bed Movements of Microplastics in Open Channel Flows: Statistical Analysis,” *Environ. Sci. Technol.*, vol. 59, no. 3, pp. 1835–1843, 2025, doi: 10.1021/acs.est.4c13351.
[80] H. Chanson, *The hydraulics of open channel flow: an introduction : basic principles, sediment motion, hydraulic modelling, design of hydraulic structures*. London: Arnold, 1999.
[81] X. Yang *et al.*, “Spotlight on the vertical migration of aged microplastics in coastal waters,” *J. Hazard. Mater.*, vol. 469, p. 134040, May 2024, doi: 10.1016/j.jhazmat.2024.134040.
[82] Z. Alhusban, “Microplastic infiltration into mobile sediments,” *Sci. Total Environ.*, vol. 919, p. 170847, Apr. 2024, doi: 10.1016/j.scitotenv.2024.170847.
[83] J.-P. Boos, F. Dichgans, J. H. Fleckenstein, B. S. Gilfedder, and S. Frei, “Assessing the Behavior of Microplastics in Fluvial Systems: Infiltration and Retention Dynamics in Streambed Sediments,” *Water Resour. Res.*, vol. 60, no. 2, p. e2023WR035532, 2024, doi: 10.1029/2023WR035532.
[84] C. Ji, J. Zhang, G. Liu, Q. Zhang, and X. Shen, “A settling velocity formula for irregular shaped microplastic fragments based on new shape factor: Influence of secondary motions,” *Sci. Total Environ.*, vol. 955, p. 176857, Dec. 2024, doi: 10.1016/j.scitotenv.2024.176857.
[85] D. Kaiser, A. Estelmann, N. Kowalski, M. Glockzin, and J. J. Waniek, “Sinking velocity of sub-millimeter microplastic,” *Mar. Pollut. Bull.*, vol. 139, pp. 214–220, Feb. 2019, doi: 10.1016/j.marpolbul.2018.12.035.
[86] I. Jalón-Rojas *et al.*, “Effects of Biofilms and Particle Physical Properties on the Rising and Settling Velocities of Microplastic Fibers and Sheets,” *Environ. Sci. Technol.*, vol. 56, no. 12, pp. 8114–8123, Jun. 2022, doi: 10.1021/acs.est.2c01302.
[87] M. Mancini, S. Francalanci, T. Serra, J. Colomer, and L. Solari, “Settling velocities of microplastics with different shapes in sediment-water mixtures,” *Environ. Pollut.*, vol. 372, p. 126071, May 2025, doi: 10.1016/j.envpol.2025.126071.
[88] H. Beaumont, A. Ockelford, and P. Morris-Simpson, “Sand bed river dynamics controlling microplastic flux,” *Sci. Rep.*, vol. 14, no. 1, p. 29420, Nov. 2024, doi: 10.1038/s41598-024-80892-3.
[89] Z. Yu, G. Yang, and W. Zhang, “A new model for the terminal settling velocity of microplastics,” *Mar. Pollut. Bull.*, vol. 176, p. 113449, Mar. 2022, doi: 10.1016/j.marpolbul.2022.113449.

[90] American Society of Civil Engineers Task Committee for the Preparation of the Manual on Sedimentation, *Sedimentation engineering*. in ASCE manuals and reports on engineering practice ; no. 54. New York: The Society, 1977.
[91] F. Mendrik, R. Fernández, C. R. Hackney, C. Waller, and D. R. Parsons, "Non-buoyant microplastic settling velocity varies with biofilm growth and ambient water salinity," *Commun. Earth Environ.*, vol. 4, no. 1, p. 30, Feb. 2023, doi: 10.1038/s43247-023-00690-z.
[92] K. Karkanorachaki, E. Syranidou, and N. Kalogerakis, "Sinking characteristics of microplastics in the marine environment," *Sci. Total Environ.*, vol. 793, p. 148526, Nov. 2021, doi: 10.1016/j.scitotenv.2021.148526.
[93] M. Vercauteren, S. Lambert, E. Hoogerwerf, C. R. Janssen, and J. Asselman, "Microplastic-specific biofilm growth determines the vertical transport of plastics in freshwater," *Sci. Total Environ.*, vol. 910, p. 168399, Feb. 2024, doi: 10.1016/j.scitotenv.2023.168399.
[94] L. A. Amaral-Zettler, E. R. Zettler, T. J. Mincer, M. A. Klaassen, and S. M. Gallager, "Biofouling impacts on polyethylene density and sinking in coastal waters: A macro/micro tipping point?," *Water Res.*, vol. 201, p. 117289, Aug. 2021, doi: 10.1016/j.watres.2021.117289.
[95] S.-Y. Lee, J. An, J. Kim, and J.-H. Kwon, "Enhanced settling of microplastics after biofilm development: A laboratory column study mimicking wastewater clarifiers," *Environ. Pollut.*, vol. 311, p. 119909, Oct. 2022, doi: 10.1016/j.envpol.2022.119909.
[96] S. Dittmar, A. S. Ruhl, and M. Jekel, "Optimized and Validated Settling Velocity Measurement for Small Microplastic Particles (10–400 μm)," *ACS EST Water*, vol. 3, no. 12, pp. 4056–4065, Dec. 2023, doi: 10.1021/acsestwater.3c00457.
[97] W. Li, B. Zu, L. Hu, L. Lan, Y. Zhang, and J. Li, "Migration behaviors of microplastics in sediment-bearing turbulence: Aggregation, settlement, and resuspension," *Mar. Pollut. Bull.*, vol. 180, p. 113775, Jul. 2022, doi: 10.1016/j.marpolbul.2022.113775.
[98] M. Munz, C. Loui, D. Postler, M. Pittroff, and S. E. Oswald, "Transport and retention of micro-polystyrene in coarse riverbed sediments: effects of flow velocity, particle and sediment sizes," *Microplastics Nanoplastics*, vol. 4, no. 1, p. 2, Jan. 2024, doi: 10.1186/s43591-023-00077-z.
[99] M. Constant, C. Alary, L. Weiss, A. Constant, and G. Billon, "Trapped microplastics within vertical redeposited sediment: Experimental study simulating lake and channeled river systems during resuspension events," *Environ. Pollut.*, vol. 322, p. 121212, Apr. 2023, doi: 10.1016/j.envpol.2023.121212.
[100] M. Molazadeh *et al.*, "The role of turbulence in the deposition of intrinsically buoyant MPs," *Sci. Total Environ.*, vol. 911, p. 168540, Feb. 2024, doi: 10.1016/j.scitotenv.2023.168540.
[101] M. Mancini, S. Francalanci, L. Innocenti, and L. Solari, "Investigations on microplastic infiltration within natural riverbed sediments," *Sci. Total Environ.*, vol. 904, p. 167256, Dec. 2023, doi: 10.1016/j.scitotenv.2023.167256.
[102] K. Waldschläger and H. Schüttrumpf, "Erosion Behavior of Different Microplastic Particles in Comparison to Natural Sediments," *Environ. Sci. Technol.*, vol. 53, no. 22, pp. 13219–13227, Nov. 2019, doi: 10.1021/acs.est.9b05394.
[103] T. H. Nguyen, "Settling behaviour of irregular-shaped polystyrene microplastics," *Sci. Technol. Dev. J. - Eng. Technol.*, vol. 4, pp. 1219–1228, Dec. 2021, doi: 10.32508/stdjet.v4i4.905.
[104] C. Dai *et al.*, "Settling velocity of submillimeter microplastic fibers in still water," *Sci. Total Environ.*, vol. 907, p. 168054, Jan. 2024, doi: 10.1016/j.scitotenv.2023.168054.
[105] I. Isachenko and I. Chubarenko, "Transport and accumulation of plastic particles on the varying sediment bed cover: Open-channel flow experiment," *Mar. Pollut. Bull.*, vol. 183, p. 114079, Oct. 2022, doi: 10.1016/j.marpolbul.2022.114079.
[106] S. Cook, H.-L. Chan, S. Abolfathi, G. D. Bending, H. Schäfer, and J. M. Pearson, "Longitudinal dispersion of microplastics in aquatic flows using fluorometric techniques," *Water Res.*, vol. 170, p. 115337, Mar. 2020, doi: 10.1016/j.watres.2019.115337.

[107] M. Guo, S. A. F. Bon, and S. Abolfathi, “Transport dynamics of microplastics within aquatic vegetation featuring realistic plant morphology,” *Water Res.*, vol. 282, p. 123534, Aug. 2025, doi: 10.1016/j.watres.2025.123534.
[108] L. Nizzetto, G. Bussi, M. N. Futter, D. Butterfield, and P. G. Whitehead, “A theoretical assessment of microplastic transport in river catchments and their retention by soils and river sediments,” *Environ. Sci. Process. Impacts*, vol. 18, no. 8, pp. 1050–1059, Aug. 2016, doi: 10.1039/C6EM00206D.
[109] C. E. Russell, R. Fernández, D. R. Parsons, and S. E. Gabbott, “Plastic pollution in riverbeds fundamentally affects natural sand transport processes,” *Commun. Earth Environ.*, vol. 4, no. 1, pp. 1–10, Jul. 2023, doi: 10.1038/s43247-023-00820-7.
[110] T. van Emmerik and A. Schwarz, “Plastic debris in rivers,” *WIREs Water*, vol. 7, no. 1, p. e1398, 2020, doi: 10.1002/wat2.1398.
[111] M. Kooi, E. H. van Nes, M. Scheffer, and A. A. Koelmans, “Ups and Downs in the Ocean: Effects of Biofouling on Vertical Transport of Microplastics,” *Environ. Sci. Technol.*, vol. 51, no. 14, pp. 7963–7971, Jul. 2017, doi: 10.1021/acs.est.6b04702.
[112] P. Dellino, D. Mele, R. Bonasia, G. Braia, L. La Volpe, and R. Sulpizio, “The analysis of the influence of pumice shape on its terminal velocity,” *Geophys. Res. Lett.*, vol. 32, no. 21, 2005, doi: 10.1029/2005GL023954.
[113] Y. Li *et al.*, “Interactions between nano/micro plastics and suspended sediment in water: Implications on aggregation and settling,” *Water Res.*, vol. 161, pp. 486–495, Sep. 2019, doi: 10.1016/j.watres.2019.06.018.
[114] S. C. Chikwendu, “Calculation of longitudinal shear dispersivity using an N-zone model as N,” *J. Fluid Mech.*, vol. 167, pp. 19–30, 1986, doi: 10.1017/S0022112086002707.
[115] J. W. Elder, “The dispersion of marked fluid in turbulent shear flow,” *J. Fluid Mech.*, vol. 5, no. 4, pp. 544–560, 1959, doi: 10.1017/S0022112059000374.
[116] R. L. Martin, D. J. Jerolmack, and R. Schumer, “The physical basis for anomalous diffusion in bed load transport,” *J. Geophys. Res. Earth Surf.*, vol. 117, no. F1, 2012, doi: 10.1029/2011JF002075.
[117] H. M. Nepf, “Drag, turbulence, and diffusion in flow through emergent vegetation,” *Water Resour. Res.*, vol. 35, no. 2, pp. 479–489, 1999, doi: 10.1029/1998WR900069.
[118] W. Cowger, A. B. Gray, J. J. Guilinger, B. Fong, and K. Waldschläger, “Concentration Depth Profiles of Microplastic Particles in River Flow and Implications for Surface Sampling,” *Environ. Sci. Technol.*, vol. 55, no. 9, pp. 6032–6041, May 2021, doi: 10.1021/acs.est.1c01768.
[119] T. Chor, D. Yang, C. Meneveau, and M. Chamecki, “A Turbulence Velocity Scale for Predicting the Fate of Buoyant Materials in the Oceanic Mixed Layer,” *Geophys. Res. Lett.*, vol. 45, no. 21, p. 11,817-11,826, 2018, doi: 10.1029/2018GL080296.
[120] X. Yang *et al.*, “Unveiling the Vertical Migration of Microplastics with Suspended Particulate Matter in the Estuarine Environment: Roles of Salinity, Particle Properties, and Hydrodynamics,” *Environ. Sci. Technol.*, vol. 58, no. 6, pp. 2944–2955, Feb. 2024, doi: 10.1021/acs.est.3c08186.
[121] S. A. Bradford, S. R. Yates, M. Bettahar, and J. Simunek, “Physical factors affecting the transport and fate of colloids in saturated porous media,” *Water Resour. Res.*, vol. 38, no. 12, pp. 63-1-63–12, 2002, doi: 10.1029/2002WR001340.
[122] M. Poulain-Zarcos, N. Pujara, G. Verhille, and M. J. Mercier, “Laboratory experiments related to marine plastic pollution: a review of past work and future directions,” *Comptes Rendus Phys.*, vol. 25, no. S3, pp. 235–266, 2024, doi: 10.5802/crphys.217.
[123] H. Park and H. Nepf, “Biological Cohesion of Sediment Bed Diminishes Net Deposition of Fine Non-Cohesive Particles Over Bare Bed and Within Model Emergent Canopies,” *Geophys. Res. Lett.*, vol. 52, no. 10, p. n/a, 2025, doi: 10.1029/2025GL115331.
[124] A. J. Nihart *et al.*, “Bioaccumulation of microplastics in decedent human brains,” *Nat. Med.*, pp. 1–6, Feb. 2025, doi: 10.1038/s41591-024-03453-1.

[125] A. Haque, T. M. Holsen, and A. B. M. Baki, “Distribution and risk assessment of microplastic pollution in a rural river system near a wastewater treatment plant, hydro-dam, and river confluence,” *Sci. Rep.*, vol. 14, no. 1, p. 6006, Mar. 2024, doi: 10.1038/s41598-024-56730-x.
[126] I. Pojar *et al.*, “Microplastic Evaluation in Water and Sediments of a Dam Reservoir–Riverine System in the Eastern Carpathians, Romania,” *Sustainability*, vol. 16, no. 11, p. 4541, Jan. 2024, doi: 10.3390/su16114541.
[127] A. Z. Fazil, D. D. S. Dhawala Wijeratna, and P. I. A. Gomes, “Predicting microplastic transport in open channels with different bed types and river regulation with machine learning techniques,” *Environ. Pollut.*, vol. 384, p. 126912, Nov. 2025, doi: 10.1016/j.envpol.2025.126912.
[128] L. Cao, X. Shen, H. Cai, W. Gao, S. Li, and D. Li, “Mechanisms of influence of confluence containing spur-dike on microplastic transport and fate,” *J. Hydrol.*, vol. 641, p. 131720, Sep. 2024, doi: 10.1016/j.jhydrol.2024.131720.
[129] E. C. for A. and the F. E. United Nations, *River training and bank protection*. in Flood control series ; no. 4. Bangkok: United Nations, 1953.
[130] M. Henning and B. Hentschel, “Sedimentation and flow patterns induced by regular and modified groynes on the River Elbe, Germany,” *Ecohydrology*, vol. 6, no. 4, pp. 598–610, 2013, doi: 10.1002/eco.1398.
[131] Public Services and Procurement Canada, “Lake Windermere: Groyne marker installation.” Accessed: Aug. 15, 2025. [Online]. Available: https://www.canada.ca/en/public-services-procurement/services/infrastructure-buildings/bridges-docks-dams/lake-windermere-groyne-marker-installation.html
[132] S. Chakravarty, H. K. Patel, B. Mohanty, and B. Kumar, “Review on different shapes of spurs and their effects on channel morphology,” *Water Pract. Technol.*, vol. 19, no. 1, pp. 241–262, Dec. 2023, doi: 10.2166/wpt.2023.221.
[133] M. Yossef, “The Effect of Groynes on Rivers,” Faculty of Civil Engineering and Geosciences, Delft University of Technology, 2002. Accessed: Aug. 16, 2025. [Online]. Available: https://www.semanticscholar.org/paper/The-Effect-of-Groynes-on-Rivers-Yossef/a721f6d5183f4ce29ca4ecc1efe9fd6a31172f8b#citing-papers
[134] V. Weitbrecht, S. A. Socolofsky, and G. H. Jirka, “Experiments on Mass Exchange between Groin Fields and Main Stream in Rivers,” *J. Hydraul. Eng.*, vol. 134, no. 2, pp. 173–183, Feb. 2008, doi: 10.1061/(ASCE)0733-9429(2008)134:2(173).
[135] A. Kadota, K. Suzuki, and E. Kojima, “Flow Visualization of Mean and Coherent Flow Structures around T-type and L-type Groynes,” presented at the River Flow 2010, 2010, pp. 203–210.
[136] G. Bagheri and C. Bonadonna, “On the drag of freely falling non-spherical particles,” *Powder Technol.*, vol. 301, pp. 526–544, Nov. 2016, doi: 10.1016/j.powtec.2016.06.015.
[137] J. Nikuradse, *Strömungsgesetze in rauhen Rohren [Flow Laws in Rough Pipes]*. Germany: VDI-Verlag, 1933.
[138] P. Wardhana, “Turbulence Characteristic of Flow Near Laboratory Experiment Groin Fields,” *MEDIA Komun. Tek. SIPIL*, vol. 24, p. 167, Feb. 2019, doi: 10.14710/mkts.v24i2.20729.
[139] D. B. Allan, T. Caswell, N. C. Keim, C. M. van der Wel, and R. W. Verweij, *soft-matter/trackpy: v0.7*. (Jul. 18, 2025). Zenodo. doi: 10.5281/zenodo.16089574.
[140] T. Wu and J. Qin, “Influence of Flow and Sediment Transport Processes on Sedimentation in Groyne Fields,” *J. Coast. Res.*, vol. 95, p. 304, May 2020, doi: 10.2112/SI95-059.1.
[141] H. Zhang and H. Nakagawa, “Scour around Spur Dyke: Recent Advances and Future Researches,” *Ann Disaster Prev. Res Inst Kyoto Univ*, vol. 51, Jan. 2008.
[142] D. Liu, S. Lv, and C. Li, “Impact of Spur Dike Placement on Flow Dynamics in Curved River Channels: A CFD Study on Pick Angle and River-Width-Narrowing Rate,” *Water*, vol. 16, no. 16, p. 2236, Jan. 2024, doi: 10.3390/w16162236.

[143] H. kumar Patel and B. Kumar, “Experimental study on the optimal spur dike shape under downward seepage,” *Water Sci.*, vol. 38, no. 1, pp. 172–191, Dec. 2024, doi: 10.1080/23570008.2024.2321423.
[144] A. Sukhodolov, W. S. J. Uijttewaal, and C. Engelhardt, “On the correspondence between morphological and hydrodynamical patterns of groyne fields,” *Earth Surf. Process. Landf.*, vol. 27, no. 3, pp. 289–305, 2002, doi: 10.1002/esp.319.
[145] K. G. Gebrelibanos, K. Vereide, S. A. Weldemariam, A. Bor, A. H. Tesfay, and L. Lia, “Hydraulic Scale Modeling of Pressurized Sediment Laden Flow,” *Water*, vol. 17, no. 13, p. 1970, Jan. 2025, doi: 10.3390/w17131970.
[146] A. L. Prasuhn, *Fundamentals of hydraulic engineering*. New York: Oxford University Press, 1992.
[147] S. A. Hughes, *Physical models and laboratory techniques in coastal engineering*. in Advanced series on ocean engineering ; v. 007. Singapore ; World Scientific, 1993.
[148] M. R. Leeder and P. H. Bridges, “Flow separation in meander bends,” *Nature*, vol. 253, no. 5490, pp. 338–339, Jan. 1975, doi: 10.1038/253338a0.
[149] M. Shinbein, “Physical Modeling of Rivers in the Hydraulics Laboratory.” U. S. Department of the Interior, 2021. Accessed: Aug. 22, 2025. [Online]. Available: https://usbr.gov/research/projects/detail.cfm?id=21200
[150] M. Alauddin and T. Tsujimoto, “Optimum configuration of groynes for stabilization of alluvial rivers with fine sediments,” *Int. J. Sediment Res.*, vol. 27, no. 2, pp. 158–167, Jun. 2012, doi: 10.1016/S1001-6279(12)60024-9.

Appendix A: Adopted Drag Model

The semi-empirical drag model proposed by Bagheri and Bonadonna (2016) [136] was constructed on shape-dependent correction factors for both viscous (k_S) and inertial flow (k_N). The two factors were adapted from existing models by substituting alternative shape descriptors:

$$k_S = \frac{1}{2}\left(F_S^{\frac{1}{3}} + F_S^{-\frac{1}{3}}\right) \tag{1}$$

$$k_N = 10^{\alpha(-\log(F_N))^{\beta}} \tag{2}$$

in which the Stokes shape factor (F_S) and Newton shape factor (F_N) were defined as:

$$F_S = fE^{1.3}\left(\frac{d_{eq}^3}{abc}\right) = \frac{d_{eq}^3}{a^{2.3}b^{0.7}} \tag{3}$$

$$F_N = f^2E\left(\frac{d_{eq}^3}{abc}\right) = \frac{cd_{eq}^3}{a^2b^2} \tag{4}$$

where α and β were empirical parameters:

$$\alpha = 0.45 + \frac{10}{\exp\left(2.5 * \log\left(\frac{\rho_p}{\rho_f}\right) + 30\right)} \tag{5}$$

$$\beta = 1 - \frac{37}{\exp\left(3\log\left(\frac{\rho_p}{\rho_f}\right) + 100\right)} \tag{6}$$

in which *a* is the length of longest side; *b* is the length of intermediate side; *c* is the length of shortest side; *E* is the elongation factor, where $E = b/a$; and *f* is the flatness factor, where $f = c/b$. By incorporating both corrections into a single framework, the authors proposed the following general drag correlation for non-spherical particles:

$$C_D = \frac{24}{Re}k_S\left(1 + 0.125\left(Re\frac{k_N}{k_S}\right)^{\frac{2}{3}}\right) + 0.46k_N\left(1 + \frac{5330}{Re\frac{k_N}{k_S}}\right)^{-1} \tag{7}$$

Where the first term dominates in the Stokes ($Re < 0.1$) and intermediate ($0.1 \leq Re < 1000$) regimes, reflecting viscous contributions to drag. The second term represents the Newtonian regime ($1000 \leq Re < 3$

$\times 10^5$), where inertial drag becomes nearly constant but is still shape-dependent. The empirical constants were determined by calibrating against >2,000 data points (mean error = 9.8%) [136].

Appendix B: Experimental Setup

Groyne dimensions

Dimensions of all groyne shapes were shown in Table S1, which followed shapes described in literatures [16], [129]. In particular, rather than the smoothly curved hockey shape reported in some studies, the variant suggested by Alauddin & Tsujimoto [150], which showed higher sediment deposition, was adopted. For clarity, it is still referred to here as hockey-shaped. Figure S2 presents the plan views of the shapes listed in Table S1, with the spacing reduced to improve the clarity of the photograph.

Table S1 Dimensions of groynes used in the current study.

Groyne configuration	**Dimensions**
Straight (S)	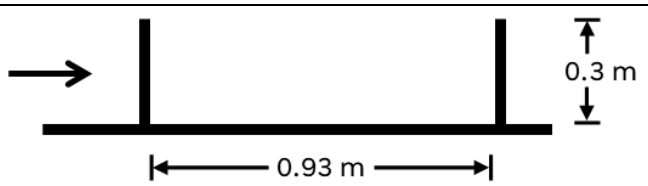
Repelling (R)	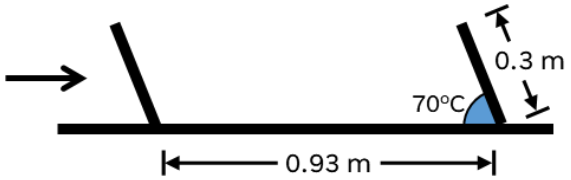
T-shaped (T)	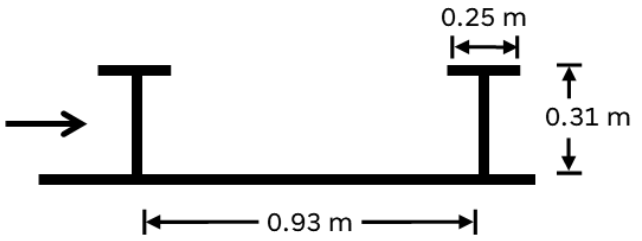
Hockey-shaped (H)	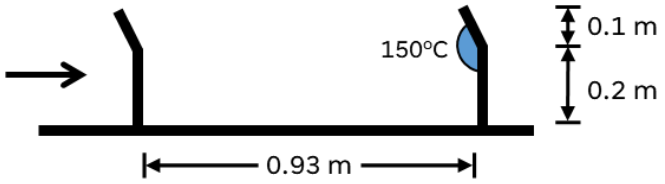

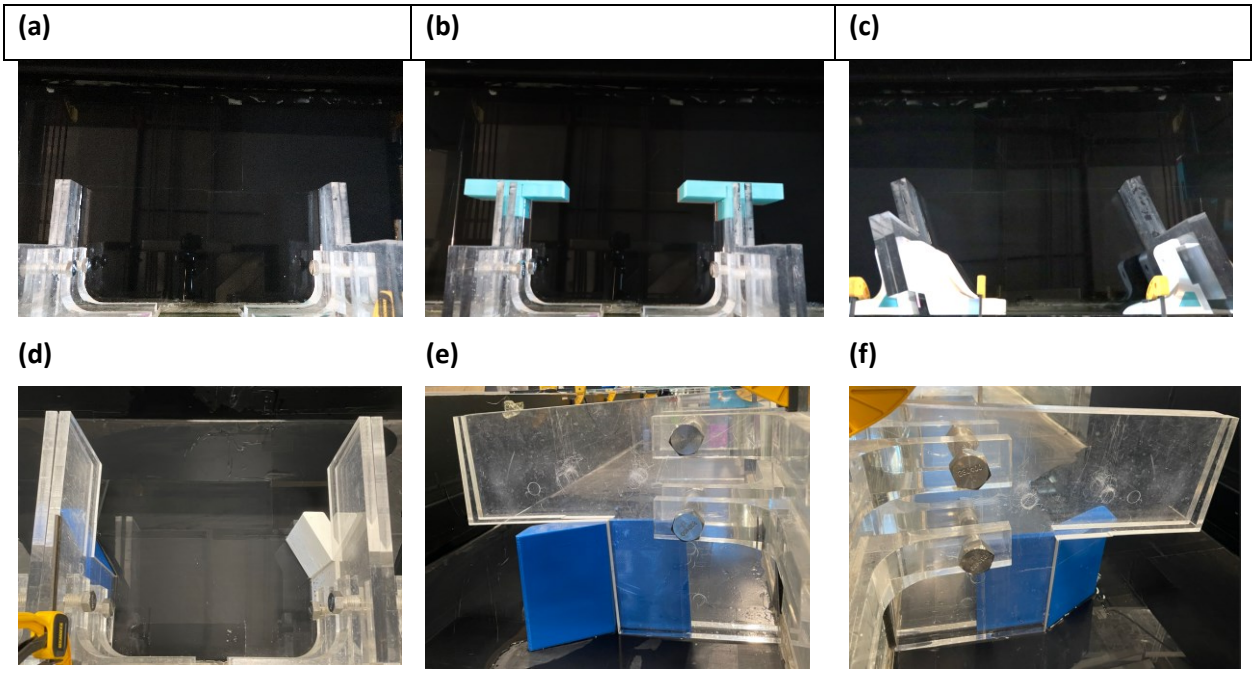

Figure S1 Plan view images of difference groyne shapes: (a) straight; (b) T-shape; (c) repelling; and (d) hockey-shape. Figures (e) and (f) show side views of the hockey-shaped groynes to aid interpretation of the plan view. Flow directed from left to right.

Table S2 Groyne configurations and corresponding IDs.

Configuration ID	Configuration
SS	
RR	
TT	
HH	
RS	
TS	
HS	
SR	

ST	
SH	

Microplastics Dimensions and Injection

The 3D image of the MPs particles was shown below. Regarding MPs injection, 1,000 MP particles were divided into 10 batches by using a measuring spoon before each injection. During injection, the automotive fluid extractor was kept perpendicular to maintain a stable flow of MPs into the outlet tube.

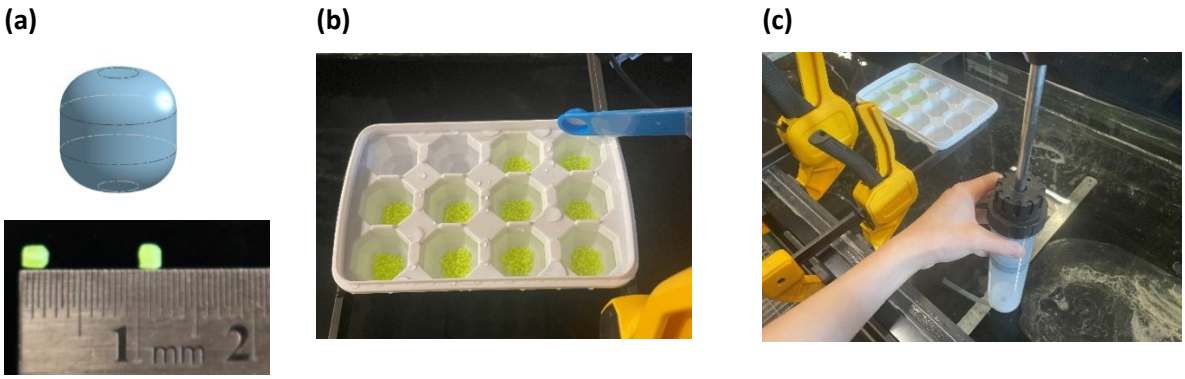

Figure S2 (a) 3D model and printed MPs particles (b) Particles were divided into 10 batches before injection (c) Injection setup.

Appendix C: Particle Tracking Model (PTM)

Video Preprocessing and Particle Tracking

The PTM comprised three components: video preprocessing, particle tracking using the Python library *Trackpy*, and optimization. The flowchart for the first two components is shown below.

Video recordings of experiments conducted under identical conditions (e.g., with the same camera position) for the same scenario were stored in the same folder. When the videos were loaded, the program first checked whether it was the initial processing attempt. If not, the user was prompted to crop the region of interest (ROI) to account for any suboptimal camera positioning. The groyne field was then defined by plotting straight lines on a pop-up window, after which the ROI was further divided into three zones: inlet, outlet, and passway. This division allowed particle trajectories to be systematically categorized into groups. For example, all particles that first appeared in the inlet zone and later disappeared in the groyne field were categorized as group A, while particles which appeared in the inlet zone and disappeared in outlet zone were in group B.

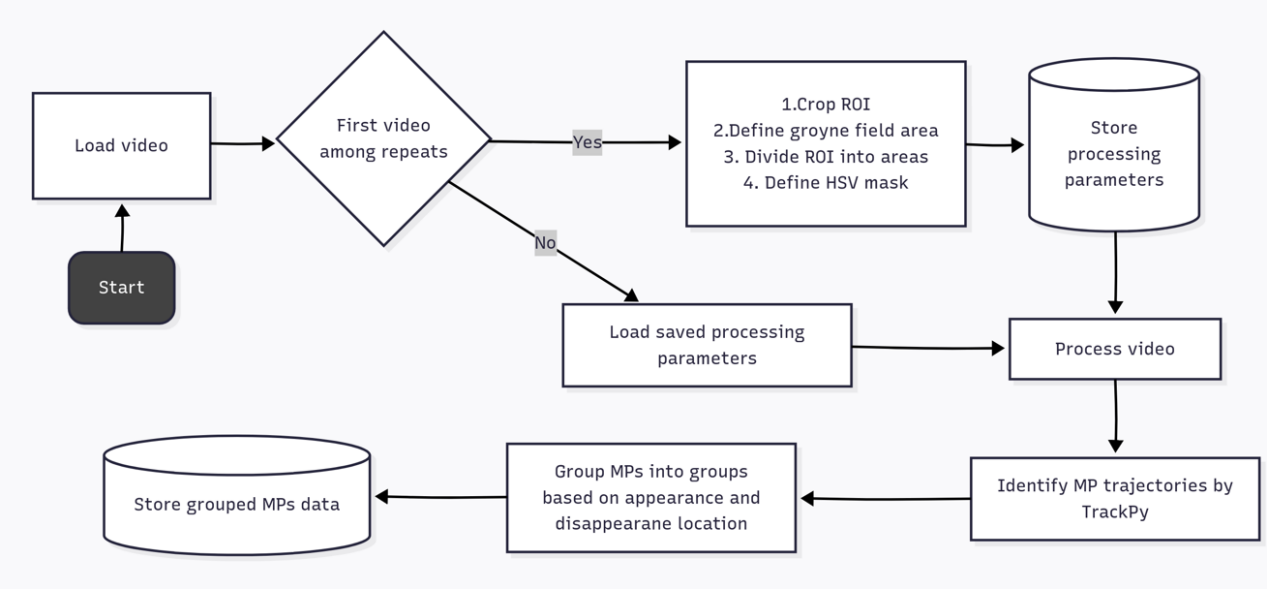

Figure S3 Flow chart of preproccesing and particle tracking.

Trajectory Optimization

The image below shows the iterative linking procedures for reconstructing particle trajectories by linking false splits by different mechanisms.

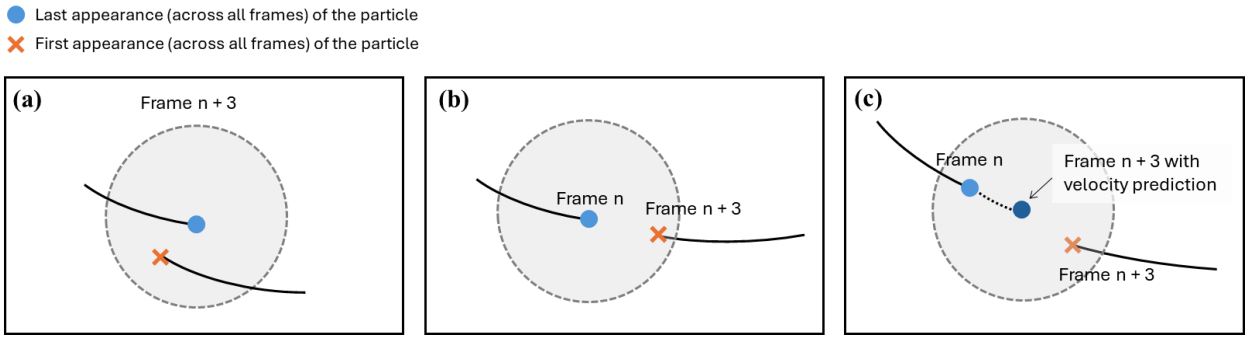

Figure S4 Illustration of the iterative linking methods. All particles which first appear or disappear within the groyne field will be eligible for this procedure. The blue dot and orange cross indicate respectively the last and first spot which the particle was spotted. The grey circle in dotted line was the distance-based search range with radius defined by variable "dist" (Fig. 3). Each image refers to a different mechanism: (a) All trajectories in the same range of frames were plotted, the nearest start and end points within the search radius will be considered the same particle; (b) Linking by looking into future frames after particle disappearance (search window set as 3 in this example); (c) Similarly, also looking into future frames after particle disappearance with search radius shifted based on velocity prediction (search window set as 3 in this example).

Appendix D: Normality Check

Shapiro-Wilk Test

Table S3 Shapiro-Wilk Test Results.

Scenario	**n**	**W**	**p-value**
SS-D	20	0.9724	0.8037
SS-L	20	0.9358	0.1993
SR-D	20	0.9088	0.0606
SR-L	20	0.9217	0.1070
ST-D	**20**	**0.9022**	**0.0454**
ST-L	20	0.9411	0.2510
SH-D	20	0.9543	0.4364
SH-L	20	0.9572	0.4896
RS-D	20	0.9699	0.7527
RS-L	20	0.9515	0.3903
TS-D	20	0.9789	0.9198
TS-L	**20**	**0.8842**	**0.0211**
HS-D	20	0.9684	0.7213
HS-L	20	0.9839	0.9744
RR-D	20	0.9672	0.6947
RR-L	20	0.9930	0.9999
TT-D	19	0.9438	0.3083
TT-L	20	0.9270	0.1350
HH-D	20	0.9546	0.4427
HH-L	20	0.9743	0.8425

Q-Q Plots

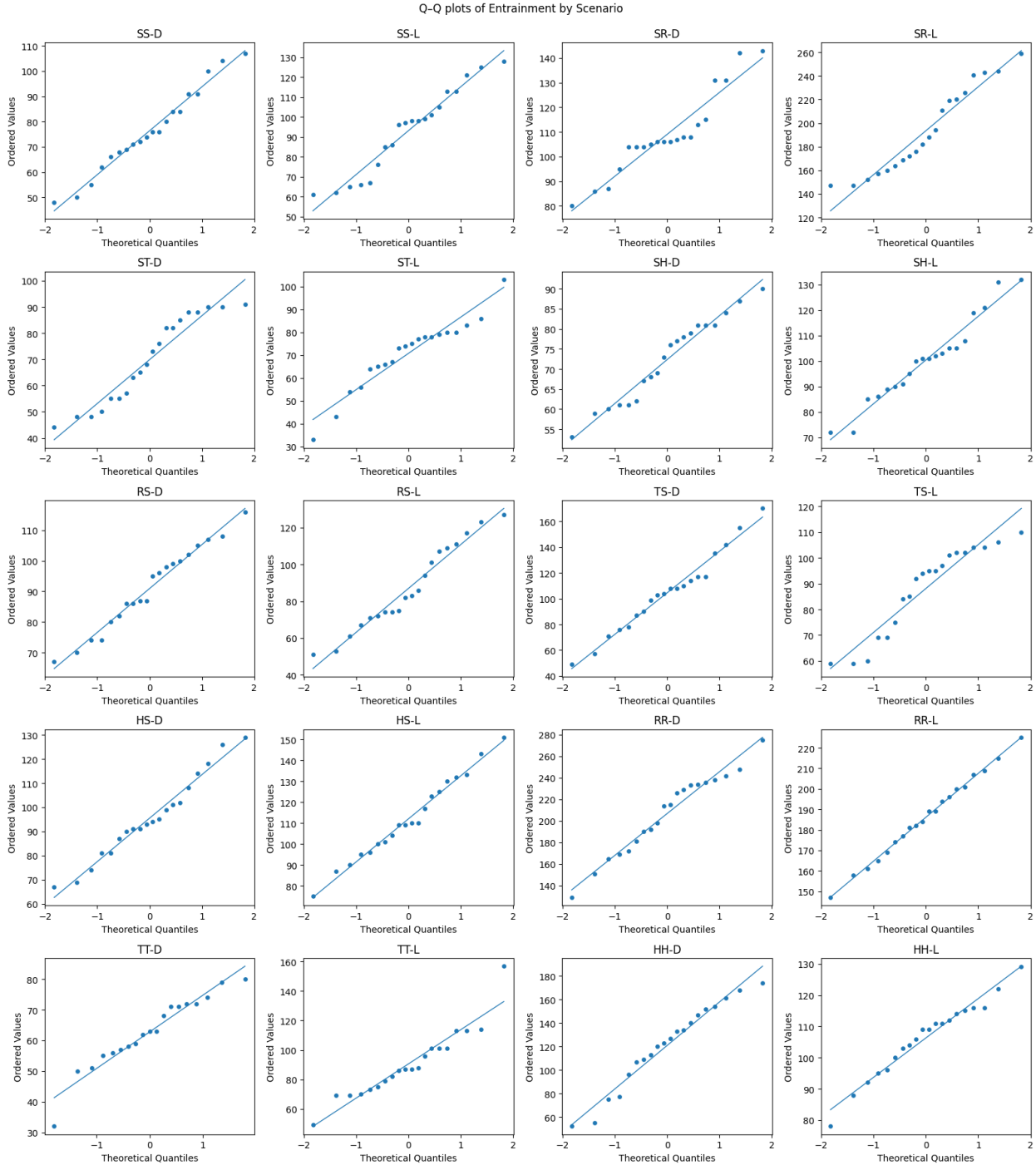

Figure S5 QQ plot of all scenarios.

Appendix E: Entrainment and Escape Rate

Descriptive statistics

The table below summarizes the mean (μ), standard deviation (σ) and coefficient of variance (CV) of entrainment and escape rates by each scenario.

Table S4 Summary table of MPs entrainment and escape rates by scenario.

Scenario	n	$\mu_{entrainment\ rate}$	$\sigma_{entrainment\ rate}$	$\%CV_{entrainment\ rate}$	$\mu_{escape\ rate}$	$\sigma_{escape\ rate}$
HH-D	20	12.10%	3.60%	29.60%	15.10%	13.50%
HH-L	20	10.60%	1.20%	11.40%	0.10%	0.40%
HS-D	20	9.60%	1.70%	18.10%	0.00%	0.20%
HS-L	20	11.20%	2.00%	17.50%	0.00%	0.20%
RR-D	20	20.70%	3.70%	18.10%	7.20%	4.50%
RR-L	20	18.60%	2.00%	10.90%	3.20%	3.40%
RS-D	20	9.10%	1.40%	15.10%	0.50%	1.50%
RS-L	20	8.70%	2.30%	26.40%	0.00%	0.00%
SH-D	20	7.20%	1.10%	14.60%	0.00%	0.00%
SH-L	20	10.00%	1.70%	16.50%	0.00%	0.00%
SR-D	20	10.90%	1.70%	15.50%	0.90%	1.60%
SR-L	20	19.40%	3.60%	18.80%	1.60%	2.00%
SS-D	20	7.60%	1.70%	21.80%	0.50%	1.00%
SS-L	20	9.30%	2.10%	23.00%	0.00%	0.00%
ST-D	20	7.00%	1.70%	23.60%	0.00%	0.00%
ST-L	20	7.10%	1.60%	22.10%	0.00%	0.00%
TS-D	20	10.40%	3.10%	29.60%	9.30%	11.50%
TS-L	20	8.80%	1.70%	19.30%	1.80%	2.90%
TT-D	19	6.30%	1.20%	18.60%	2.80%	2.90%
TT-L	20	9.00%	2.30%	25.60%	1.10%	1.50%

Dwass–Steel–Critchlow–Fligner Test

The table below showed the pairwise comparison by groyne shapes. P-value adjustment was applied in the DCSF test to control for inflated Type I error due to multiple comparisons, with Holm adjustments used in accordance with standard procedures.

Table S5 Pairwise comparison based on groyne shape, scenarios organized by straight groyne locations. Pairs with insignificant differences (p-values > 0.05) bolded.

Scenario i	Scenario j	Median i	Median j	Cliffs delta |δ|	p-value	Adjusted p-value
RR-D	TT-D	214.5	63	1.0000	5.580E-07	2.790E-06
SS-D	RR-D	75	214.5	-1.0000	3.755E-07	2.253E-06
RR-D	HH-D	214.5	125	0.9100	5.077E-06	2.031E-05
TT-D	HH-D	63	125	-0.8132	8.324E-05	2.497E-04
SS-D	HH-D	75	125	-0.7150	6.318E-04	1.264E-03
SS-D	**TT-D**	**75**	**63**	**0.4684**	**5.944E-02**	**5.944E-02**
RR-L	TT-L	186.5	87	0.9950	4.335E-07	2.250E-06
SS-L	RR-L	97.5	186.5	-1.0000	3.755E-07	2.250E-06
RR-L	HH-L	186.5	109	1.0000	3.750E-07	2.250E-06
TT-L	**HH-L**	**87**	**109**	**-0.5425**	**1.747E-02**	**5.240E-02**
SS-L	**HH-L**	**97.5**	**109**	**-0.3775**	**1.723E-01**	**3.447E-01**
SS-L	**TT-L**	**97.5**	**87**	**0.0675**	**9.833E-01**	**9.833E-01**
SS-D	TS-D	75	106	-0.5900	7.677E-03	4.606E-02
SS-D	**HS-D**	**75**	**93.5**	**-0.5650**	**1.192E-02**	**5.960E-02**
SS-D	**RS-D**	**75**	**91**	**-0.4925**	**3.845E-02**	**1.538E-01**
RS-D	**TS-D**	**91**	**106**	**-0.3475**	**2.362E-01**	**7.085E-01**
TS-D	**HS-D**	**106**	**93.5**	**0.2000**	**7.002E-01**	**1.000E+00**
RS-D	**HS-D**	**91**	**93.5**	**-0.1275**	**9.008E-01**	**1.000E+00**
RS-L	HS-L	82.5	109.5	-0.5850	8.400E-03	4.200E-02
TS-L	HS-L	94.5	109.5	-0.6250	3.982E-03	2.389E-02
SS-L	**RS-L**	**97.5**	**82.5**	**0.1500**	**8.489E-01**	**1.000E+00**
SS-L	**HS-L**	**97.5**	**109.5**	**-0.4575**	**6.371E-02**	**2.548E-01**
RS-L	**TS-L**	**82.5**	**94.5**	**-0.0375**	**9.970E-01**	**1.000E+00**
SS-L	**TS-L**	**97.5**	**94.5**	**0.1575**	**8.292E-01**	**1.000E+00**
SR-D	ST-D	106	70.5	0.9100	4.988E-06	2.494E-05
SR-D	SH-D	106	74.5	0.9525	1.500E-06	8.999E-06
SS-D	SR-D	75	106	-0.8525	2.314E-05	9.258E-05
SS-D	**ST-D**	**75**	**70.5**	**0.1950**	**7.163E-01**	**1.000E+00**
ST-D	**SH-D**	**70.5**	**74.5**	**-0.0425**	**9.957E-01**	**1.000E+00**
SS-D	**SH-D**	**75**	**74.5**	**0.1325**	**8.902E-01**	**1.000E+00**
SR-L	ST-L	185	74.5	1.0000	3.755E-07	2.250E-06
SS-L	SR-L	97.5	185	-1.0000	3.755E-07	2.250E-06

SR-L	SH-L	185	101	1.0000	3.750E-07	2.250E-06
ST-L	SH-L	74.5	101	-0.8200	5.374E-05	1.612E-04
SS-L	ST-L	97.5	74.5	0.5450	1.679E-02	3.358E-02
SS-L	**SH-L**	**97.5**	**101**	**-0.2125**	**6.582E-01**	**6.582E-01**

The following table showed the pairwise comparison by MPs densities. Similarly, the p-value was adjusted.

Table S6 Pairwise comparison based on MPs densities, ordered in descending adjusted p-value. Pairs with insignificant differences (p-values > 0.05) bolded.

Scenario i	Scenario j	Median i	Median j	Cliffs delta |δ|	p-value	Adjusted p-value
SR-D	SR-L	106	185	-1.0000	6.204E-08	6.204E-07
SH-D	SH-L	74.5	101	-0.8625	3.040E-06	2.736E-05
TT-D	TT-L	63	87	-0.7605	4.858E-05	3.886E-04
HS-D	**HS-L**	**93.5**	**109.5**	**-0.4850**	**8.669E-03**	**6.068E-02**
SS-D	**SS-L**	**75**	**97.5**	**-0.4150**	**2.469E-02**	**1.481E-01**
RR-D	**RR-L**	**214.5**	**186.5**	**0.3800**	**3.975E-02**	**1.921E-01**
HH-D	**HH-L**	**125**	**109**	**0.3675**	**4.672E-02**	**1.921E-01**
TS-D	**TS-L**	**106**	**94.5**	**0.3825**	**3.841E-02**	**1.921E-01**
RS-D	**RS-L**	**91**	**82.5**	**0.1325**	**4.731E-01**	**9.462E-01**
ST-D	**ST-L**	**70.5**	**74.5**	**0.0100**	**9.568E-01**	**9.568E-01**

Appendix F: Groyne Field Dynamics

MPs entered the groyne field from the downstream end, where they formed a clockwise gyre. The trajectories of each particle within the first 5 seconds they entered the ROI were averaged and plotted below.

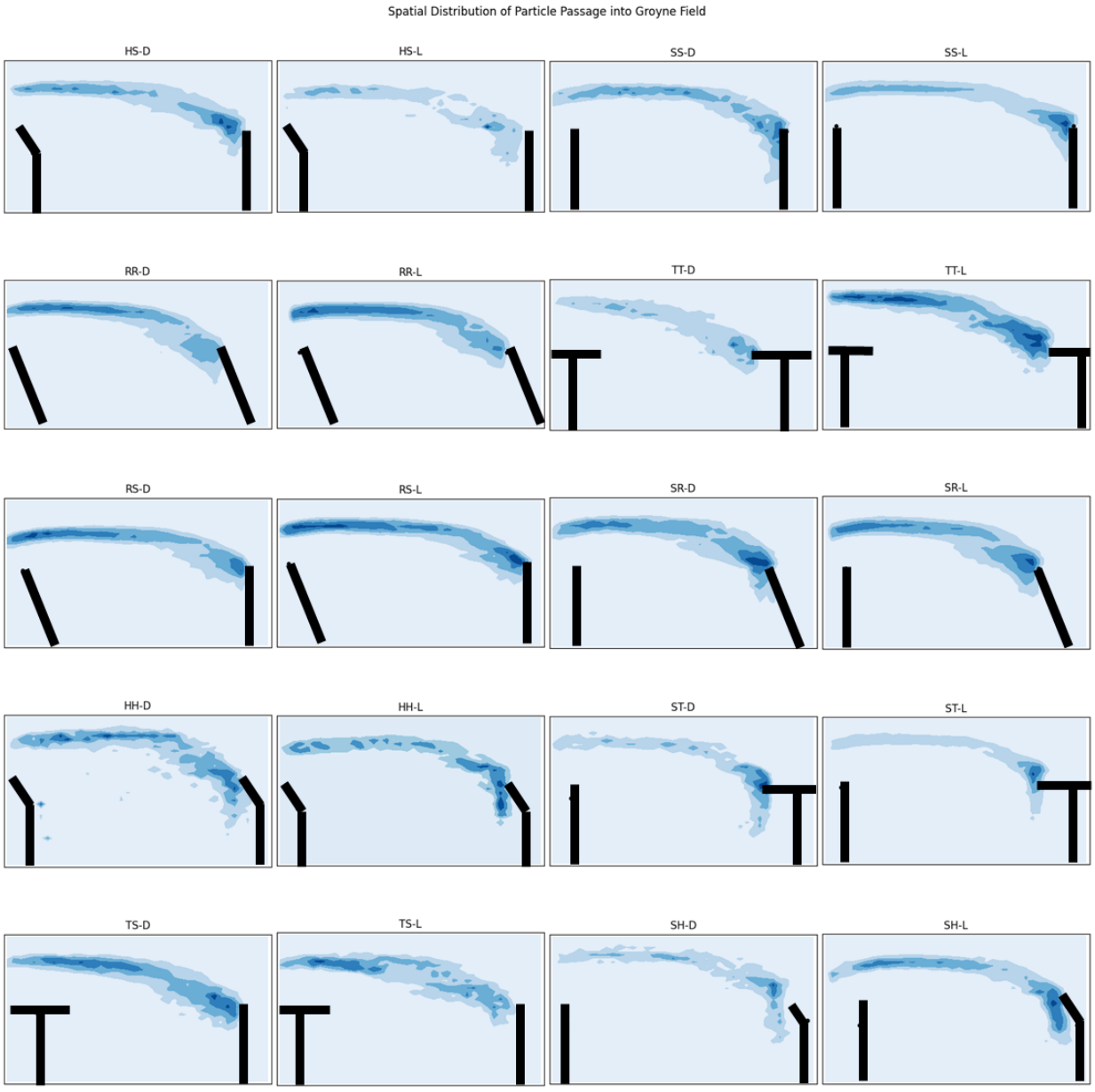

Figure S6 Distribution of particles within first 5 seconds after entering ROI. Flow directed from left to right.

Appendix G: Microplastics Retention Zones

Spatial distribution of MPs particles (ρ_s = 1.08 g/cm^3) in groyne fields during the final 150 s of the experiment was illustrated below.

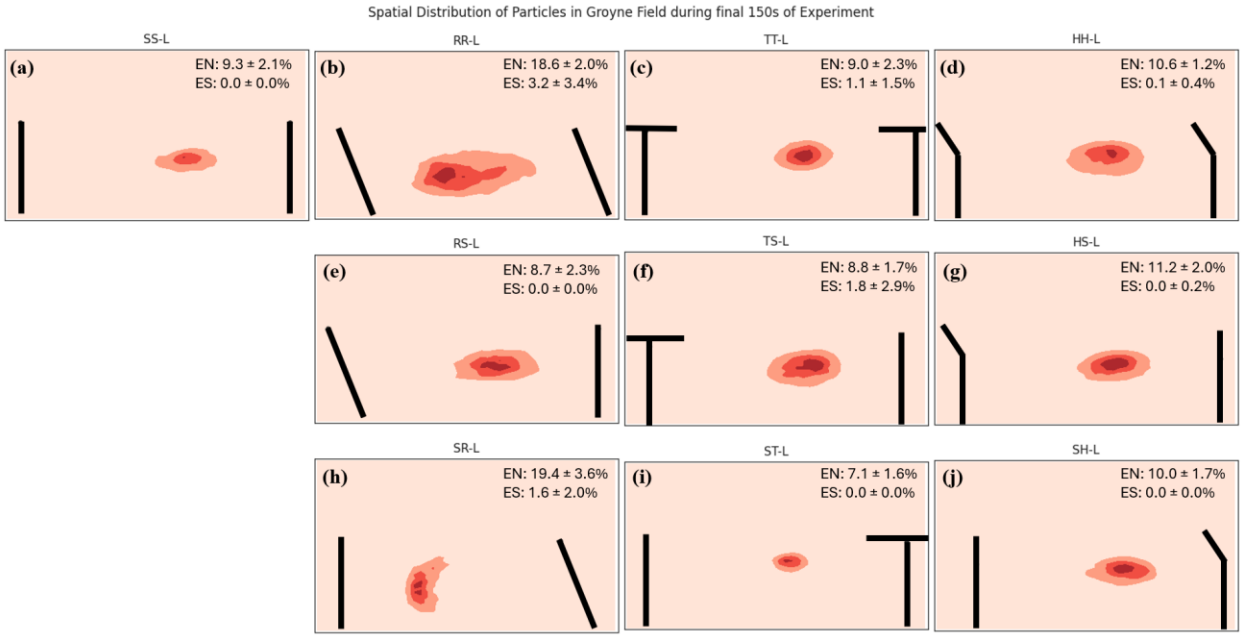

Figure S7 Spatial distribution of light MPs particles in groyne field in the final 150 s of each run. Flow directed from left to right.